The Dissertation Committee for Stephen Travis Bannerman
certifies that this is the approved version of the following dissertation:

Cooling Atomic Ensembles with Maxwell's Demon

Committee:

Mark G. Raizen, Supervisor

Herbert L. Berk

Jennifer S. Brodbelt

Todd Ditmire

Linda E. Reichl

Cooling Atomic Ensembles with Maxwell's Demon

by

Stephen Travis Bannerman, B.S.Phy.

DISSERTATION

Presented to the Faculty of the Graduate School of

The University of Texas at Austin

in Partial Fulfillment

of the Requirements

for the Degree of

DOCTOR OF PHILOSOPHY

THE UNIVERSITY OF TEXAS AT AUSTIN

August 2011

For the Fat Lady.

Acknowledgments

First and foremost, I would like to thank my advisor, Professor Mark Raizen. Mark's creativity and exuberance for physics are unrivaled, and it has been a privilege for me to work with him over the last five years. I am immensely grateful for the opportunity that he gave me to work in the group and for his continued support.

Not even a century ago, experiments on the forefront of science were often conducted solely by a professor or with a single graduate student. It is said, however, that Nature gives up her secrets reluctantly, and it would seem that she becomes more reclusive with each successive interrogation. Today, multiple graduate students and postdocs working in tandem under the direction of an advisor are often needed in order to construct experiments of great complexity. I am indebted to a great number of people, without whom the research in this dissertation would not have been possible.

For my first three years in the lab, I worked closely with Gabriel Price on the rubidium experiment. Gabe was a terrific labmate and an outstanding friend. His jovial personality and quick wit made it a pleasure to work in the lab late into the night and on weekends, and his acute sense of physics and dedication to the experiment helped drive our progress. Also, I feel compelled to mention that he is a tenacious racquetball player with a wicked serve.

When I first arrived in the lab, Chih-Sung Chuu was the senior student working on the rubidium experiment. I am grateful for his guidance and patience as he explained how to operate, modify, and debug the apparatus, even while he was busy writing his dissertation. Kirsten Viering joined the experiment soon after I did. She is amazingly friendly and a great co-worker. Edvardas Narevicius was a very bright postdoc in the lab for my first two years. Although Ed didn't work directly on the rubidium experiment, we had many helpful discussions, and he was always more than willing to talk physics and share his expertise.

After my third year, we shut down the rubidium experiment and I began building the laser system for the hydrogen experiment. Adam Libson, Tom Mazur, and Isaac Chavez have been building the coilgun and magnetic trap for the experiment. They are all very knowledgeable and capable experimentalists. Julia Majors, an undergraduate student in the group, built the tellurium oven. She has enviable parallel parking skills and is really fun to hang out with. Rob Clark joined the group two years ago as a postdoc, and it has been great getting to know him and working with him.

Hrishikesh Kelkar, Tongcang Li, and David Medellin all worked on the sodium experiment. They have been tremendously helpful when I needed assistance troubleshooting and very generous when I needed to borrow optics or parts. Also, David has taught me more Spanish slang than I ever thought I would know.

One of my favorite aspects of graduate school, and in a broader sense

academia, is the diversity of the people who come together to discuss ideas, reach consensus, and expand knowledge. Through countless conversations and debates with my coworkers, I've gained invaluable perspective on science, politics, and the world in general. Along with Chih-Sung, Hrishi, Gabe, Tongcang, Kirsten, and David, it has been a pleasure to share the "international office" with Simon Kheifets and Jianyong Mo. Both have very promising futures ahead of them. Additionally, we've had a number of Würzburg exchange students in the lab. Max Riedel, Christian Parthey, and Christoph Schäff all did great work and had good stories to tell about Germany.

Shoupu Wan, Charlotte Sanders, Melissa Jerkins, Ioannis Keramidas, and Geneva White were members of the group with abbreviated tenures. Though our time together was short, they all contributed positively to the lab atmosphere.

As Isaac Newton once reminded us, progress comes only by building on the work of others. With that in mind, I am grateful to previous generations of students and postdocs in the lab who designed and built equipment, wrote code, and set up the infrastructure which helped to facilitate much of this research. There are too many to list completely, but in particular, Jay Hanssen, Todd Meyrath, and Florian Schreck were instrumental in setting up the rubidium BEC apparatus that would be converted into the apparatus used for this dissertation.

Jack Clifford, the student shop supervisor, has always been very friendly and helpful whenever I needed to machine something. I would also like to thank

our administrative staff. Olga Vera, Elena Simmons, and Marybeth Casias do a great job of keeping the lab running smoothly, whether it's through purchases, travel arrangements, or tamale lunches.

None of this would have been possible without the love and support of my parents. They are terrific people, and I am extremely thankful for their generosity and encouragement. Friday morning tea with them has kept me sane over the past five years and reminded me that there is more in this world than just lasers and basements.

Finally, I would like to thank the National Science Foundation for three years of financial support through the Graduate Research Fellowship Program.

S.T.B.

Austin, Texas

May 2011

Cooling Atomic Ensembles with Maxwell's Demon

Publication No. _____

Stephen Travis Bannerman, Ph.D.
The University of Texas at Austin, 2011

Supervisor: Mark G. Raizen

This dissertation details the development and implementation of novel experimental techniques for cooling neutral atoms. Based on a method first proposed by Maxwell in a nineteenth century thought experiment, these techniques reduce the entropy of an ensemble by allowing unidirectional transmission through a barrier and thus compressing the ensemble without doing work or increasing its temperature. Because of their general nature, these techniques are much more broadly applicable than traditional laser and evaporative cooling methods, with the potential to cool the vast majority of the periodic table and even molecules.

An implementation that cools in one dimension is demonstrated for an ensemble of magnetically trapped rubidium atoms which are irreversibly transferred to a gravito-optical trap. Analysis of the experimental results confirms that phase-space is completely compressed in one dimension. The results also indicate that the overall cooling performance is limited only by

the dynamics of atoms in the magnetic trap and may be improved with a more ergodic system.

Three-dimensional cooling may be accomplished with a modified technique which substitutes a radio-frequency-dressed magnetic trap for the gravito-optical trap. Application of this technique to atomic hydrogen and progress toward building an experimental apparatus are discussed.

Table of Contents

List of Figures

Chapter 1

Entropy and Demons

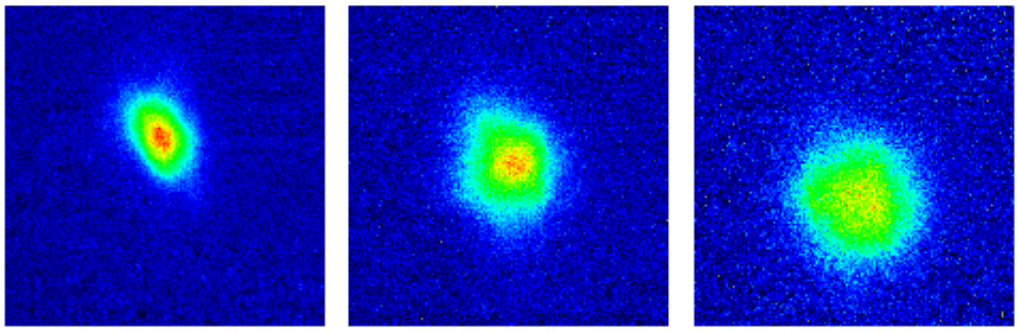

...the notion of dissipated energy could not occur to a being who could not turn any of the energies of nature to his own account, or to one who could trace the motion of every molecule and seize it at the right moment. It is only to a being in the intermediate stage, who can lay hold of some forms of energy while others elude his grasp, that energy appears to be passing inevitably from the available to the dissipated state.

-James Clerk Maxwell, 1878 [1]

1.1 The Second Law of Thermodynamics

In the mid-nineteenth century, Clausius, building off the work of Carnot, proposed the notion that, for any heat engine, there is a fundamental limit to how much heat can be converted into work and how much must be released into a cold reservoir [2]. Clausius made his theory more explicit over the years by defining a thermodynamic state variable whose variation, in any quasi-static process transforming a system from state A to state B, goes as

$$\Delta S = S_{\mathrm{B}} - S_{\mathrm{A}} = \int_A^B \frac{\delta Q}{T}, \tag{1.1}$$

where δQ is the inexact differential of the heat Q and T is the temperature of the system. For certain processes, termed reversible, this variation was zero, but for all the others it was positive. He designated the state variable S *entropy*. It is a straightforward exercise to show that in any cyclic process which produces work (such as that of a heat engine),

$$\Delta S = \oint \frac{\delta Q}{T} \geq 0. \tag{1.2}$$

This is the venerable Second Law of Thermodynamics–that entropy never decreases–and it has been regarded by many as holding "the supreme position among the laws of nature." [3]

With the advent of the atomistic picture of matter and the development of the theory of statistical mechanics in the 1870s, a more precise and simultaneously more curious definition of entropy was derived by Boltzmann [4]. It related the entropy of a gas to the number of possible configurations

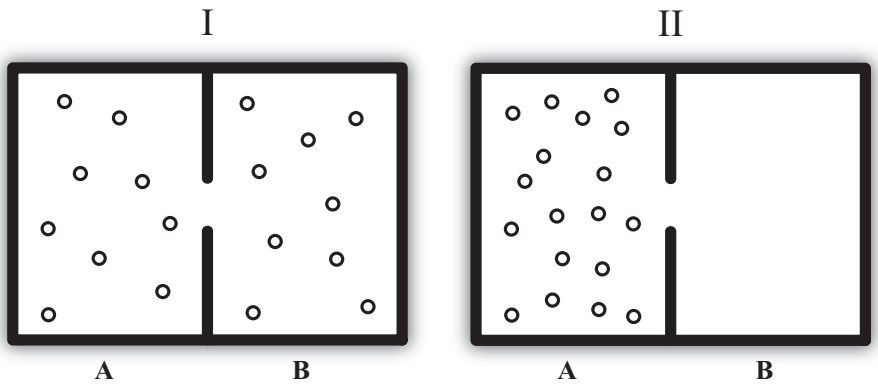

Figure 1.1: With the hole in the barrier between **A** and **B** open, System **I** can evolve to System **II** after enough time. However, if the hole is closed in **II**, then $\Omega_{\mathrm{II}} \subset \Omega_{\mathrm{I}}$, the entropy $S_{\mathrm{II}} < S_{\mathrm{I}}$, and a macroscopic violation of the Second Law has occurred.

that gas could be in, and it can be written succinctly:

$$S = k_{\mathrm{B}} \ln \Omega, \tag{1.3}$$

where k_{B} is Boltzmann's constant and Ω is the number of microstates accessible to the system.

In light of the fundamental postulate of statistical mechanics–that a system in thermal equilibrium is equally likely to occupy any one of Ω microstates consistent with its macrostate [5]–it became apparent that the Second Law could only hold statistically. Indeed, the observation of Brownian motion of pollen grains suspended in water soon demonstrated that transitory violations of the Second Law were possible [6]. However, violations on a macroscopic scale are ruled extremely improbable.

To see this, consider the vessel shown schematically in Figure 1.1. It

is divided into two identical chambers, **A** and **B**, by a barrier with a hole in the center. Imagine two scenarios: System **I** where an ideal gas of N atoms is evenly distributed between the two chambers, and System **II** where the same gas occupies only Chamber **A**. It should be immediately obvious that the number of microstates accessible to System **I** is twice that of System **II**. It follows then, from Equation 1.3, that $S_1 - S_2 = Nk_{\mathrm{B}} \ln 2 > 0$. This could be shown alternatively using the Sackur-Tetrode equation, which gives an explicit expression for the entropy of a monatomic ideal gas:

$$S = Nk_{\mathrm{B}} \left[\ln \left(\frac{V}{N} \left(\frac{4\pi mU}{3Nh^2} \right)^{3/2} \right) + \frac{5}{2} \right], \tag{1.4}$$

where V is the volume occupied by the gas, m is the atomic mass, U is the internal energy of the gas, and h is Planck's constant.

If the hole in the center of the barrier is left open, then **I** and **II** are microstates of the same macrostate, and so $S_{\mathrm{I}} = S_{\mathrm{II}}$. Thus there is some non-zero probability that System **I** will spontaneously compress entirely into Chamber **A**. By simply closing the hole at this point, entropy is reduced. But a simple calculation [7] shows that, for one mole of hydrogen atoms at room temperature in a box with 1 meter sides, it would take on the order of $10^{6\times 10^{22}}$ times the age of the universe before such a compression would spontaneously occur. It would be an understatement to say that the Second Law of Thermodynamics is effectively safe from this type of macroscopic violation.

1.2 Maxwell's Demon

Contemplating the statistical nature of the Second Law, Maxwell penned a letter to his colleague Tait in 1867. In the letter, he proposed a thought experiment with a "very observant and neat-fingered being" that could lower the entropy of a gas in a simple way [8]. Later christened 'demons' by William Thomson [9], these creatures and their interpretation have been a source of agitation and debate for over a century.

1.2.1 The Demon

Although Maxwell's first conception of the demon was of an intelligent being that could sort gas molecules according to their velocities, he subsequently described a less intelligent being that lowered entropy simply by functioning as one-way valve. Figure 1.2 illustrates this demon.

As in the scenario illustrated in Figure 1.1, a gas of atoms (or molecules) is contained in a two-chambered vessel. Here, a hole in the barrier dividing this box may be opened and closed with a massless gate. The demon observes the atoms and operates the gate and allows atoms to pass from **B** to **A** but not from **A** to **B**. No work is performed operating the door, yet the gas is compressed to half its volume. The upshot is a reduction of entropy, evident from Equations 1.3 and 1.4, in clear violation of the Second Law.

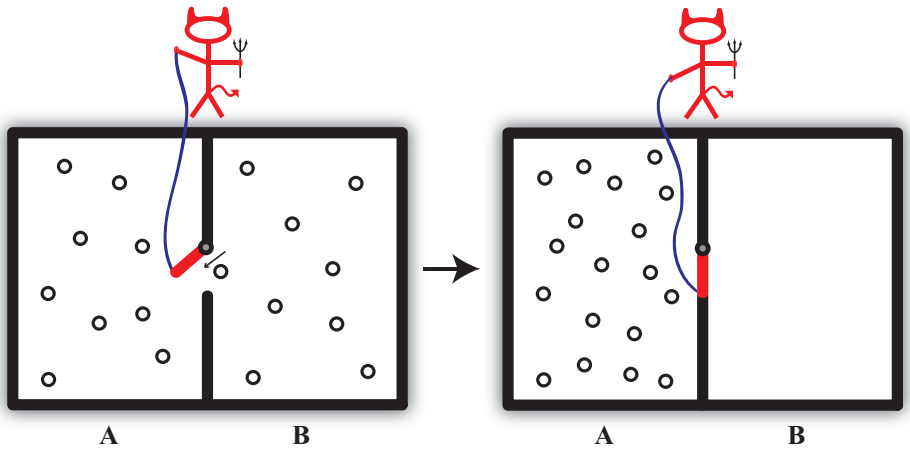

Figure 1.2: Maxwell's pressure demon lowers the entropy of a gas by allowing atoms to pass unidirectionally through a gate. Though no work is done in operating the gate, the gas occupies a smaller volume with reduced entropy after some time has elapsed.

1.2.2 Exorcisms

Ever since the introduction of the demon, physicists have fought to save the Second Law from it through various 'exorcisms.' The most common approach has been to naturalize the demon, assume the Second Law holds, and locate the missing entropy. In many respects, this tradition began in 1929 with Szilard's one molecule heat engine [10], his own incarnation of Maxwell's demon. Szilard emphasized that, in order to operate, the demon must make a measurement and glean information from the molecule. This measurement, he claimed, was invariably accompanied by an entropy increase that would compensate for the decrease in the entropy of the molecule.

Building off of Szilard's work, Brillouin [11, 12] and Gabor [13] analyzed in detail the entropy costs associated with using light as a measurement

device. Later, Bennett would show that certain measurements can be made isentropically [14]. A physical demon, however, must store the results of this measurement in a finite memory. At some point, the memory must be erased, and there is an unavoidable entropy cost associated with this erasure [15].

All of these exorcisms imply an intrinsic link between information and thermodynamic entropy. This interpretation seems natural today in light of the theory of information developed by Shannon [16] and Jaynes [17]. Even Lewis stated in 1930 that "gain in entropy always means loss of information, and nothing more" [18]. Yet many have contended that the arguments invoking information theory to exorcise the demon are circular and unnecessary, merely a reframing of the Second Law using the formalism of information theory [19–21]. Indeed, if one assumes from the outset that the demon is governed by the laws of thermodynamics, then there is no need to make any further suppositions to save the Second Law.

To this day, there is considerable controversy and debate as to whether the demon has been satisfactorily exorcised, largely due to the disparity of proposed demons and disagreement over various assumptions fundamental to their operation and interpretation. While it is surely a worthwhile pursuit to resolve the controversy for a deeper understanding of thermodynamics and information, proxies for the demon (i.e., experiments which operate in close resemblance to the original demon but do work, dissipate energy, or fail to violate any laws) have been realized that stochastically cool particles circulating in accelerator rings [22, 23], create Brownian ratchets [24], and cool gases of

neutral atoms [25]. The last example is the subject of this dissertation.

1.3 The Atomic One-Way Valve

Proposals for physical implementations of atomic one-way valves began in 2005 with a conceptual paper by Raizen *et al.* [26]. A related concept for the rectification of atomic currents was independently developed and proposed soon after this paper was submitted for publication [27]. The proposals were advanced and studied in a series of papers [28–31], and in 2008 the first one-way valve was demonstrated experimentally by the Raizen Group [32]. An alternate implementation of the valve was demonstrated shortly thereafter by a separate research group [33]. Subsequently, the compression limit of the valve has been analyzed and reached [34], and its application toward molecules has been discussed [35].

1.3.1 Implementation

The asymmetric nature of the one-way valve necessitates a non-Hermitian Hamiltonian due to the reversibility of microscopic laws. This may be accomplished by the irreversible dissipation of energy into an external reservoir, ideally one which has negligible interaction with the system under consideration. All implementations of the one-way valve cited herein meet this requirement through the irreversible and spontaneous scattering of a single photon to the environment. This photon effects a change in the atom's internal state, resulting in a different potential landscape that prohibits reverse motion. A precise

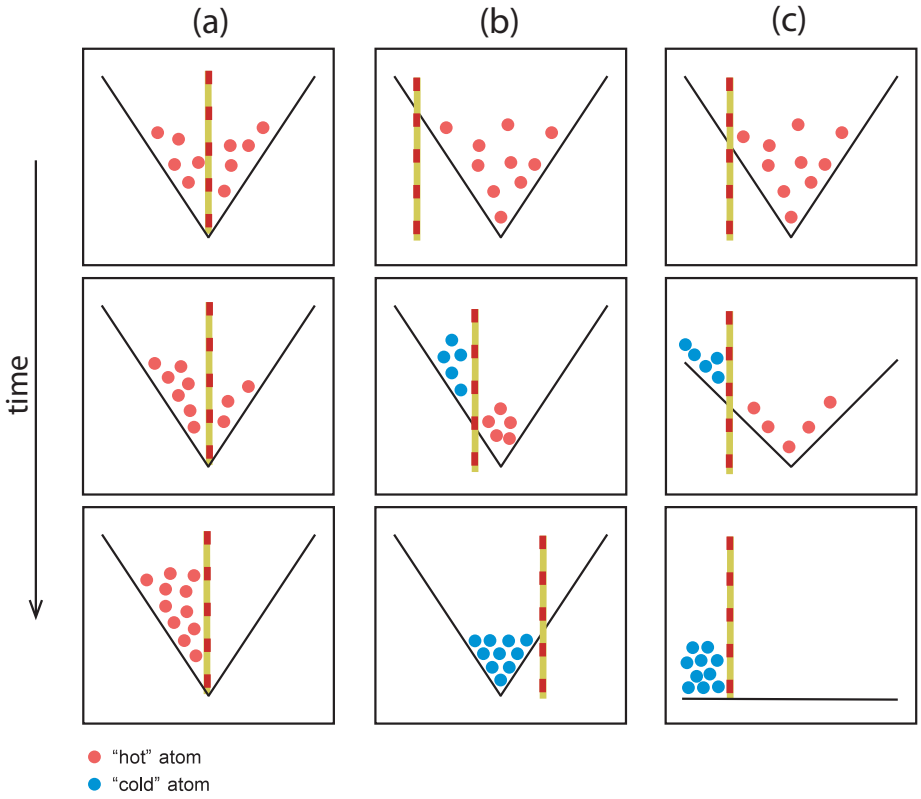

Figure 1.3: Maximizing entropy reduction with Maxwell's pressure demon in a gradient confining potential. (a) Maxwell's original pressure demon allows unidirectional passage through a barrier. (b) A gradient potential with a moving demon. (c) A collapsing gradient potential with a stationary demon.

description of this process will be given in Chapters 4 and 5.

Although the one-way valve is of interest from the standpoint of Maxwell's demon, a promising application is for its use as a cooling technique. Toward this end, several slight modifications can be made, with respect to Maxwell's original thought experiment, to maximize the entropy reduction. Using Equation 1.4, one can write the entropy reduction between two arbitrary states of

an ideal gas:

$$|\Delta S| = |S_f - S_i| = N k_{\mathrm{B}} \ln \left[\frac{V_i U_i^{3/2}}{V_f U_f^{3/2}} \right], \tag{1.5}$$

where the subscripts f and i refer to the final and initial states, respectively. The entropy reduction can thus be maximized by minimizing both the final volume V_f and the final internal energy U_f. The method by which both of these quantities are minimized is illustrated in Figure 1.3.

With Maxwell's original demon, the valve is located at the center of a flat potential. The internal energy is unchanged while the volume is compressed by a factor of two, resulting in $|\Delta S| = N k_B \ln 2$. However, by introducing a gradient potential and positioning the valve just beyond the classical turning points of the most energetic atoms, two beneficial effects can occur: First, by slowly translating the demon (Figure 1.3b) or collapsing the potential (Figure 1.3c), atoms transit the valve only when they are near their classical turning points. In fact, by extending the translation or collapse time, the ratio U_f/U_i may be made arbitrarily small[1]. Second, the final volume of the gas is now dependent only on the residual internal energy. To the extent that U_f/U_i can be made arbitrarily small, so too can V_f/V_i. The result is a nearly complete reduction of entropy.

[1]Because each atom must scatter a photon as it transits the valve, this is not strictly true. The photon imparts a small momentum kick on the atom, resulting in a minimum achievable residual energy. This energy is typically negligible in the experiments described in this dissertation, but it will be cited when relevant.

1.3.2 A Single Scattered Photon

It is worthwhile to make a few remarks on the role played by the scattered photon in this implementation of Maxwell's demon. Indeed, when compared to other laser cooling techniques, the fact that only a single photon per atom is required to accomplish significant cooling presents a huge advantage in regard to generality and applicability. Appropriately, the technique has been called *single-photon cooling* to emphasize its distinction.

The irreversibility of single-photon cooling is dependent on the non-degeneracy of the initial and final atomic states. In this way, it is the scattered photon which either carries away the liberated kinetic energy of the gas or stores that energy in the atom's internal structure, thereby satisfying conservation of energy. But what of the Second Law? A suitable analogy is the spontaneous crystallization of a super-cooled melt [36]. The configurational entropy of the atoms in the melt is lowered by forming a lattice structure, necessitating the transfer of an equal amount of entropy to another reservoir. This occurs through the disordered excitation of crystal vibrational modes by the liberated latent heat. With single-photon cooling, the one-way valve lowers the configurational entropy of the gas by compressing it, and this entropy decrease is compensated by an increase in the disorder of the radiation field.

In the context of the informational interpretation of Maxwell's demon, single-photon cooling can be thought of as informational cooling. Each scattered photon represents a measurement of an atom's position at a particular time, and thus it contains information that specifies the atom's position in

phase-space. In principle, the scattered photons could be collected and stored, yielding complete information on the ensemble's energy distribution. The original ensemble could then be reversibly reconstructed. In practice, the scattered photons are immediately discarded. Unlike the demons considered in the tradition of Szilard and Bennett [37], the information contained in the photons need not be stored or processed. The operation of the valve is automatic; it is as if the demon makes a measurement and immediately erases its memory.

It is also interesting to look at the efficiency of single-photon cooling's information use. Whereas other informational cooling techniques, such as stochastic cooling, radiate an enormous amount of information compared to the amount collected and used for cooling, single-photon cooling is maximally efficient in this sense. The reduction of atomic entropy is exactly balanced by the information entropy of the scattered photon [30].

Chapter 2

Cold Atomic Gases

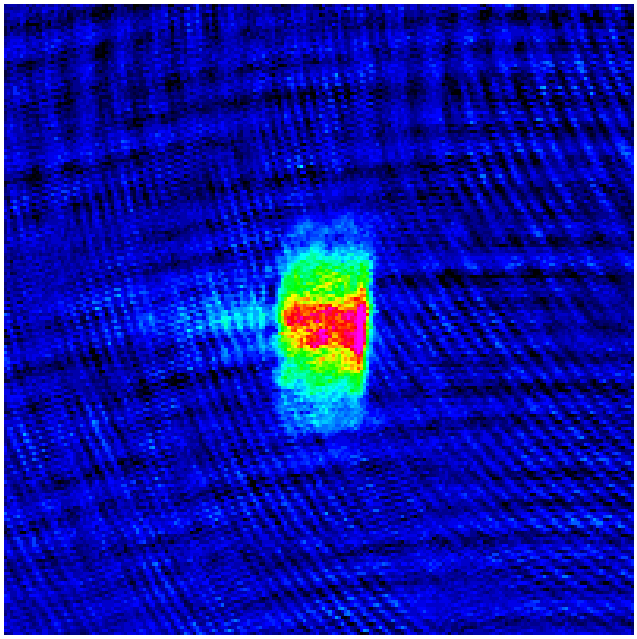

"A physicist is just an atom's way of looking at itself."

-Niels Bohr

2.1 Overview

The proposition that matter is composed of indivisible particles can be traced back to the Greek philosopher Democritus, circa 400 BCE [38].

Nevertheless, it took more than two millennia before the scientific community accepted the atomic hypothesis, due in no small part to the considerable technical challenges concomitant with isolating and probing matter on such a minute scale. In the first half of the twentieth century, physicists made great strides in understanding the atomic structure, but few experimental tools were available for comprehensive control over atoms in the laboratory.

With the advent of the laser in 1960 [39, 40], the field of atomic physics was radically transformed. Physicists had been aware of the mechanical effects of radiation on matter since the days of Kepler [41], but the laser gave experimentalists unprecedented control over the radiation field. It was proposed that this control could in turn be harnessed to dissipate energy in the external degrees of freedom of atoms, cooling a gaseous ensemble with precisely tuned laser radiation [42, 43]. Cooling schemes relying upon atomic doppler shifts were quickly realized with trapped ions [44, 45], and neutral atoms soon followed suit [46, 47].

Since this time, laser-cooled atomic gases at sub-millikelvin temperatures have proven to be a rich and diverse testbed for fundamental physics as well as for a variety of applications. Investigations into long-standing questions of thermodynamics, one of which is the focus of this dissertation, have been made possible with cold atoms. They have enabled the study of novel thermodynamical systems such as Bose-Einstein condensation [48, 49] and degenerate Fermi gases [50]. Furthermore, precision measurements of electric dipole transitions in cold atoms have provided tests of quantum electrody-

namics to extreme levels of accuracy.

Cold atoms are also the basis for a variety of promising applications. Interferometers exploiting the thermal de Broglie wavelength of atoms are potentially the most sensitive gyroscopes today [51]. Optical frequency standards accurate to a part in 10^{16} have been demonstrated by interrogating narrow electronic transitions in clouds of cold calcium and strontium [52]. Additionally, the field of quantum information has the potential to revolutionize modern computation and communication by exploiting the quantum mechanical nature of cold atoms [53].

2.2 Entropy and Cooling

To the extent that the term 'cooling' refers simply to reducing the temperature of a gas, it is a fairly uninteresting concept in atomic physics. By reversibly expanding a trapped gas, its temperature decreases at the cost of a decrease in density. This process is isentropic and essentially trivial. Therefore 'cooling' is typically used colloquially among atomic physicists to refer to a reduction of entropy. This encompasses processes that decrease temperature at a constant density, increase density at a constant temperature, or simultaneously decrease the temperature and increase the density.

A figure of merit customarily used in the context of cold atoms and cooling experiments is phase-space density, rather than entropy. Phase-space density is defined as the product of the atomic density and the cube of the

System	$n\,(\mathrm{cm}^{-3})$	T (K)	ρ
Atmospheric nitrogen	10^{22}	300	10^{-7}
Liquid nitrogen	10^{25}	77	10^{-5}
Laser cooled atoms	10^{11}	10^{-5}	10^{-6}
Bose-Einstein condensation	10^{15}	10^{-7}	1

Table 2.1: Estimates of phase-space density for various systems.

thermal de Broglie wavelength:

$$\rho \equiv n\Lambda_{\mathrm{dB}}^3 = \frac{N}{V}\left(\frac{h^2}{2\pi m k_{\mathrm{B}} T}\right)^{3/2}. \tag{2.1}$$

It is easy to see that this quantity is closely (though inversely) related to entropy by noting that $U = \frac{3}{2}Nk_{\mathrm{B}}T$ in Equation 1.4. Thus the following statements may be taken as equivalent, at least for the purposes of this dissertation:

1. The atomic ensemble has been cooled.

2. The entropy of the ensemble has decreased.

3. The phase-space density of the ensemble has increased.

To get a sense of how phase-space density scales, Table 2.1 gives approximate values for several systems.

Evolution of the phase-space density in Hamiltonian systems is governed by Liouville's theorem [54], which states that $d\rho/dt = 0$. A conservative system flows through phase-space with constant density. Even with time dependent terms in the Hamiltonian, phase-space density cannot increase [55],

although schemes relying on collisional interactions may allow local increases [56].

The bottom line is that real cooling, or an overall increase in phase-space density, is nontrivial and impossible without some sort of irreversible dissipation. Historically, it has been a grand challenge to devise experimentally viable schemes of this nature.

2.3 Interactions Between Atoms and External Fields

The development of the quantum mechanical theory of matter in the early twentieth century, along with progress in the understanding of the internal structure of atoms, have resulted in a detailed understanding of the interactions between atoms and external electromagnetic fields. Experimentalists have, for some time now, used these interactions to manipulate both the internal states as well as the external degrees of freedom of atomic ensembles. This section will detail the main interactions that are relevant to this dissertation.

2.3.1 Resonant light

The most common tool used by experimentalists for manipulating the internal states of atoms is resonant light. Because photons carry momentum, a scattering force also arises from resonant absorption and emission.

The optical Bloch equations describe the interaction between a classical monochromatic optical field and an ensemble of quantum two-level atoms. An

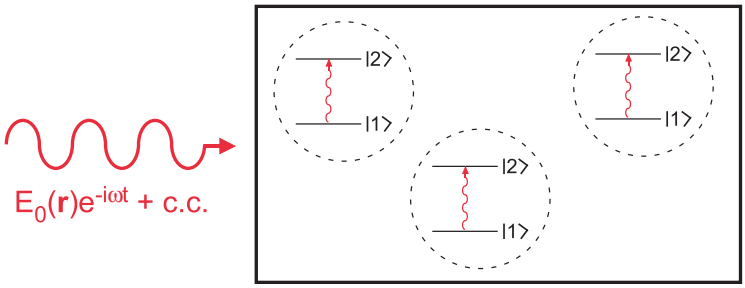

Figure 2.1: Monochromatic radiation field incident on an ensemble of two-level atoms.

excellent derivation and discussion of these equations is given in References [57–59]. Here only the main results that are relevant for the present work are highlighted.

Consider an ensemble of two-level atoms, with ground state $|1\rangle$ and excited state $|2\rangle$. When irradiated by a monochromatic field of frequency ω, which is close to the ensemble's resonant frequency ω_{12}, the atoms may make a transition to state $|2\rangle$ by the stimulated absorption of a photon. From the excited state, they will decay back to $|1\rangle$ either by spontaneous or stimulated emission of another photon. The net spontaneous scattering rate for each atom may be written

$$R = \frac{\Gamma}{2} \frac{I/I_{\mathrm{s}}}{1 + I/I_{\mathrm{s}} + (2\delta/\Gamma)^2}, \tag{2.2}$$

where Γ is the natural linewidth (decay rate) of the excited state, I is the intensity of the driving field, I_{s} is referred to as the saturation intensity, and $\delta = \omega - \omega_{12}$ is the detuning of the field from the atomic resonance. The

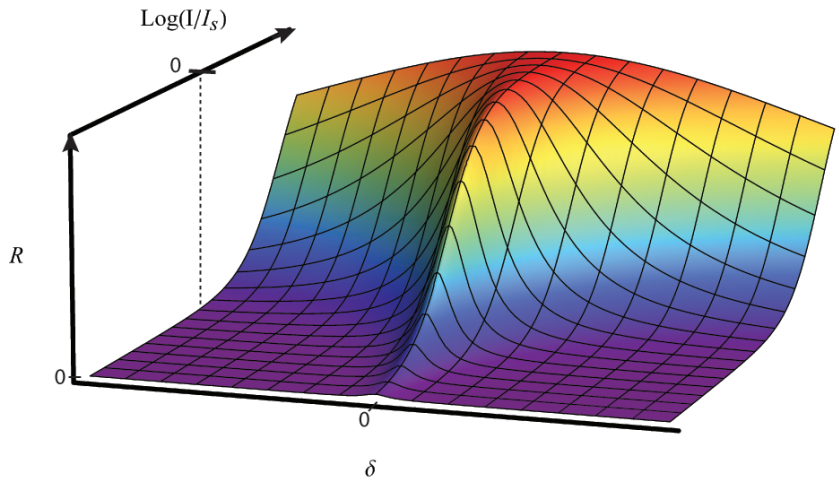

Figure 2.2: Scattering rate as a function of detuning and saturation parameter I/I_s. As the intensity increases, the effective linewidth becomes broader, and transitions can be driven away from resonance.

saturation intensity I_s is given by

$$I_s = \frac{\epsilon_0 c \Gamma^2 \hbar^2}{4|\hat{\mathbf{e}} \cdot \boldsymbol{\mu}|^2}, \tag{2.3}$$

where $\hat{\mathbf{e}}$ is the polarization vector of the electric field and $\boldsymbol{\mu} = -e\mathbf{r}$ is the microscopic polarization operator. I_s is significant in that it corresponds to the intensity at which the Rabi frequency is comparable to the decay rate of the excited state and the excited state population is half its maximum. For the D_2 ($F = 2 \rightarrow F' = 3$) transition of rubidium 87, $I_s = 3.58\,\mathrm{mW/cm^2}$ for isotropic light polarization [60]. A comparable parameter has been be derived for the $1S \rightarrow 2S$ two-photon transition of hydrogen, and its value is $0.89\,\mathrm{W/cm^2}$ [61].

Figure 2.2 is a plot of Equation 2.2 for a range of detunings δ and saturation parameters I/I_s. The scattering rate is a Lorentzian centered about

the atomic resonance, with a width that increases with increasing saturation parameter. The full width at half-maximum (FWHM) of this Lorentzian is given by [62]

$$\Delta\omega_{\mathrm{FWHM}} = \Gamma\left(1 + \frac{I}{I_{\mathrm{s}}}\right)^{1/2}. \tag{2.4}$$

This phenomenon is known as *power broadening*. Experimentally, it may be utilized to drive atomic transitions effectively using off-resonant light.

2.3.1.1 Optical Molasses

Because a photon carries with it a certain amount of momentum ($\mathbf{p} = \hbar\mathbf{k}$, where $\mathbf{k}$ is the wavevector of the light), each absorbed and scattered photon imparts a momentum kick to the atom. For a large number of scattering events, the momentum kicks from photons emitted spontaneously in random directions average out to zero. The result is a net scattering force, due to the absorbed photons, in the direction of the light propagation

$$\mathbf{F}_{\mathrm{sc}} = R\hbar\mathbf{k}, \tag{2.5}$$

where R is the scattering rate of Equation 2.2.

For a light source such as a laser, the direction of this force can be precisely controlled. Furthermore, the frequency dependence of this force can be exploited in conjunction with the Doppler effect to form the basis of nearly all laser cooling schemes. In its simplest form, it is known as 'optical molasses.'

Consider a two-level atom at rest in a field comprising two counter-propagating laser beams (Figure 2.3a). The lasers are red-detuned from the

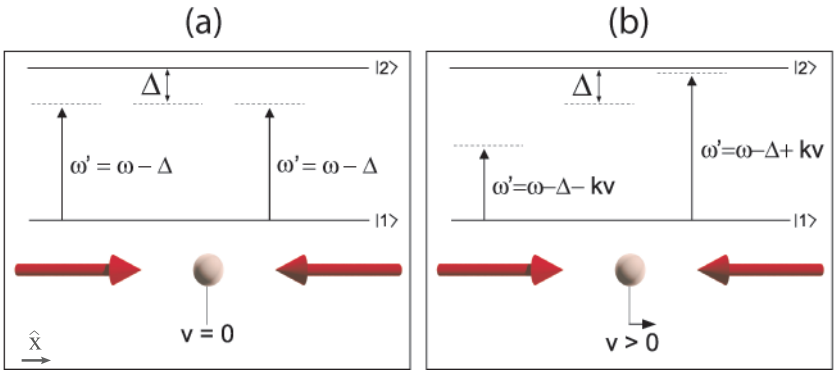

Figure 2.3: Optical molasses incident on (a) an atom at rest and (b) an atom with positive velocity. The moving atom scatters more photons from the left-propagating beam, resulting in a viscous damping force.

atomic resonance by an amount $\delta = \omega - \omega_{12}$. The detuning is said to be red (blue) when δ is negative (positive). The net force on the atom is given by

$$\begin{aligned} \mathbf{F}_{\text{net}} &= \mathbf{F}_{\text{sc}}^{+} + \mathbf{F}_{\text{sc}}^{-} \\ &= \hbar k \frac{\Gamma}{2} \frac{I}{I_{\text{s}}} \left[\frac{1}{1 + I/I_{\text{s}} + (2\delta_{+}/\Gamma)^2} - \frac{1}{1 + I/I_{\text{s}} + (2\delta_{-}/\Gamma)^2} \right] \hat{\mathbf{x}}, \end{aligned} \quad (2.6)$$

where the first (second) term on the right hand side of the equation corresponds to the force generated by the right-propagating (left-propagating) laser beam.

Because the scattering force (2.2) is in the direction of the laser propagation, it is clear that the forces from the two beams on an atom at rest will cancel each other out, provided they have equal intensities and detunings. However, in the case that the atom has a finite velocity $\mathbf{v}$ (Figure 2.3b), the atom sees two different effective laser detunings due to the Doppler shift $\mathbf{k} \cdot \mathbf{v} = \mp kv$:

$$\delta_{\pm} = \delta \mp kv. \quad (2.7)$$

This asymmetry induces a non-zero net force. Indeed, an atom with non-zero velocity sees one beam blue-shifted (toward resonance) and the other red-shifted (further away from resonance). It scatters more photons out of the blue-shifted beam, resulting in a net force that acts against the atomic motion.

This can be shown more explicitly by Taylor-expanding Equation 2.6 in the small velocity limit ($v \ll \delta/k$). The result to first order is

$$\mathbf{F}(\mathbf{v}) = \frac{4\hbar k(I/I_{\mathrm{s}})(2\delta/\Gamma)}{\left(1 + I/I_{\mathrm{s}} + (2\delta/\Gamma)^2\right)^2} k\mathbf{v}. \tag{2.8}$$

Given a red-detuned laser, $\delta < 0$ and Equation 2.8 can be rewritten

$$\mathbf{F}(\mathbf{v}) = -\beta\mathbf{v}. \tag{2.9}$$

It is immediately clear that this is a damping force similar to that of a particle in a viscous fluid. Hence the name, optical molasses.

This scheme may be trivially scaled up to three dimensions. With the inclusion of particular magnetic fields and beam polarizations, a magneto-optical trap (MOT) can be created that both cools and trap the atoms [63]. MOTs have become one of the workhorses of the cold-atom community, and little else will be said about them here except to note Reference [57] and mention that they are used in preparing the rubidium atoms for the cooling experiments.

2.3.1.2 Branching Ratios

Thus far, the discussion has assumed that each atom has only two accessible quantum states. Needless to say, this is an idealization often far

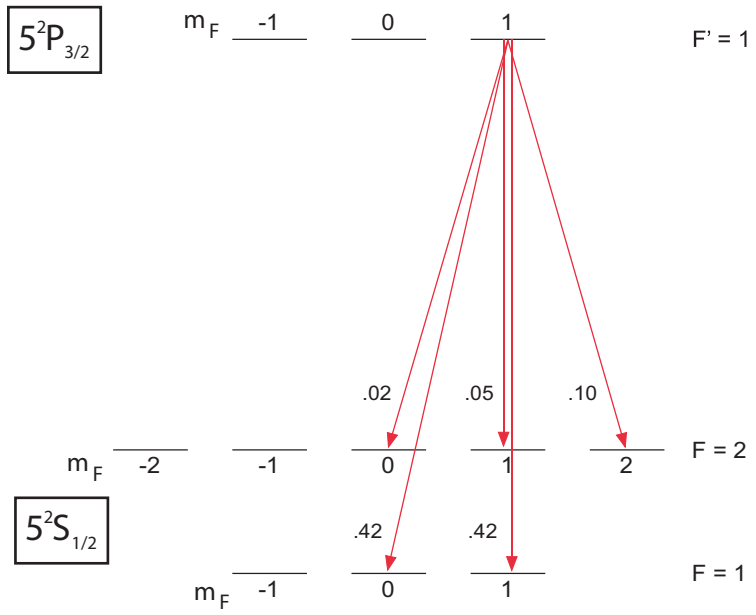

Figure 2.4: Branching ratios for a rubidium 87 transition.

from the truth. It is often the case that an excited atom spontaneously decays not to its original state, but, for example, to a different hyperfine state. This process has been the bane of traditional laser cooling, but it will be shown to be essential for the success of single-photon cooling.

Electric dipole selection rules limit the possible decay channels of any particular excited state, but one can predict with greater certainty the relative probabilities of allowable spontaneous transitions. These decay probabilities are known as *branching ratios*. Consider the spontaneous decay of a photon from a rubidium 87 atom in the excited $5^2P_{3/2}\,|F' = 1, m'_F = 1\rangle$ state (Figure 2.4). The relevant selection rules for this transition, $\Delta F = 0, \pm 1$ and $\Delta m_F = 0, \pm 1$, yield five possible final states.

To determine the relative strengths of each of these transitions, the Wigner-Eckhart theorem may be employed to produce the relation [64, 65]

$$\langle F, m_F|\mu_q|F', m'_F\rangle = \langle F\|\mu\|F'\rangle(-1)^{F'-1+m_F}\sqrt{2F+1}\begin{pmatrix} F' & 1 & F \\ m'_F & q & -m_F \end{pmatrix}, \tag{2.10}$$

where $|F, m_F\rangle$ ($|F', m'_F\rangle$) are the ground state (excited state) hyperfine quantum numbers, μ_q is the q component of the spherical electric dipole operator, and the quantity in parentheses is a Wigner 3-j symbol. Applying the Wigner-Eckhart theorem again allows one to rewrite this equation with the F and F' dependence factored into a Wigner 6-j symbol:

$$\langle F\|\mu\|F'\rangle = \langle J\|\mu\|J'\rangle(-1)^{F'+J+1+I}\sqrt{(2F'+1)(2J+1)}\begin{Bmatrix} J & J' & 1 \\ F' & F & I \end{Bmatrix}. \tag{2.11}$$

The matrix element $\langle J\|\mu\|J'\rangle$ can be determined using the relation

$$\frac{1}{\tau} = \frac{\omega_{12}^3}{3\pi\epsilon_0\hbar c^3}\frac{2J+1}{2J'+1}|\langle J\|\mu\|J'\rangle|^2, \tag{2.12}$$

where τ is the lifetime of the excited state.

Using these relations, the normalized branching ratios are calculated and shown in Figure 2.4 next to each red arrow representing possible decay channels.

2.3.2 Light Shifts

When an atom interacts with light that is detuned far from resonance, the scattering rate becomes negligible, and the dominant effect is a shift in the

atom's internal energy. This shift may be exploited by applying gradient fields, such as that of a Gaussian laser beam, which result in nearly-conservative forces and potentials. First proposed for neutral atoms in 1962 by Askar'yan [66] and demonstrated in 1986 by Chu *et al.* [67], trapping potentials based on light shifts (so-called optical dipole traps) are now commonplace in the cold atom community due to their simplicity and flexibility.

A detailed discussion of light shifts and the optical dipole force is given in [68]. To understand the interaction between far-detuned light and an atom, consider the atomic dipole moment ($\mathbf{p}(\mathbf{r},t) = \hat{\mathbf{e}}\tilde{p}(\mathbf{r})\exp(-i\omega t) + c.c.$) induced by the electric field of the light ($\mathbf{E}(\mathbf{r},t) = \hat{\mathbf{e}}\tilde{E}(\mathbf{r})\exp(-i\omega t) + c.c.$). The dipole moment and field amplitudes are related by the complex polarizability α as follows:

$$\tilde{p} = \alpha\tilde{E}. \tag{2.13}$$

The interaction potential for this system is

$$U_{\text{dip}} = -\frac{1}{2}\langle \mathbf{p}\cdot\mathbf{E}\rangle = -\frac{1}{2\epsilon_0 c}\,\text{Re}(\alpha)I, \tag{2.14}$$

where $I = \frac{1}{2}\epsilon_0 c|\tilde{\mathbf{E}}|^2$ is the intensity of the field. It is straightforward to calculate the dipole force:

$$\mathbf{F}_{\text{dip}}(\mathbf{r}) = -\nabla U_{\text{dip}}(\mathbf{r}) = \frac{1}{2\epsilon_0 c}\,\text{Re}(\alpha)\nabla I. \tag{2.15}$$

The complex polarizability α may now be calculated by integrating the equation of motion for the classical damped, driven harmonic oscillator

$$\ddot{x} + \Gamma_\omega \dot{x} + \omega_0^2 x = \frac{-eE(t)}{m_e} \tag{2.16}$$

and inserting Larmor's formula for the power radiated by an accelerating charge [69]:

$$\Gamma_\omega = \frac{e^2\omega^2}{6\pi\epsilon_0 m_e c^3}. \tag{2.17}$$

Solving for the polarizability gives

$$\alpha = 6\pi\epsilon_0 c^3 \frac{\Gamma/\omega_0^2}{\omega_0^2 - \omega^2 - i(\omega^3/\omega_0^2)\Gamma}, \tag{2.18}$$

where $\Gamma \equiv \Gamma_{\omega_0}$. This expression is valid for the case of negligible saturation and large detuning. General equations for the dipole potential and the scattering rate may now be written:

$$U_{\rm dip}(\mathbf{r}) = -\frac{3\pi c^2}{2\omega_0^3}\left(\frac{\Gamma}{\omega_0 - \omega} + \frac{\Gamma}{\omega_0 + \omega}\right) I(\mathbf{r}) \tag{2.19}$$

and

$$R_{\rm dip}(\mathbf{r}) = \frac{3\pi c^2}{2\hbar\omega_0^3}\left(\frac{\omega}{\omega_0}\right)^3 \left(\frac{\Gamma}{\omega_0 - \omega} + \frac{\Gamma}{\omega_0 + \omega}\right)^2 I(\mathbf{r}). \tag{2.20}$$

Typically, the second term in parentheses of Equations 2.19 and 2.20 can be neglected (the rotating wave approximation), and the equations may be simplified to

$$U_{\rm dip}(\mathbf{r}) = \frac{3\pi c^2}{2\omega_0^3}\frac{\Gamma}{\delta} I(\mathbf{r}) \tag{2.21}$$

and

$$R_{\rm dip}(\mathbf{r}) = \frac{3\pi c^2}{2\hbar\omega_0^3}\left(\frac{\Gamma}{\delta}\right)^2 I(\mathbf{r}), \tag{2.22}$$

where, as before, $\delta = \omega - \omega_0$ is the detuning from resonance.

There are two features of Equations 2.21 and 2.22 that merit closer examination. The first is that the potential $U_{\rm dip}$ scales as I/δ while the scattering

rate R_{dip} scales as I/δ^2. This means that strong potentials with negligible scattering can be formed by fields with large detunings and high intensities. The second is that the sign of the potential depends solely on the sign of the detuning δ. Thus, for red detuning, an atom will experience an attractive force. Conversely, for blue detuning, an atom will experience a repulsive force. In this way, atoms may be trapped at red-detuned field maxima or blue-detuned field minima.

2.3.3 Zeeman effect

Just as the internal energy of an atom with an (induced) electric dipole moment is raised or lowered by an external electric field, an atom with a magnetic dipole moment experiences energy shifts in the presence of an external magnetic field. This effect, first explored by Zeeman [70], is routinely used to trap neutral atoms at local magnetic field minima [71].

The total magnetic moment of an atom is given by the sum of its electronic and nuclear moments

$$\boldsymbol{\mu} = -\mu_B(g_J\mathbf{J} + g_I\mathbf{I}), \tag{2.23}$$

where $\mu_B = e\hbar/2m_e \cong h \cdot 1.4\,\mathrm{MHz/G}$ is the Bohr magneton, $\mathbf{J}$ and $\mathbf{I}$ are the electronic angular momentum and nuclear spin, respectively, and g_J (g_I) is the electronic (nuclear) Landé g-factor. Here $\mathbf{J} = \mathbf{L} + \mathbf{S}$ is the vector sum of the electronic orbital angular momentum $\mathbf{L}$ and spin $\mathbf{S}$.

The Hamiltonian for the Zeeman interaction $H_{\mathrm{Z}} = -\boldsymbol{\mu} \cdot \mathbf{B}$ may be

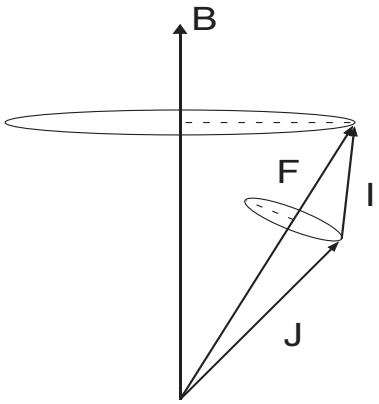

Figure 2.5: Vector model of hyperfine coupling. The vector sum of the electronic orbital angular momentum, electronic spin, and nuclear spin precesses about the axis aligned with the magnetic field.

diagonalized in the so-called hyperfine basis $\{|F, m_F\rangle\}$, where $\mathbf{F} = \mathbf{J} + \mathbf{I}$. This coupling is shown pictorially in Figure 2.5. The hyperfine basis vectors are eigenvectors of the operators F^2 and F_z, with the latter being the angular momentum operator projected along the axis of the local magnetic field.

For a given hyperfine manifold with total angular momentum F, there are $2F + 1$ projections labeled by m_F. The energy shift of each sublevel, in the low-field regime, can be written

$$U_{\mathrm{Z}} = \mu_B g_F m_F |B|. \tag{2.24}$$

Figure 2.6 depicts the Zeeman effect for rubidium atoms in the $5^2S_{1/2}$ ground state.

By removing the vector dependence of Equation 2.24, it is assumed that the magnetic dipole moment is aligned with and precessing about the direction of the magnetic field. Experimentally, an atom's magnetic moment

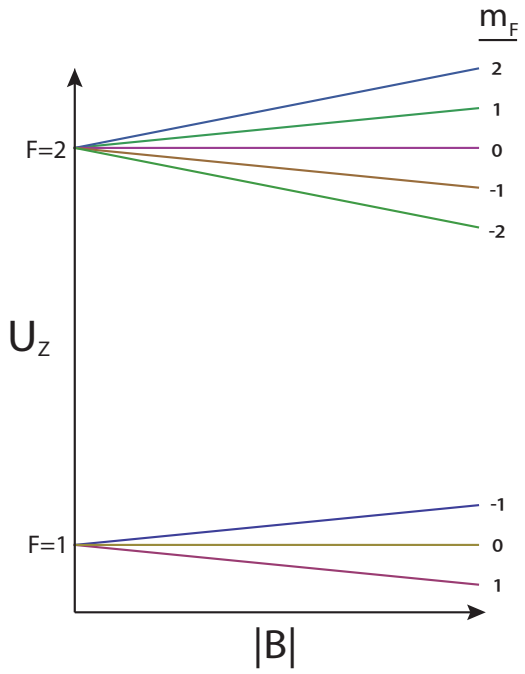

Figure 2.6: Low-field Zeeman shifts for F=1 and F=2 hyperfine manifolds of ^{87}Rb.

will adiabatically follow an inhomogeneous or time-dependent field as long as the following condition holds: $\omega_L \gg |\dot{B}/B|$, where $\omega_L = U_Z/\hbar$ is the Larmor precession frequency and $\dot{B}$, for a static magnetic field, arises from the atomic motion across a spatially inhomogeneous field. When this condition is violated, Majorana spin flips can occur.

It can be seen from Equation 2.24 that there are three classes of magnetic states. Those for which the product $g_F m_F > 0$ are referred to as low-field seekers. The energy of atoms in these states increases with increasing magnetic field strength. Given a magnetic field gradient, these atoms will be forced toward regions of lower field strength. Conversely, the states for which

the product $g_F m_F < 0$ are referred to as high-field seekers. Atoms in these states will be forced toward regions of high field strength. Finally, there is a magnetically decoupled state $m_F = 0$ which experiences no energy shifts and therefore feels no forces from a magnetic gradient.

In principle, a magnetic confining potential could be created to trap either low-field or high-field seekers at field extrema. However, Maxwell's equations forbid the presence of local magnetic field maxima in free space [72]. Thus it is the low-field seekers, those for which the product $g_F m_F > 0$, that are magnetically trappable.

Chapter 3

The Rubidium Apparatus

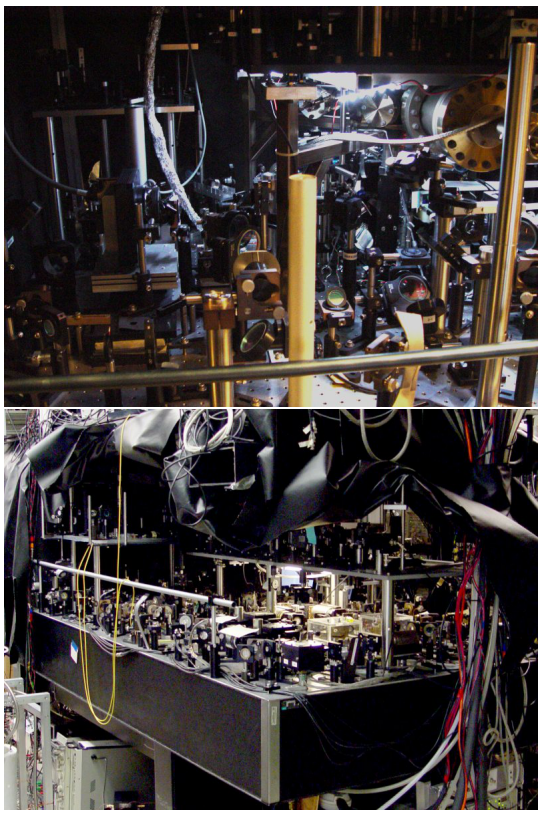

"It doesn't matter how beautiful your theory is, it doesn't matter how smart you are. If it doesn't agree with experiment, it's wrong."

-Richard Feynman

It is the privilege of experimentalists to query Nature with progressively refined and conglomerated theories, which often require increasingly elaborate experimental apparatuses. Indeed, the modern tabletop cold atom experiment can be an intricate and dauntingly vast amalgam of optics, electronics, vacuums, and graduate students. Each of these elements is both complicated and necessary, and each must work in concert to yield meaningful results. This chapter overviews the apparatus used to perform the experiments on rubidium as well as the methods employed for preparation and detection of the atomic ensembles. Exhaustive detail on the construction of the vacuum, magnetic, and laser systems can be found in [73–76]; this chapter will serve primarily as an overview.

3.1 Vacuum System

Due to the immense difference in temperature scales between the laboratory environment and the ensembles (typically greater than six orders of magnitude), cold atom experiments require absolute thermodynamic separation between the two. This is accomplished using a steel and glass vacuum chamber, a photograph of which is shown in Figure 3.1.

The vacuum chamber operates in the double MOT configuration [77]. The motivation for this design is to maintain a low background pressure in the science chamber (where the experiments are performed) without sacrificing the ability to accumulate rubidium atoms quickly. These goals seem diametrically opposed because, while the background gas is the source of ru-

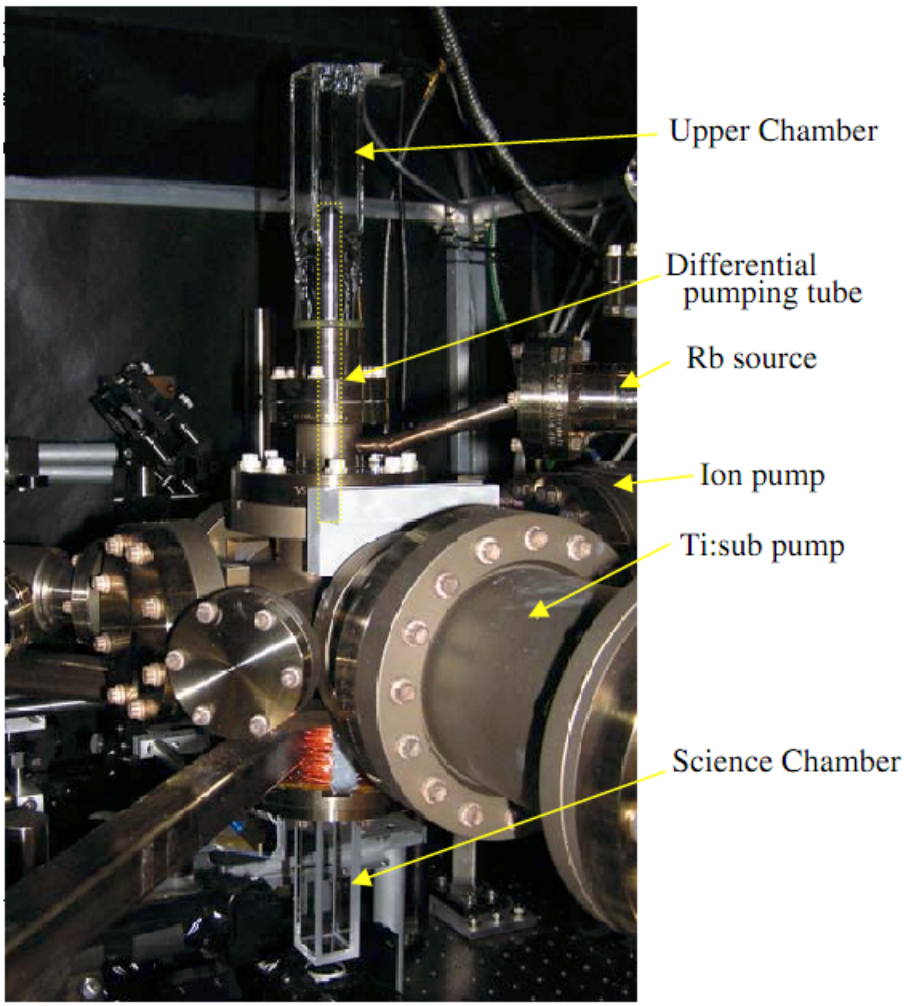

Figure 3.1: The vacuum chamber. Photo courtesy of Todd Meyrath [74].

bidium atoms for the experiment, collision with background gas atoms result in losses once the experiment has begun. An elegant solution to this problem is the use of two chambers, operated at different pressures and interconnected by a differential pumping tube that maintains the pressure gradient. Atoms are accumulated initially in the high-pressure chamber and then transferred through the differential pumping tube to the low-pressure chamber where the experiment occurs.

3.1.1 Upper Chamber

The upper chamber is a $4'' \times 1\,1/4'' \times 1\,1/4''$ rectangular Pyrex cell which is attached via a graded glass-to-metal seal to a $2\,3/4''$ conflat steel flange. A passageway for atoms to the lower chamber (consisting of the science chamber and pumping region) is provided by a $6\,3/4''$ type-304 stainless steel tube with a $\sim 1/8''$ tapered hole through the center. The tube conductance is approximately 0.05 L/s, allowing for a pressure differential of greater than three orders of magnitude. A schematic of the chamber is shown in Figure 3.2.

Roughly 200 mg of 3N5 purity solid rubidium is located in a reservoir attached to this chamber, leading to a background gas pressure of approximately 10^{-7} torr [78], the room temperature vapor pressure of rubidium. Only 28% of this is the desired isotope (^{87}Rb), but the isotopic shift makes ^{85}Rb transparent to the near-resonant lasers, and so it can be effectively ignored.

A MOT is created in this chamber, capturing atoms from the low-velocity tail of the Maxwell-Boltzmann thermal distribution. The MOT com-

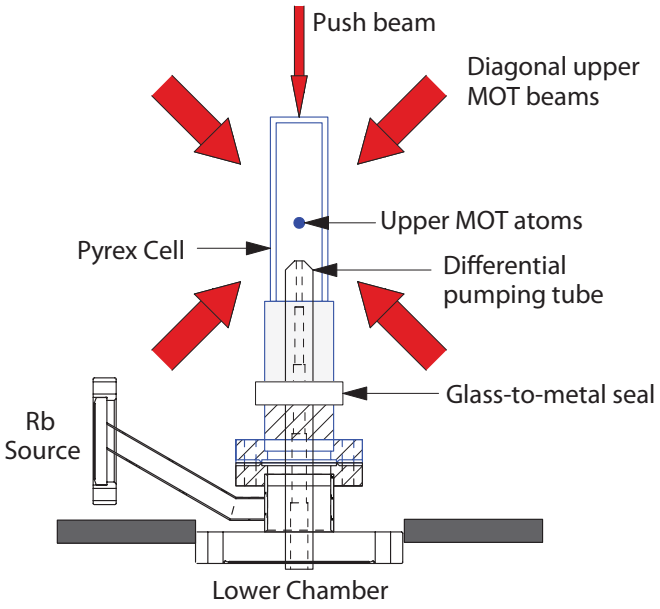

Figure 3.2: Schematic of the upper vacuum chamber, courtesy of Todd Meyrath [74].

prises three pairs of counter-propagating beams (one pair not shown in Figure 3.2) as well as a pair of anti-Helmholtz electromagnetic coils (also not shown). Cold atoms are accumulated in the center of the chamber, and, utilizing the scattering force of Equation 2.5, they are funneled downward through the differential pumping tube to the lower chamber with a resonant 'push beam.'

3.1.2 Lower Chamber

There are two regions of the lower chamber. The pumping region consists of two vacuum pumps which maintain a pressure below 10^{-10} torr in the entire lower chamber. The second region is the science chamber, where atoms are recaptured out of the push beam and experiments are performed.

3.1.2.1 Pumping Region

The heart of the pumping region is a modified six-way steel cross with $4\,1/2''$ and $2\,3/4''$ CF flanges. Two pumps are attached to this cross. The primary pump, which runs continuously, is an ion pump (Varian 919-0103) with nominal pumping speed of 75 L/s. An auxiliary titanium sublimation (Ti:sub) pump is also attached. The Ti:sub has a pumping speed around 300 L/s and is fired on occasion.

In addition to the two pumps, a nude Bayard-Alpert ion gauge is attached to the pumping region. The hot-cathode gauge has limited usefulness at pressures below 10^{-10} torr, and thus it is rarely operated. A more sensitive and valuable measure of the background pressure is given by the lifetime of atoms in the magnetic trap. The losses in the trap are dominated by collisions with background gas atoms, and so shorter lifetimes indicate higher pressures. The lifetime for this apparatus is typically around 20 s, which, though not ideal, is adequate for the cooling experiments.

The remainder of the flanges are sealed with flats and an all-metal valve used for attaching the chamber to a roughing pump station during the initial evacuation of the chamber.

3.1.2.2 Science Chamber

The construction and attachment of the science chamber was a remarkable feat of engineering, described in detail in the references given above. A photograph of the chamber is shown in Figure 3.3. It is a rectangular glass

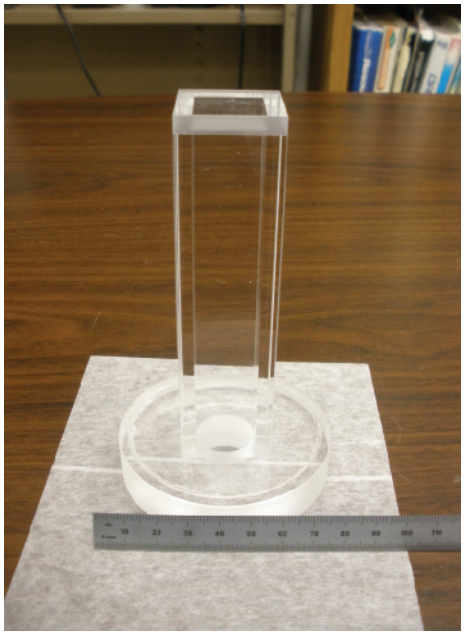

Figure 3.3: The science chamber before attachment to the pumping region.

cell with outer dimensions 30 mm × 30 mm × 115 mm attached to a cylindrical disc. The type of glass is Spectrosil (Heraeus Quarzglas GmbH), a proprietary UV-grade synthetic fused silica. The walls are 5 mm thick and were optically contacted and fused by Hellma Cells, Inc. A vacuum seal was made between the cylindrical piece and the steel chamber with a Helicoflex seal (Garlock Helicoflex H-307330 REV NC).

3.2 Magnetic System

Magnetic fields in the experiment are provided by current-flowing coils, and they serve two purposes. The first is to create quadrupole fields for the MOTs and magnetic trap. The second is to provide offset fields that both

counter the earth's magnetic field and shift the center of the quadrupole fields.

3.2.1 Anti-Helmholtz Coils

The Anti-Helmholtz configuration is one of the simplest and most ubiquitous coil configurations, and it can be used to produce magnetic fields for both MOTs and pure magnetic traps. It comprises two concentric circular coils separated by a distance equal to their radius, with current flowing through the coils in opposite directions. This creates a quadrupole field near the midpoint of the coils.

To see this, consider a single circular loop carrying electric current I. In cylindrical coordinates, with the origin at the center of the loop, the resulting magnetic field may be written [79]

$$B_z = \frac{\mu I}{2\pi} \frac{1}{\sqrt{(R+\rho)^2 + z^2}} \left[K(\xi^2) + \frac{R^2 - \rho^2 - z^2}{(R-\rho)^2 + z^2} E(\xi^2) \right] \tag{3.1a}$$

$$B_\rho = \frac{\mu I}{2\pi\rho} \frac{z}{\sqrt{(R+\rho)^2 + z^2}} \left[-K(\xi^2) + \frac{R^2 + \rho^2 - z^2}{(R-\rho)^2 + z^2} E(\xi^2) \right], \tag{3.1b}$$

where μ is the permeability, R is the loop radius, $K(\xi^2)$ and $E(\xi^2)$ are the complete elliptic integrals of the first and second kind, respectively, and the argument $\xi^2 = (4R\rho)/[(R+\rho)^2 + z^2]$.

With the addition of a second loop, concentric with the first but centered at $z = R$ and carrying current $-I$, the resulting is shown in Figure 3.4. At the midpoint of the coils, there is a local field minimum where atoms in a low-field seeking state may be trapped. In this experiment, atoms are confined

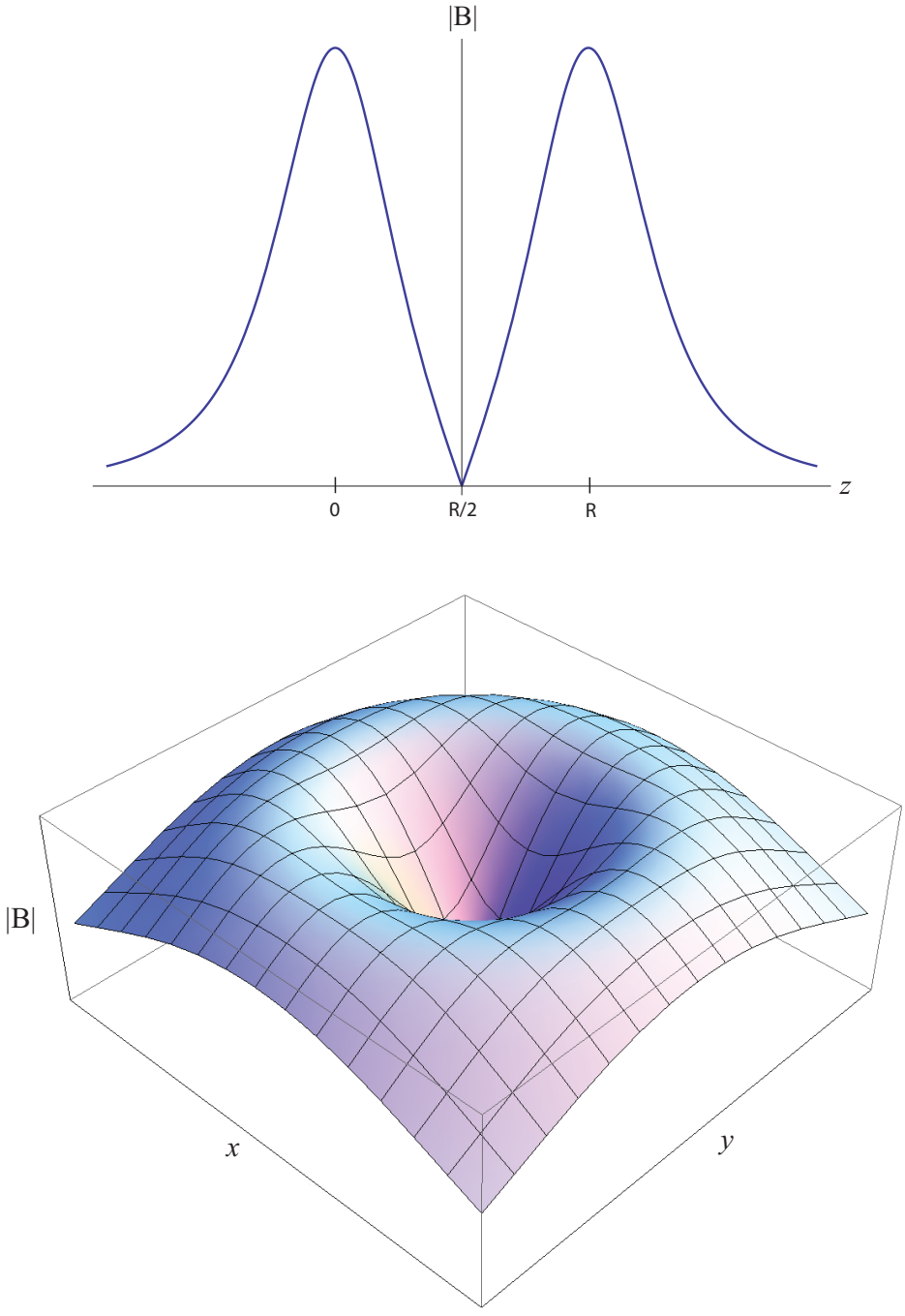

Figure 3.4: Axial and transverse field magnitude for anti-Helmholtz pair.

close enough to the center that the field gradients may be approximated as constant. The first terms in the Taylor expansions of the field magnitudes are

$$B_z = 2B'z \tag{3.2a}$$

$$B_\rho = B'\rho \tag{3.2b}$$

where the field gradient B' is given by

$$B' = \frac{3}{2}\mu I \frac{(d/2)R^2}{\left[(d/2)^2 + R^2\right]^{5/2}}. \tag{3.3}$$

3.2.1.1 Upper MOT Coils

A pair of circular coils, alluded to in Section 3.1.1, sandwich the glass cell of the upper vacuum chamber. The coils have a radius of 4 cm and are spaced by 6 cm. Around 2.5 A flow through 91 windings of 20 gauge wire, producing a nearly anti-Helmholtz quadrupole field for the upper MOT with a gradient of about 15 G/cm. The current in each coil is independently regulated by home-built current controllers [74], allowing the location of the field minimum (MOT center) to be adjusted. The coils are mounted to water-cooled copper blocks for heat dissipation.

3.2.1.2 Magnetic Trap Coils

Another pair of circular coils is located around the science chamber. These multipurpose coils create a weak-gradient field for the lower MOT when operated at low current as well as a strong-gradient field for the quadrupole

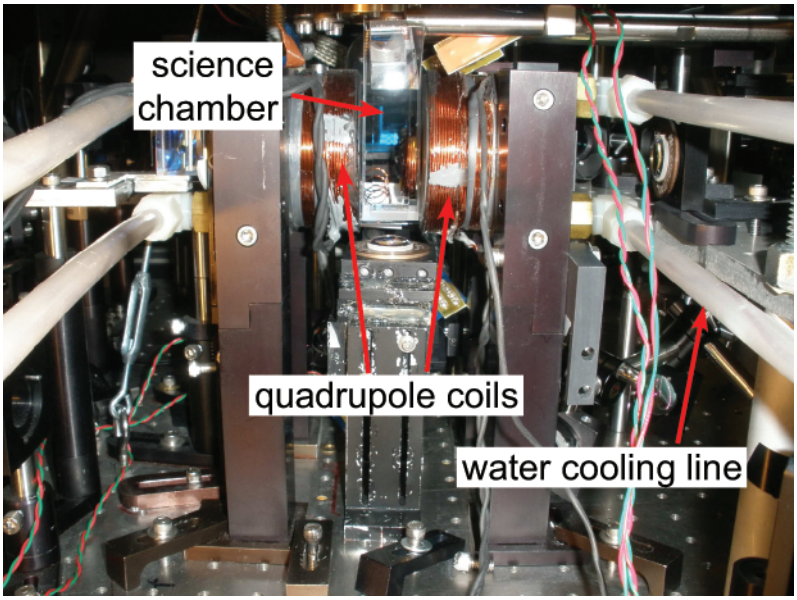

Figure 3.5: Photograph of the science chamber and quadrupole magnetic trap coils.

magnetic trap when operated at high current. They are pictured in Figure 3.5.

Each coil consists of 176 turns of 14 gauge magnetic wire in three layers, with an inner diameter of 34 mm, an outer diameter of 69 mm, and a width of 42 mm. From center to center, the coils are separated by 75 mm. The wire is encased by a PVC enclosure, and chilled water continuously flows through the enclosures to dissipate resistive heat. Figure 3.6 is a horizontal cross-section of the geometry and location of the magnetic trap coils.

The calculated field gradients near the midpoint, which agree well with the measured values, are $B_z = 9.7$ G/(cm A) and $B_\rho = 4.8$ (G/cm A) where z is the axial coordinate and $\rho = \sqrt{x^2 + y^2}$ is the radial coordinate.

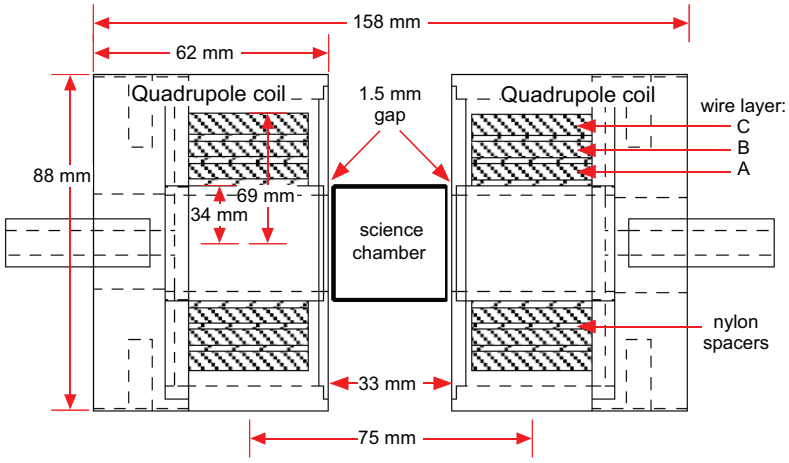

Figure 3.6: Schematic of the magnetic trap quadrupole coils.

Current flows in series through the coils and is generated by three power supplies (Lambda GEN80-19) wired in parallel. The current is regulated with seven power op-amps (OPA549) controlled by a home-built proportional-integral-derivative (PID) control circuit.

3.2.2 Auxiliary Coils

In addition to the two pairs of anti-Helmholtz coils, several more coils are positioned around the science chamber, serving various functions.

First, a Helmholtz pair is aligned on axis with the quadrupole coils. These coils each consist of 30 turns of 16 gauge wire, resulting in a near-uniform field at the trap center of about 2.6 G/A. The purpose of these coils is both to shift the center of the MOT/magnetic trap and to provide the reference field during optical pumping (Section 3.6).

Another auxiliary coil is located just above the science chamber and

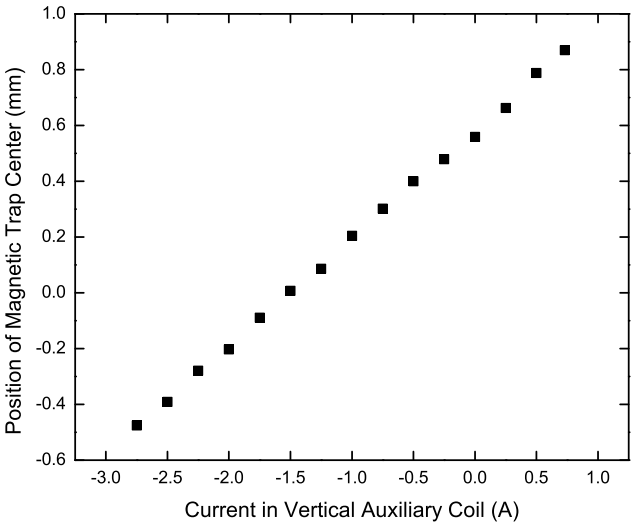

Figure 3.7: Adding a uniform field to the quadrupole field shifts its minimum. Here the center of a magnetically trapped ensemble is plotted against the current flowing through the vertical auxiliary coil.

oriented vertically. The coil consists of 150 turns of 20 gauge wire and produces a field near the trap center of roughly 1 G/A.

Naively, one might expect that superimposing a uniform field on a quadrupole field would do nothing but increase the magnitude of the field everywhere. However, the quadrupole magnetic field is vectorial and points in opposite directions on either side of its minimum. Therefore adding a uniform field *translates* the minimum (zero) in space rather than simply increasing it. This effect can be seen clearly in Figure 3.7, where the observed center of the magnetic trap shifts in proportion to the current through the vertical auxiliary coil.

3.3 Laser System

An intricate system of lasers and optics is used to manipulate and probe the atomic ensembles. The lasers can be grouped into two classes: lasers operating near the ^{87}Rb D_2 transition at wavelength $\lambda \approx 780\,\text{nm}$, and lasers far detuned from this wavelength.

3.3.1 Near-Resonance Lasers

A diagram of the near-resonance frequencies used in the experiment is shown in Figure 3.8. A total of six different frequencies are used, though not all simultaneously. All frequencies are resonant or located within 50 MHz of a D_2 ($5\,^2S_{1/2} \rightarrow 5\,^2P_{3/2}$) transition.

The fundamental light for the experiment is generated by two external-cavity diode lasers (ECDLs) in the Littrow configuration [80]: the MOT master laser and the repump laser. The frequency of each is locked to individual rubidium lines using saturated absorption spectroscopy methods. To generate adequate optical power for the experiment, the light from the MOT master laser is amplified by seeding it into three injection-locked 'slave' lasers. The frequencies of all five diode lasers are shifted using acousto-optic modulators (AOMs), many of which serve additionally as fast shutters. Because the experiment is extremely sensitive to stray light and the AOMs do not completely extinguish the diffracted orders, slower mechanical shutters are located at various points along the beam paths to provide full occlusion.

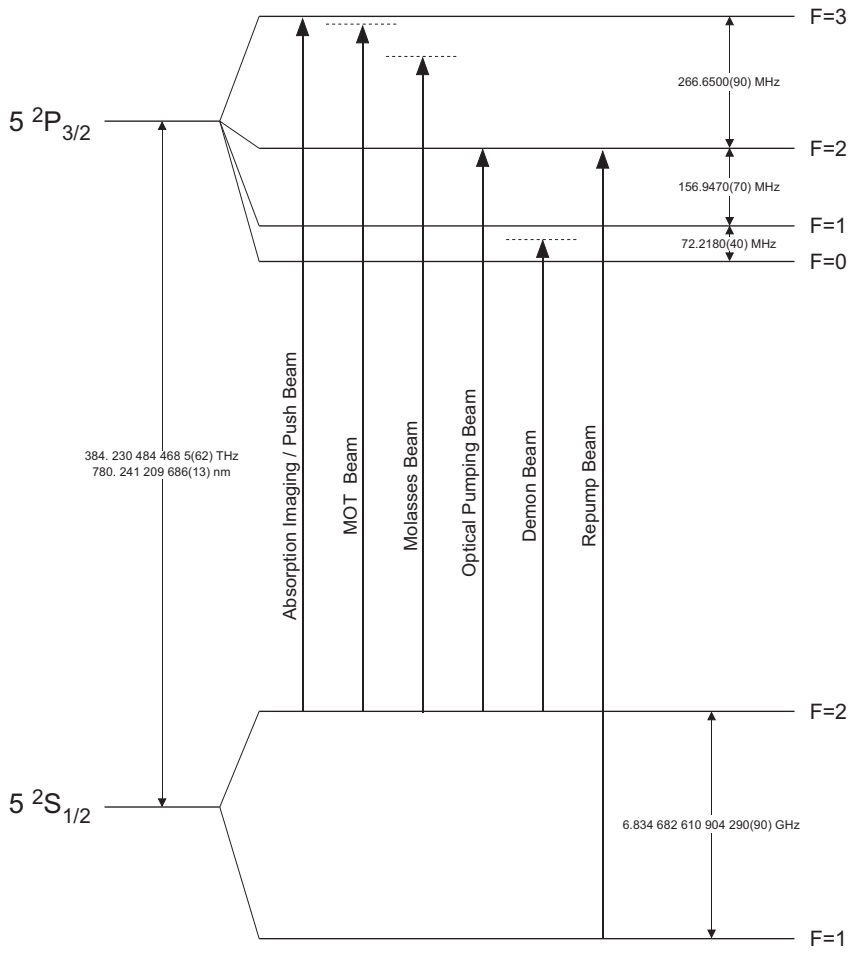

Figure 3.8: Near-resonance laser frequencies used in the experiment.

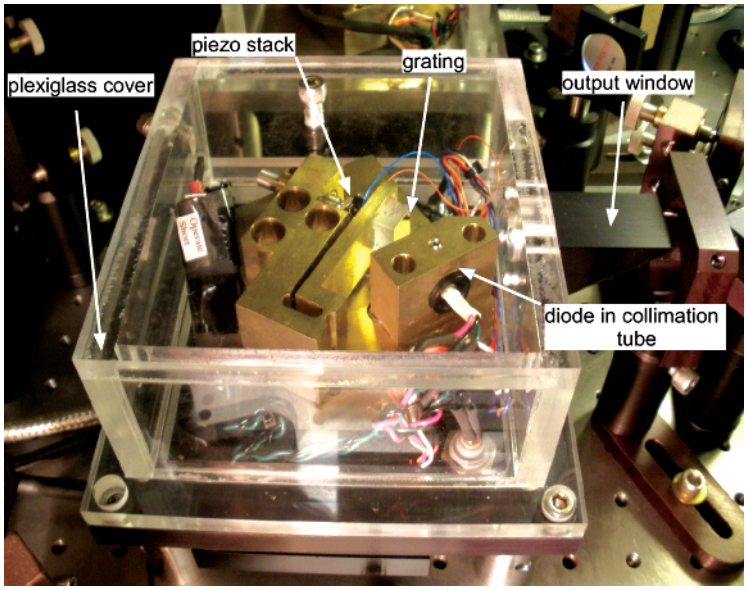

Figure 3.9: The MOT master laser.

3.3.1.1 MOT Master Laser

The MOT master laser, pictured in Figure 3.9, is a robust Littrow-configured ECDL designed and built originally for a prior experiment [81]. The heart of the laser is an edge-emitting diode (Intelite MLD-780-100S5P) with nominal wavelength of 780 nm and output power of 100 mW at injection current of 120 mA. The diode is mounted in a tube (Thorlabs LT230P-B) which houses a broadband anti-reflection (AR) coated aspheric lens ($f = 4.5\,\mathrm{mm}$). The exiting light is collimated and directed at a gold-coated, blazed diffraction grating with 1200 grooves/mm. This grating serves as the laser output coupler as well as frequency selector. The zeroth-order specular reflection is used as the output beam, while the first-order diffracted beam is retroreflected into the diode, forming the external laser cavity. By adjusting the grating angle

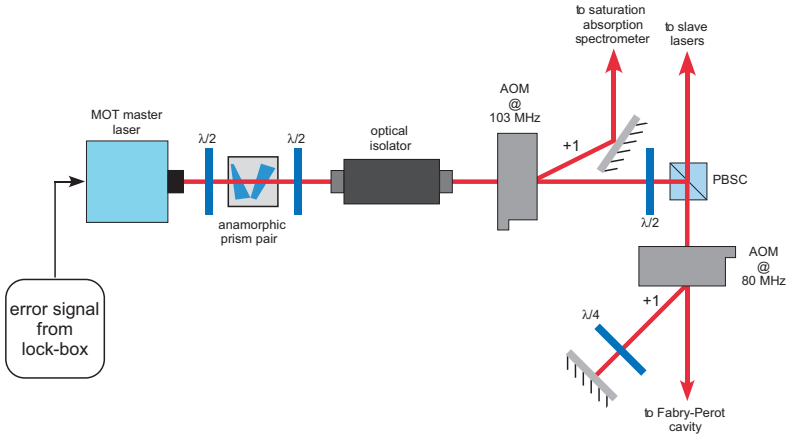

Figure 3.10: Distribution of the MOT master laser output.

with a piezo stack, the output wavelength can be finely tuned. The linewidth of the laser has an upper bound of 1.5 MHz, as measured with a Fabry-Perot cavity.

For maximum stability, all parts are mounted on a bronze baseplate which is actively temperature stabilized with a thermo-electric cooler (TEC) and PID circuit. A plexiglass cover thermally isolates the laser and rejects air currents and acoustic vibrations.

The asymmetry in the spatial mode of the laser is removed with an anamorphic prism pair, and the beam is sent through an optical isolator (Conoptics 712B). The isolator, which utilizes the Faraday effect, prevent back-reflections from reaching the master diode and causing lasing instabilities. Subsequent to the isolator, the beam is distributed into three paths, as shown in Figure 3.10.

Most of the laser power passes straight through a 103 MHz AOM. This zeroth-order diffracted beam reflects off a polarizing beamsplitter cube (PBSC) and double-passes an 80 MHz AOM with a 40 MHz bandwidth. Because the first-order diffracted beam double-passes a quarter waveplate ($\lambda/4$), its polarization rotates by $\pi/2$, and it travels straight though the PBSC on second incidence. It is then distributed to the slave lasers for injection locking (see Section 3.3.1.3). As a result of the double-pass, the injection beam, and hence the slave lasers, are tunable between 80 and 160 MHz red of the $F = 2 \rightarrow F' = 3$ transition. The slave lasers are each followed by their own 80 MHz AOMs, allowing for final frequencies between resonance and 80 MHz red of the $F = 2 \rightarrow F' = 3$ transition.

A small amount of light is undiffracted by the 80 MHz AOM and is coupled into a Fabry-Perot cavity. This cavity serves as a useful diagnostic for ensuring single-mode operation of the MOT master laser.

Finally, a few milliwatts is diffracted into the first-order of the 103 MHz AOM. This light is sent to a saturated absorption spectrometer which actively stabilizes the fundamental laser frequency to a rubidium transition. A layout of the setup is depicted in Figure 3.11.

A thorough review of saturation absorption spectroscopy may be found in [82]. There are many ways to produce a dispersive error signal for stabilizing a laser to an atomic transition. The error signal for the MOT master laser is produced in a fairly straightforward fashion.

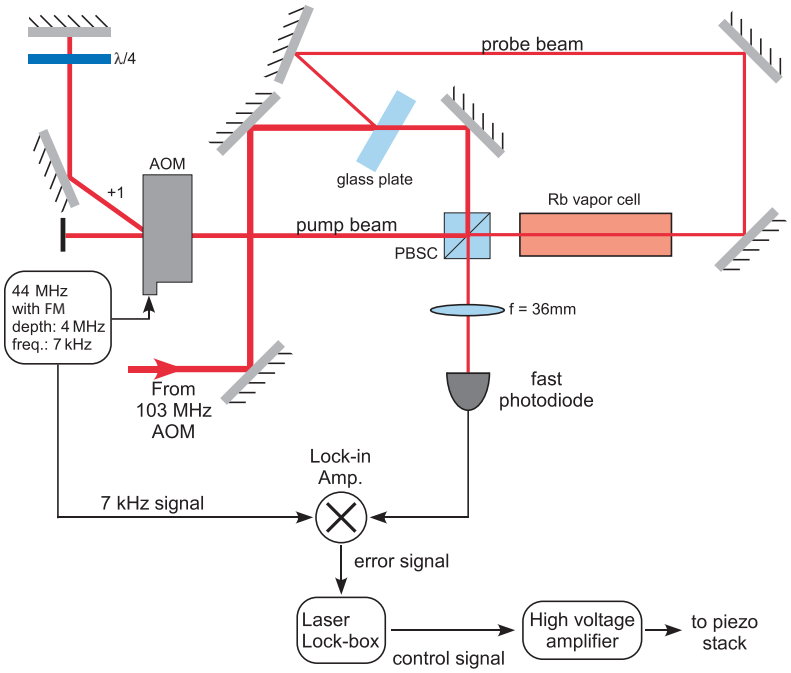

Figure 3.11: The saturated absorption spectrometer and locking setup for the MOT master laser.

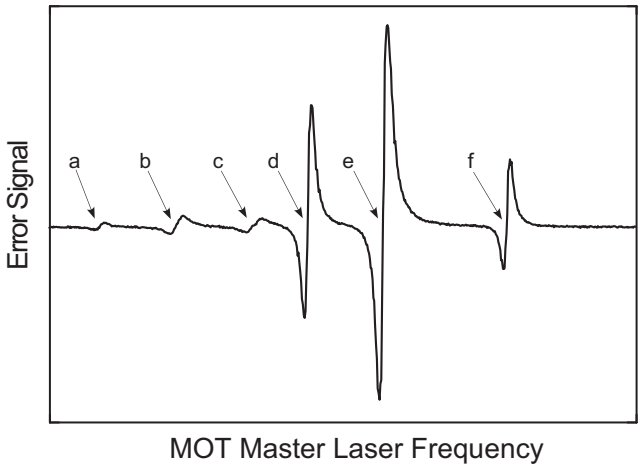

Figure 3.12: Error signal for the MOT master laser. The labeled real and crossover transitions are (a) $F = 2 \rightarrow F' = 1$ (b) $F = 2 \rightarrow F' = 1/2$ (c) $F = 2 \rightarrow F' = 2$ (d) $F = 2 \rightarrow F' = 1/3$ (e) $F = 2 \rightarrow F' = 2/3$ (f) $F = 2 \rightarrow F' = 3$.

The beam is split into a strong pump beam and a weak probe beam with an uncoated glass plate. The pump beam double-passes an AOM that is driven by a frequency modulated (FM) 44 MHz signal with modulation depth 4 MHz and frequency 7 kHz. It then passes through a room-temperature rubidium vapor cell. The probe beam counter-propagates with the pump beam in the vapor cell and is focused onto a photodiode. The resulting signal is mixed with the FM frequency by a commercial lock-in amplifier (SRS SR510). When the MOT master laser frequency is scanned across the $F = 2 \rightarrow F' = 1, 2, 3$ transitions, a dispersive error signal is produced by the lock-in amplifier (Figure 3.12).

Because it is the most prominent, the $F = 2 \rightarrow F' = 2/3$ crossover

transition is used for locking. The error signal is fed into a PID circuit, the output of which is amplified (Trek 601B-2) and input to the piezo stack which controls the diffraction grating angle. This closes the feedback loop and locks the frequency of the MOT master laser 280 MHz red of the $F = 2 \rightarrow F' = 3$ transition.

3.3.1.2 Repump Laser

During the experiment, atoms will decay on occasion to the $|F = 1\rangle$ ground state. This can be problematic because the MOT master laser and its slaves are tuned to transitions from the $|F = 2\rangle$ ground state, meaning these atoms are in a dark state which scatters no photons. To remedy this, a repump laser tuned to the $F = 1 \rightarrow F' = 2$ transition is introduced. This laser is used during the MOT, molasses, optical pumping, and detection stages of the experiment to cycle atoms from $|F = 1\rangle \rightarrow |F = 2\rangle$.

The repump laser is constructed identically to the MOT master laser. The distribution of its output power is shown in Figure 3.13. Because the output power of the repump laser is sufficient for the experiment (~ 30 mW), the laser is directed straight to the upper and lower chambers rather than to slave lasers.

A small amount of power is picked off after the optical isolator with a PBSC. This light goes to another saturated absorption spectrometer, depicted in Figure 3.14. The setup is slightly different from that of the MOT master laser (Figure 3.11). Here, two weak probe beams are created by a glass plate

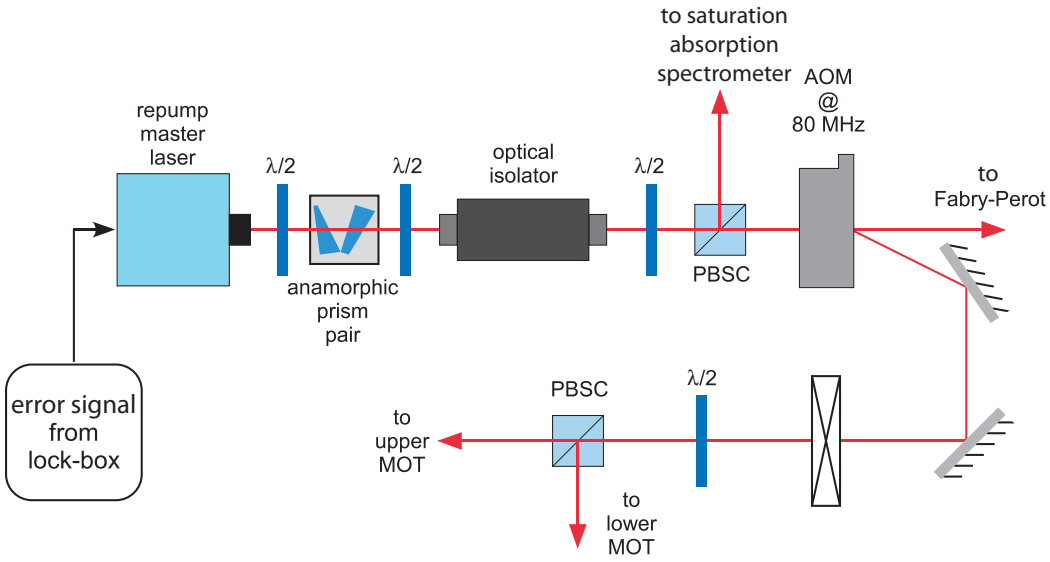

Figure 3.13: Distribution of the repump laser output.

beamsplitter, and the strong pump beam overlaps only one of them in the rubidium vapor cell. The probe beams are then subtracted by a differential photodetector. The purpose of this configuration is to subtract the doppler-broadened background absorption from the spectroscopy signal.

Another difference with this setup is that the frequency modulation is applied to the laser not by an FM AOM, but rather by directly dithering the piezo stack of the laser. This introduces some frequency noise to the laser, but it has a negligible operational effect.

Figure 3.15 is the dispersive error signal produced by the repump saturated absorption spectrometer. The laser is locked to the $F = 1 \rightarrow F' = 1/2$ transition which is 78.5 MHz red of the desired $F = 1 \rightarrow F' = 2$ transition. As shown in Figure 3.13, the frequency is upshifted by an 80 MHz AOM, putting

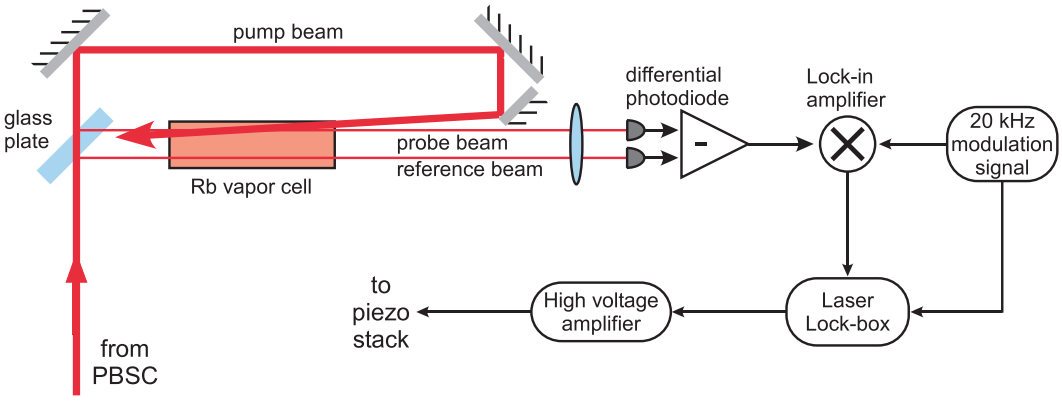

Figure 3.14: The saturated absorption spectrometer and locking setup for the repump laser.

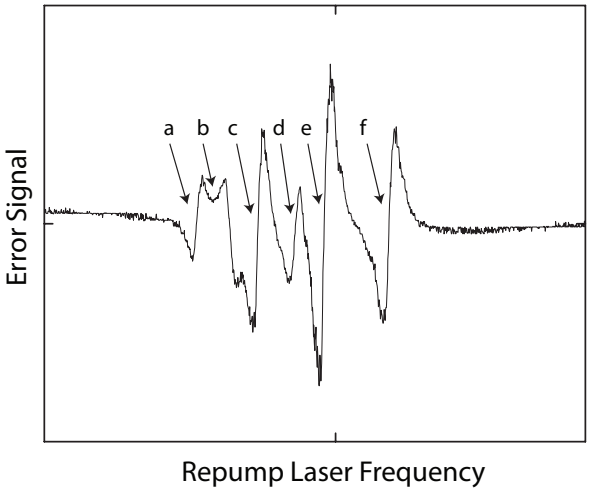

Figure 3.15: Error signal for the repump laser. The real and crossover transitions are labeled (a) $F = 1 \rightarrow F' = 0$ (b) $F = 1 \rightarrow F' = 0/1$ (c) $F = 1 \rightarrow F' = 1$ (d) $F = 1 \rightarrow F' = 0/2$ (e) $F = 1 \rightarrow F' = 1/2$ (f) $F = 1 \rightarrow F' = 2$.

it within 1.5 MHz of resonance. Because the linewidth of this transition is about 6 MHz, the offset can be ignored.

3.3.1.3 Upper MOT Horizontal Slave Laser

The upper MOT horizontal slave laser is the first of three injection-locked lasers which amplify the MOT master laser. A photograph of the construction is shown in Figure 3.16. The slave lasers are built around an inexpensive diode (Sharp GH0781JA2C) with a nominal wavelength of 784 nm and power of 120 mW at 140 mA injection current. The diode is housed in a collimation tube (Thorlabs LT230P-B) which is mounted in a bronze block. This block is temperature-controlled to bring the diode's free-running wavelength closer to the rubidium resonance. The laser is enclosed by an aluminum housing, and the light escapes through a glass Brewster window.

An injection-locked diode laser can be considered as a regenerative amplifier [83]. The goal is to seed the gain medium with enough external laser light such that the free-running laser oscillation dies out and the gain is saturated entirely by the injected seed light. In practice, $\sim$ 2 mW is enough injection power for this to occur. Figure 3.17 shows the injection technique. A portion of the MOT master injection beam is picked off using a half waveplate ($\lambda/2$) and a PBSC. This beam is aligned into the output rejection port of an optical isolator (Conoptics 712B), so that it is collinear with and the same polarization as the free-running slave laser output. With careful alignment, the slave laser produces $\sim$ 60 mW of power with the spectral characteristics

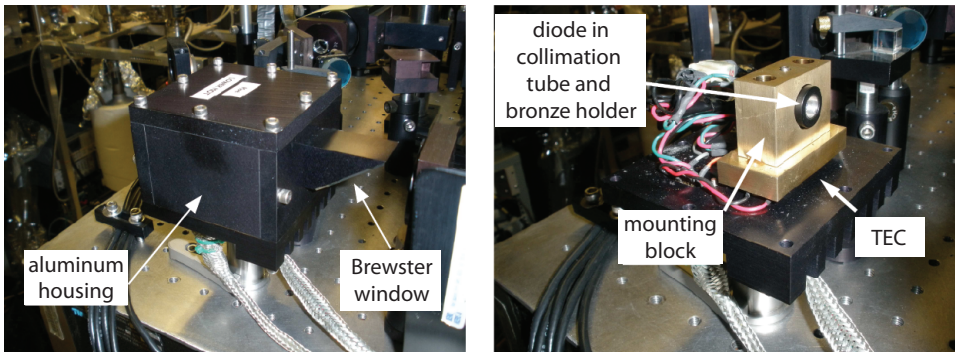

Figure 3.16: Photograph of a slave laser, with and without the aluminum housing.

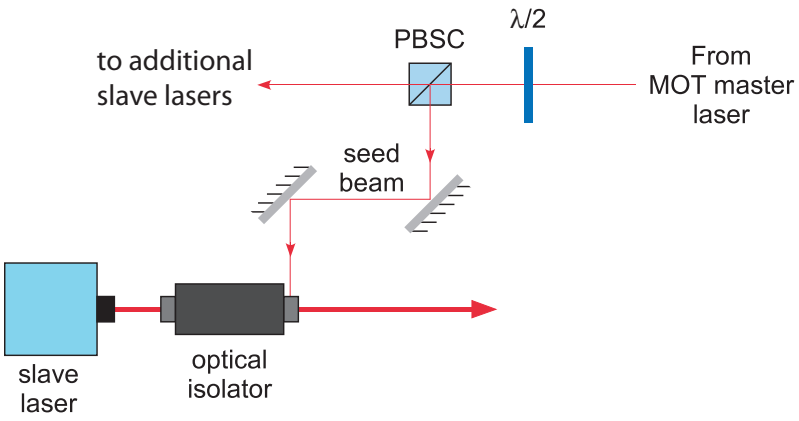

Figure 3.17: Method used for injection-locking the slave lasers.

of the seed laser.

As should be apparent from its name, the upper MOT horizontal slave laser's primary function is to provide light for the horizontal beams of the upper MOT. It provides light for several other purposes as well. Figure 3.18 shows the distribution of the laser beam. After the optical isolator, the beam passes through an 80 MHz AOM. The first-order diffracted beam goes to the

upper MOT. Part of this beam is picked off by a 424 MHz AOM. The minus-first-order beam is near resonance with the $F = 2 \rightarrow F' = 1$ transition, and it serves as the demon beam (see Section 3.4.3).

Part of the original beam passes through the first 80 MHz AOM undiffracted. A small portion is picked off by a beamsplitter and sent to a Fabry-Perot cavity used to check for proper injection locking. The remainder is upshifted by an 80 MHz AOM to become the push beam, or it double-passes a tunable AOM centered at 56 MHz to become the vertical absorptive imaging beam. The role of the latter beam is described in Section 3.4.3.

3.3.1.4 Upper MOT Diagonal Slave Laser

The upper MOT diagonal laser, in addition to providing light for the diagonal beams of the upper MOT, supplies laser power for the optical pumping and horizontal absorptive imaging beams. Figure 3.19 shows the beam distribution. Following the optical isolator, the first-order diffracted beam from an 80 MHz AOM goes to the upper MOT.

The zeroth-order beam is then directed toward a series a double-pass AOMs, arranged such that the retroreflected beams from both AOMs are collinear and follow the same path to the vacuum chamber. The minus-first-order diffracted beam double-passed through the 80 MHz AOM serves as the optical pumping beam (see Section 3.6 for details). The frequency of this beam has been lowered by 160 MHz, making it resonant with the $F = 2 \rightarrow F' = 2$ optical pumping transition, assuming an appropriate injection beam detuning.

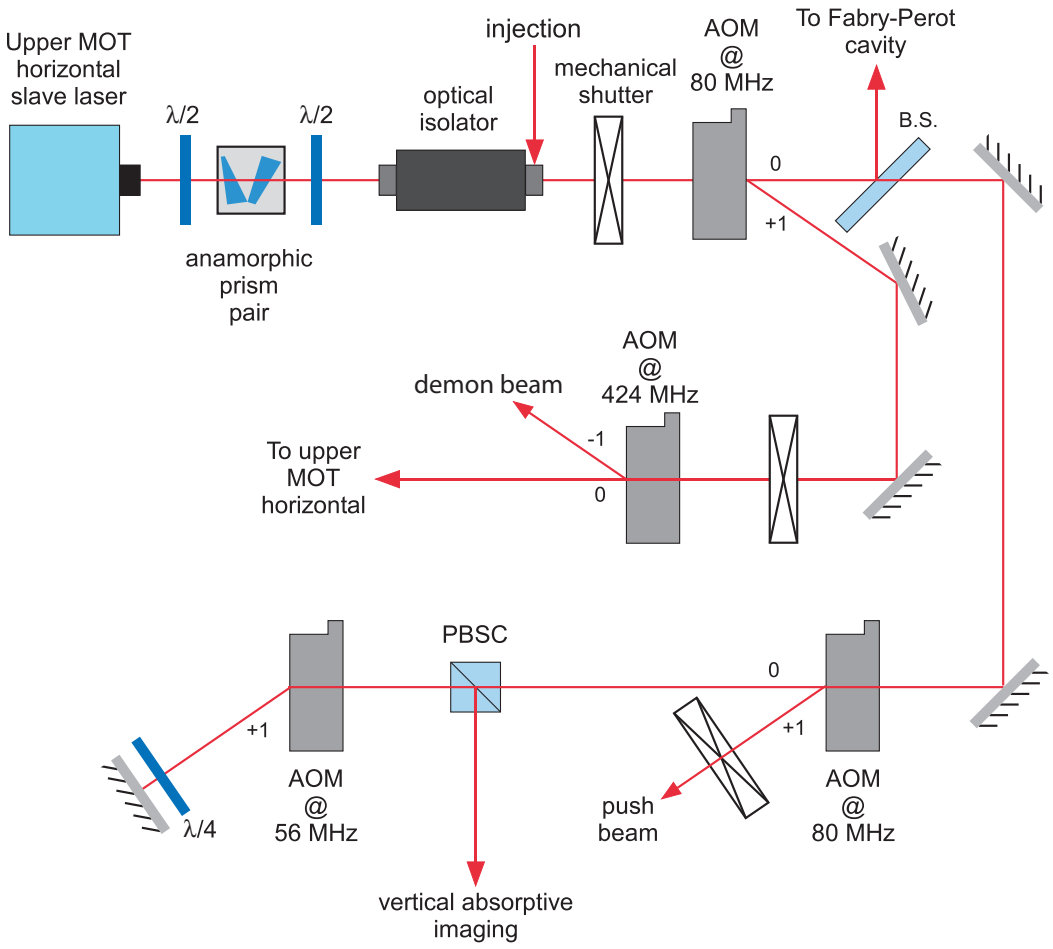

Figure 3.18: Distribution of the upper MOT horizontal slave laser.

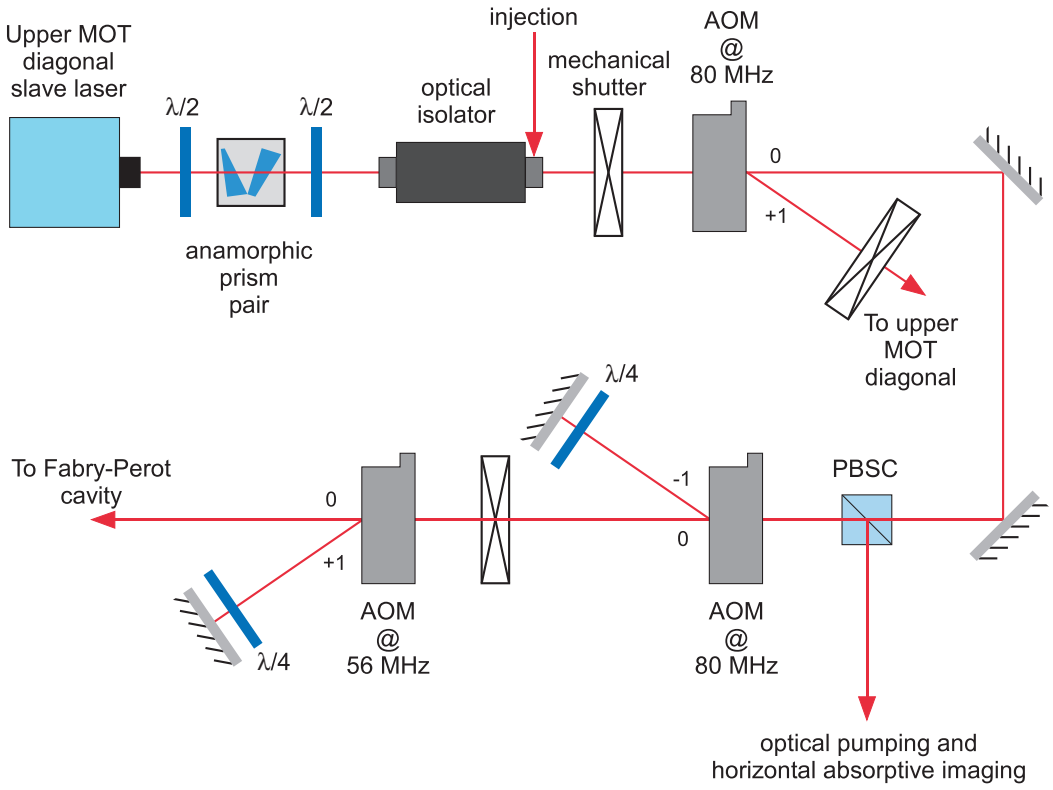

Figure 3.19: Distribution of the upper MOT diagonal slave laser.

The beam created by double-passing the tunable 56 MHz AOM serves as the horizontal absorptive imaging beam. More detail on this beam is given in Section 3.4.3.

Finally, the undiffracted beam from the 56 MHz AOM is sent to a Fabry-Perot cavity for diagnostics.

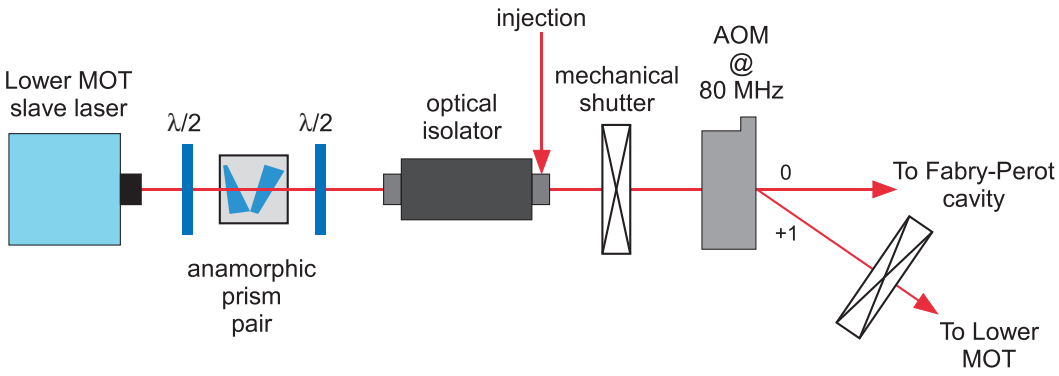

Figure 3.20: Distribution of the lower MOT slave laser.

3.3.1.5 Lower MOT Slave Laser

Nearly all of the power from the lower MOT slave laser is used for the lower MOT. A small portion is undiffracted by an 80 MHz AOM and is sent to the diagnostic Fabry-Perot cavity. The layout is shown in Figure 3.20.

3.3.2 Far-Detuned Laser

A laser detuned far from resonance ($\lambda = 532\,\text{nm}$) is used in the experiment to create an optical dipole trap. This laser is a frequency-doubled Nd:Vanadate (Coherent Verdi V10) which provides 10 W of power in the TEM_{00} spatial mode. It is also single-mode longintudinally with a linewidth less than 5 MHz.

Because its frequency is blue of the rubidium transition, the laser creates a repulsive potential for ground state atoms in accordance with Equation 2.21. Thus a trap may be created by surrounding atoms with laser fields on all sides (a "closed" trap) or allowing a force such as gravity to hold atoms on one

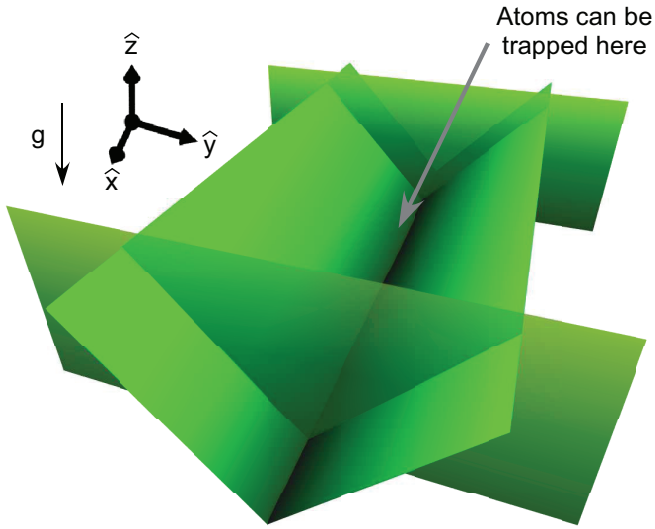

Figure 3.21: The optical trough.

side and surrounding it with laser fields on the others (an "open" trap). The optical trap used for the rubidium experiment discussed in this dissertation is an open trap, and, due to its shape, it is referred to as the *optical trough*.

As shown in Figure 3.21, the optical trough comprises four elliptical Gaussian laser beams which have been elongated in one dimension with cylindrical lenses. Two of these beams propagate along $\hat{\mathbf{x}}$ and cross to form a "V" shape. These V beams, along with gravity which is aligned along $\hat{\mathbf{z}}$, confine atoms in the $\hat{\mathbf{y}}$ and $\hat{\mathbf{z}}$ direction. Another pair of beams ("end caps"), whose elongated axes are parallel, propagate along $\hat{\mathbf{y}}$ and confine atoms in the $\hat{\mathbf{x}}$ direction. Each beam has a $1/e^2$ waist of $10\,\mu\text{m} \times 100\,\mu\text{m}$ and roughly 700 mW of optical power, resulting in a three-dimensional trap depth of $\sim 10\,\mu\text{K}$. A

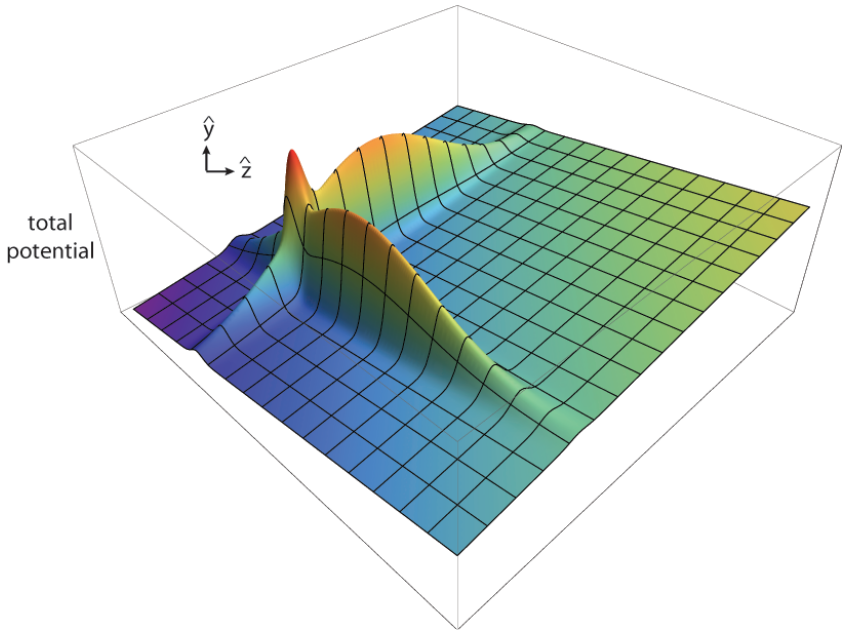

Figure 3.22: Potential of the gravito-optical trap in the $(\hat{\mathbf{y}}, \hat{\mathbf{z}})$ plane.

plot of the optical potential along with gravity in the $(\hat{\mathbf{y}}, \hat{\mathbf{z}})$ plane is shown in Figure 3.22.

A schematic of the beam layout for the far-detuned laser is shown in Figure 3.23. The beam is split into three paths (enumerated on the schematic) by a combination of half-waveplates and thin-film polarizing beamsplitters (PBS). Beams 1 and 2 constitute the V beams. Two cylindrical lenses, oriented at right angles to each other, make the beams astigmatic. The beams are then recombined with a PBSC and focused into the science chamber with a 63.5 mm lens.

The end caps are derived from Beam 3. These are created with an AOM which is driven at two distinct frequencies, creating two first-order diffracted

beams. The difference in the driving frequencies determines the difference in diffraction angle, which, in turn, yields the spacing between the beams at their focus. In practice, driving an AOM with multiple frequencies creates a large number of diffracted beams, both at harmonics of the driving frequencies as well as the difference frequency. The undesired diffracted orders are occluded by a one-dimensional spatial filter (essentially a pair of knife-edges) at the focus of a telescope which follows the AOM. Subsequent to this, a 300 mm cylindrical lens makes the pair astigmatic. The pair is then combined with a near-resonant beam path by a dichroic mirror (transparent to 780 nm) and focused into the science chamber with a 50 mm lens.

3.4 Imaging and Measurement

At the end of the experimental sequence, it is necessary to measure certain properties of the ensembles such as spatial distribution and atom number. This is accomplished with two distinct imaging techniques: absorption imaging and fluorescence imaging. Both techniques have advantages and disadvantages, but they complement each other well in the regime in which the experiment is operated. They are essentially two-dimensional techniques, and so two imaging systems, oriented along orthogonal axes, are employed to facilitate measurements in all three dimensions.

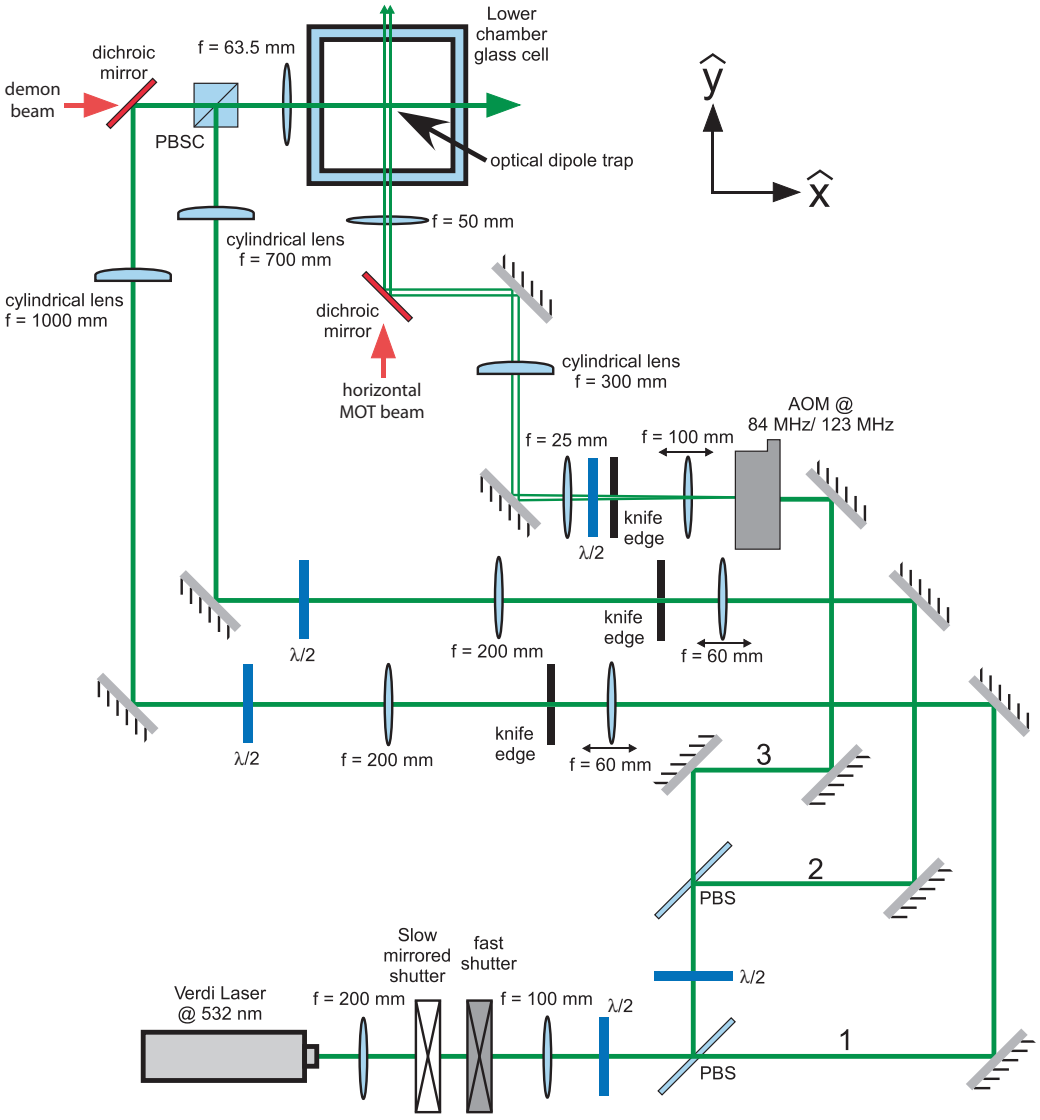

Figure 3.23: Distribution of the far-detuned laser beam.

3.4.1 Absorption Imaging

Absorption imaging is a technique which extracts information from the shadow cast by a cloud of atoms in the profile of a resonant or near-resonant probe beam. As the probe beam passes through the cloud, the atoms scatter photons out of the beam at the rate R given by Equation 2.2. The scattering cross-section may be written

$$\sigma = \frac{R\hbar\omega}{I} = \frac{\sigma_0}{1 + (I/I_s) + (2\delta/\Gamma)^2}, \tag{3.4}$$

where $\sigma_0 \equiv \hbar\omega\Gamma/2I_\mathrm{s}$ is the low-saturation resonant cross-section. The quantity σI represents the power each atoms scatters out of a probe beam of intensity I, and thus the attenuation of a probe beam propagating along z and passing through a cloud with atomic density $n(x, y, z)$ is given by Beer's law:

$$\frac{dI}{dz} = -\sigma n(x, y, z) I. \tag{3.5}$$

The solution to this differential equation is the transverse intensity profile of the probe beam:

$$I(x, y) = I_0(x, y) e^{-\sigma \int n(x,y,z) dz}. \tag{3.6}$$

Here the exponential factor on the right hand side is the shadow cast by the cloud of atoms. If the unattenuated intensity profile $I_0(x, y)$ is known (i.e. the profile with no atoms present), then the optical density is straightforward to calculate. It is given by

$$D_\mathrm{opt}(x, y) = -\ln\left(\frac{I(x, y)}{I_0(x, y)}\right) = \sigma \int n(x, y, z) dz. \tag{3.7}$$

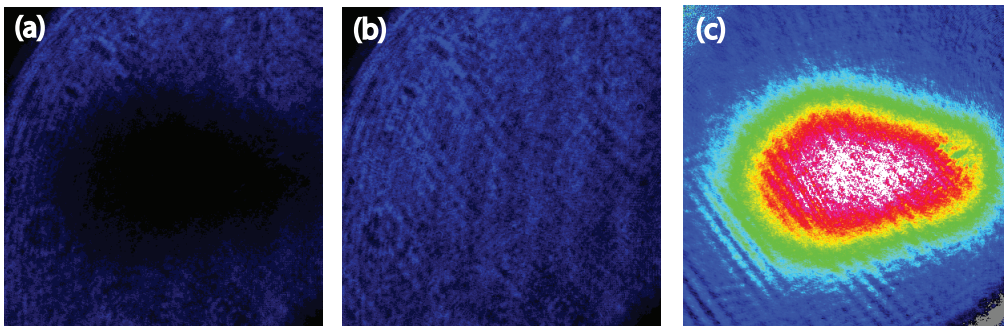

Figure 3.24: Absorption imaging method. (a) Probe beam displaying $I(x, y)$ (b) Unattenuated intensity profile $I_0(x, y)$ (c) Optical density D_{opt} calculated from (a) and (b). The total number of atoms here, given by the integration of (c) is $N = 1.7 \times 10^8$.

This quantity, which is proportional to the integrated column density of the cloud, can be used to calculate the total number N of atoms, given by

$$N = \iiint n(x, y, z)dxdydz = \frac{1}{\sigma} \iint D_{\text{opt}}(x, y)dxdy. \tag{3.8}$$

Figure 3.24 is an example of this sort of calculation for a cloud of atoms from a MOT.

While atom number and spatial distribution may be determined from a single image, accurate temperature measurements are made using a series of images. The time-of-flight method [84, 85] images a freely expanding cloud at different expansion times as the momentum distribution is converted into a spatial distribution. In the absence of collisions, the atoms follow ballistic trajectories upon release from the trap, and the spatial distribution measured after time t is a convolution of the initial density and momentum distributions. Assuming that the initial distributions are both Gaussian, the measured spatial

distribution is given by

$$n(x,t) = \frac{1}{(2\pi\sigma_t^2)^{3/2}} e^{-x^2/2\sigma_t^2}, \tag{3.9}$$

where σ_0 is the $1/\sqrt{e}$ width of initial density distribution and

$$\sigma_t^2 = \sigma_0^2 + \frac{\sigma_p^2}{m^2} t^2. \tag{3.10}$$

Here σ_p is the $1/\sqrt{e}$ width of the momentum distribution and is related to the temperature by $T = \sigma_p^2/mk_B$. Substituting for σ_p, Equation 3.10 can be rewritten:

$$\sigma_t^2 = \sigma_0^2 + \frac{k_B T}{m} t^2. \tag{3.11}$$

By imaging the cloud at multiple expansion times, the measured Gaussian widths may be fitted to the above equation to yield a value for the temperature.

It is important to note that Equation 3.11 describes a single dimension. For a system in thermal equilibrium, the temperatures in all degrees of freedom are equal, and hence the system may be described by a single value for the temperature. However, it is sometimes the case with experiments described herein that the system under consideration is not fully in equilibrium. In this situation, multiple temperature values are used to represent the momentum distributions in separate dimensions.

3.4.2 Fluorescence Imaging

In addition to absorption imaging, the experiment employs fluorescence imaging. Unlike absorption imaging, fluorescence imaging is sensitive to small

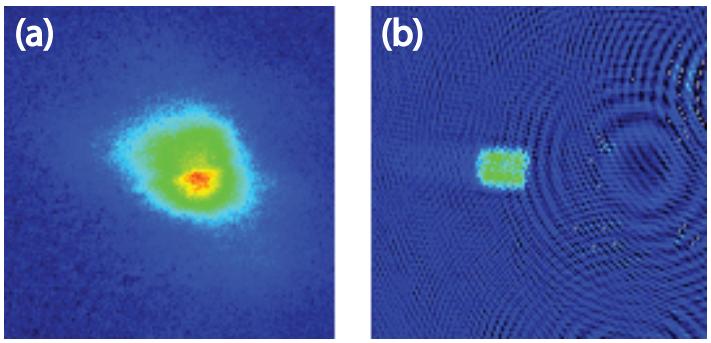

Figure 3.25: Comparison of fluorescence and absorption images. (a) The fluorescence image is large and has no distinct features. (b) The absorption image shows details of atoms confined in a hard-walled box.

numbers of atoms. In fact, the technique has been used to detect just a single atom [86]. However, the advantage of sensitivity to small atom numbers is accompanied by an inherent loss of spatial detail. Thus fluorescence imaging is useful for atom counting and not particularly for density or temperature measurements. A comparison of absorption and fluorescence images is shown in Figure 3.25.

Fluorescence imaging is very much the inverse of absorption imaging. Rather than image the shadow cast by atoms scattering photons, the scattered photons themselves are collected and imaged. Also, instead of using a single beam for excitation, the atoms are illuminated by six optical molasses beams. In this way, they are actively cooled as they fluoresce. The total atom number N is proportional to the total number of photons collected N_p and may be estimated by [60]

$$N = \frac{8\pi[1 + 6I/I_s + (2\delta/\Gamma)^2]}{6\Gamma(I/I_s)t_f\eta d\Omega} N_p, \tag{3.12}$$

where t_f is the fluorescence time, η is the fraction of collected photons which are actually registered by the detector, and $d\Omega$ is the solid angle of photon collection.

3.4.3 Horizontal and Vertical Imaging System

The horizontal probe beam is derived from the upper MOT diagonal laser as shown in Figure 3.19. It is typically operated on resonance with the $F = 2 \rightarrow F' = 3$ transition. The beam is combined with the path of one horizontal lower MOT beam using a PBSC. After passing through the chamber, it is picked off by another PBSC, relayed by a pair of 120 mm lenses, and imaged onto a charge-coupled device (CCD) camera (Apogee AP9e) with a 4x objective lens.

Horizontal fluorescence images can also be taken by triggering a motorized flipper mirror in front of the objective lens. A high solid angle collection lens [87] collects fluorescence in a direction perpendicular to the probe beam and directs it toward the flipper mirror.

The vertical probe beam is derived from the upper MOT horizontal laser, as shown in Figure 3.18. It is typically operated resonantly like its counterpart. The probe beam is combined with the push beam by a PBSC, and it is focused through the chamber with a 175 mm lens. The beam is collected with a 50 mm lens and is imaged onto a CCD camera (Apogee Alta U47+) with a net magnification 4.33x.

Because there are no vertical molasses beams, the vertical fluorescence

is imaged along the same path as the vertical probe beam.

3.5 Experimental Control and Data Acquisition

Execution of the experimental sequence requires precise timing of digital and analog outputs, as well as communication with external hardware such as frequency generators, lasers, and CCD cameras. These tasks are carried out by three networked desktop PCs running customizable software originally written by former group members [88].

The experiment is controlled by a PC which houses several PCI boards manufactured by National Instruments (NI): two digital input/output boards (PCI-6533) and three analog output boards (PCI-6733). These boards are operated as a digital output bus for a home-built hardware system capable of 80 digital outputs and 64 analog outputs with 625 kHz temporal resolution. The hardware is described in detail in [74]. A general purpose interface bus board (PCI-GPIB), also made by NI, allows the computer to communicate with a number of frequency generators and the Nd:Vanadate laser.

This PC runs the software *Control*, which was written by a former postdoctoral scholar Florian Schreck. *Control* is a powerful C++ program that writes a waveform to the NI cards, controlling the analog and digital outputs. It may be modified easily for new experimental routines.

A second PC performs data acquisition with the software *Vision* which was also written by Florian Schreck. *Vision* communicates with the CCD

cameras through a third PC, the sole purpose of which is to relay information between the cameras and *Vision*. After a measurement is performed, *Vision* processes the images and performs a number of analytical functions.

3.6 Preparation of the Ensemble

The starting point for single-photon cooling is a magnetically trapped ensemble. It is produced using routine methods. Atoms are first captured in the upper MOT from the room-temperature rubidium vapor at a rate of roughly 2×10^9 atoms/s. The push beam funnels these atoms to the lower MOT, which recaptures them. The lower MOT is typically operated for $1-2$ seconds with a field gradient $B' \approx 8$ G/cm and laser detuning 15 MHz red of the $F = 2 \rightarrow F' = 3$ cycling transition. Approximately 10^8 atoms are produced in the lower MOT at a temperature around 150 μK.

Following the loading of the lower MOT, the atoms undergo polarization gradient cooling [89]. The upper MOT, push beam, and magnetic fields are all turned off, and the lower MOT beams are detuned 50 MHz red of the cycling transition. The atoms are cooled to approximately $15-20\,\mu$K in 5 ms.

At this point, the atoms are distributed among the magnetic sublevels of the $F = 2$ manifold. To maximize the transfer efficiency into the magnetic trap, they are optically pumped to the $|F = 2, m_F = 2\rangle$ stretched state. A weak, uniform magnetic field ($\approx$ 1 G) is created by the Helmholtz coils described in Section 3.2.2. This defines a quantization axis for the magnetic dipoles of the atoms. The optical pumping beam is turned on for 100 μs

and propagates along the quantization axis. Because it is σ^+ polarized and resonant with the $F = 2 \rightarrow F' = 2$ transition, the atoms are driven to the $|F = 2, m_F = 2\rangle$ dark state after several excitation cycles. The net result is modest heating ($\approx 5\,\mu$K) with a tremendous increase in transfer efficiency. Typically $\sim 73\%$ of the atoms end up in the $|F = 2, m_F = 2\rangle$ state, with the remaining in the $|F = 2, m_F = 1\rangle$ state.

Subsequent to optical pumping, all optical fields are shuttered, and the current in the quadrupole coils is switched on to $\sim$ 10 A in less than 5 ms. The dipoles align with the local quadrupole field and are trapped magnetically. The amount of current in the coils is chosen such that the resultant field gradient optimally mode-matches the cloud with the magnetic trap and minimizes heating.

Though the atoms are now in a magnetic trap, they are not necessarily in thermal equilibrium. By waiting for some time, the cloud could equilibrate through collisions. However, the collision rate at this point is low ($< 1\,$Hz) and so the equilibration time would be long. To speed up the process, the quadrupole current is linearly ramped to 20 A in 200 ms. This compresses and heats the cloud, resulting in an increased collision rate. After 5 s the cloud has equilibrated, and the current is ramped down to 15 A. The end result is an ensemble of $\sim 10^7$ rubidium atoms at a temperature of $\sim 50\,\mu$K.

One of the key parameters of the ensemble which is experimentally useful to control is its temperature. The majority of the ensemble's energy is gained when it is transferred to the magnetic trap, and this is a result of

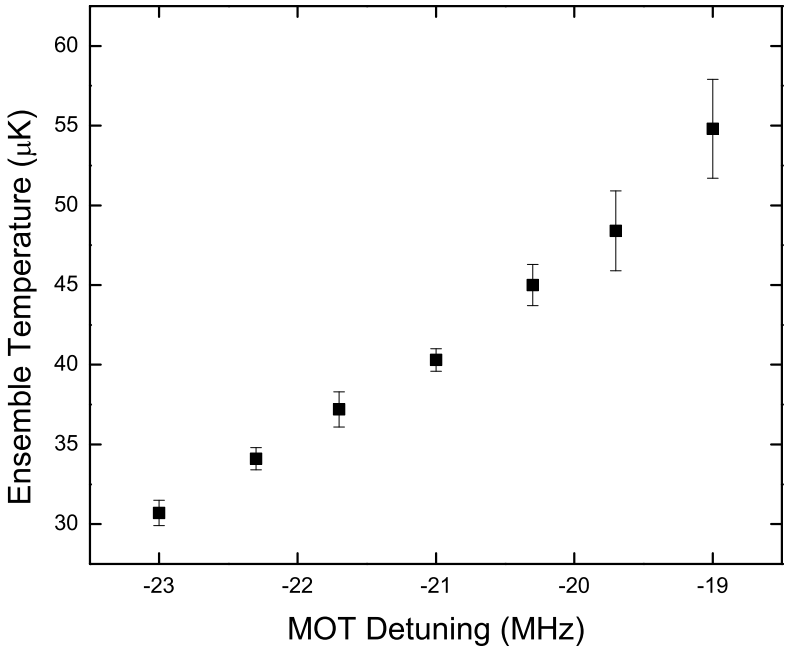

Figure 3.26: Ensemble temperature as a function of MOT laser detuning

its spatial extent. Because a MOT is density limited to $\sim 10^{11}/\,\mathrm{cm}^3$ [57], the number of atoms in the lower MOT, and hence its size, will be directly tied to the ensemble's final temperature. Therefore the ensemble temperature may be controlled by changing the loading rate of the lower MOT. This is achieved in the experiment by varying the MOT laser detuning. The effect is shown in Figure 3.26.

Chapter 4

Single-Photon Cooling of Rubidium

> "The strongest arguments prove nothing so long as the conclusions are not verified by experience. Experimental science is the queen of sciences and the goal of all speculation."
>
> -Roger Bacon

The first demonstration of single-photon cooling was achieved in 2008 in a proof-of-principle experiment [32]. Approximately 1.5×10^5 rubidium atoms were irreversibly transferred from a large volume, magnetically trapped ensemble to a small volume optical trap. This number was 23 times higher than the largest number of atoms that could be directly transferred to the optical trap (i.e. without cooling), and thus it was a clear signature that the entropy had been reduced.

This chapter details the second implementation of single-photon cooling, for which several key improvements were made. The most significant change was the conversion of the optical trap to a gravito-optical trap, already described in Section 3.3.2. The modified trap geometry was simpler and introduced fewer artifacts into the dynamics of the cooling process, making the fundamental mechanics of the technique more apparent and easier to

study. Additionally, the gravito-optical trap was effectively deeper, allowing for an order of magnitude more atoms to be captured. This increased both the accuracy and scope of the measurements made on the system.

4.1 Cooling Sequence

The starting point for the cooling experiment is a ^{87}Rb ensemble in a magnetic trap, prepared as described in Section 3.6. Typically, the magnetic trap starts with a radial field gradient $B'_\rho \approx 62\,\mathrm{G/cm}$. The size of the ensemble is dependent solely on its temperature (neglecting, for the moment, repulsive interactions), and a linear regression of measured data yields

$$\sigma_\rho = 8.46 + 6.19T, \tag{4.1}$$

where σ_ρ is the $1/\sqrt{e}$ Gaussian radius of the ensemble in μm and T is its temperature in μK.

The optical trough (Section 3.3.2) is positioned just beneath the magnetically trapped ensemble where the initial atomic density is negligible. A linearly polarized beam detuned slightly below the $F = 2 \rightarrow F' = 1$ transition is focused to a $1/e^2$ waist of 8 μm inside the trough. This beam plays the role of the demon in the cooling experiment. Figure 4.1 illustrates this configuration.

When atoms encounter the demon beam, they undergo a spontaneous Raman transition. The beam excites the atoms to the $|F' = 1, m_{F'} = 1\rangle$ state, in accordance with the electric-dipole selection rules ($\Delta m_F = \pm 1, 0$). From

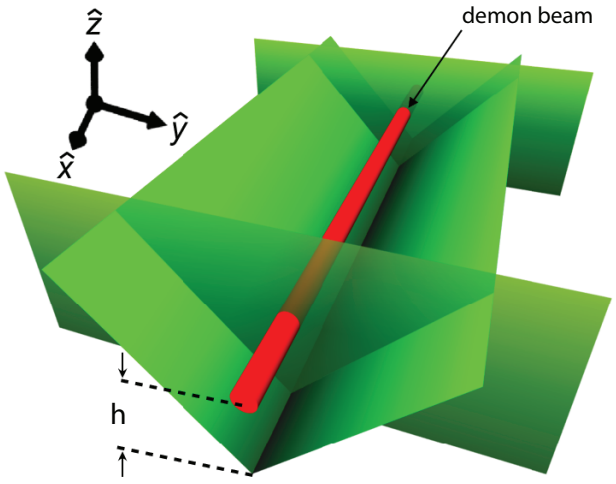

Figure 4.1: The demon beam is tightly focused inside the trough at a height h above the vertex. It drives an spontaneous Raman transition, transferring atoms irreversibly out of the magnetic trap and into the optical trough.

the branching ratios calculated in Section 2.3.1.2, it is predicted that 84% of the atoms decay from this state to the $F = 1$ ground state manifold. The remaining 16% are cycled back to the $F = 2$ manifold and re-excited.

A diagram of the experimental scheme and relevant energy levels is shown in Figure 4.2. Here $|i\rangle = |F = 2, m_F = 2\rangle$ is the initial state of the ensemble (neglecting the minority population with projection $m_F = 1$). The potential drawn for this state, as a function of the vertical coordinate z, represents the magnetic potential from the quadrupole field, the light shift from the optical trough, and the gravitational potential. The most energetic atoms of the ensemble have classical turning points at the location of the demon beam, which transfers them via the excited state $|e\rangle = |F' = 1, m_{F'} = 1\rangle$

to the state $|f\rangle = |F = 1, m_F = 0\rangle$ or $|F = 1, m_F = 1\rangle$. The potential for the former final state is due solely to the light shift of the trough and gravity, while the potential for the latter final state (a high-field seeker) also includes the magnetic interaction and thus should have a steeper gradient than is drawn. Both, however, are trapped states in the trough.

It should be noted that this is effectively an irreversible process. Atoms in state $|i\rangle$ readily scatter photons from the demon beam, but in state $|f\rangle$ they see a detuning of 6.8 GHz, the ^{87}Rb ground state hyperfine splitting. For the intensities relevant to this experiment (typically a few orders over the saturation intensity), state $|f\rangle$ is effectively a dark state which undergoes negligible scattering.

The experiment proceeds by adiabatically ramping off the current in the quadrupole coils in time $t_{\text{ramp}} \sim 1\,\text{s}$. This collapses the magnetic potential, and, as in Figure 1.3, pushes each atom toward the demon so that it is excited with little kinetic energy remaining. To ensure this, the adiabaticity condition $\langle \tau_B \rangle \ll t_{\text{ramp}}$ must be satisfied, where $\langle \tau_B \rangle \approx 20\,\text{ms}$ is the average oscillation period in the magnetic trap. Figure 4.3 shows the measured incremental atom accumulation in the trough as a function of the quadrupole ramp-off. It should be noted that, because the trough by itself is a conservative trap, any positive slope on this plot indicates irreversible transfer and hence a functioning demon.

In the first implementation of single-photon cooling (Reference [32]), the quadrupole trap was adiabatically translated toward the optical trap. In principle, this achieves the same effect as collapsing the magnetic potential

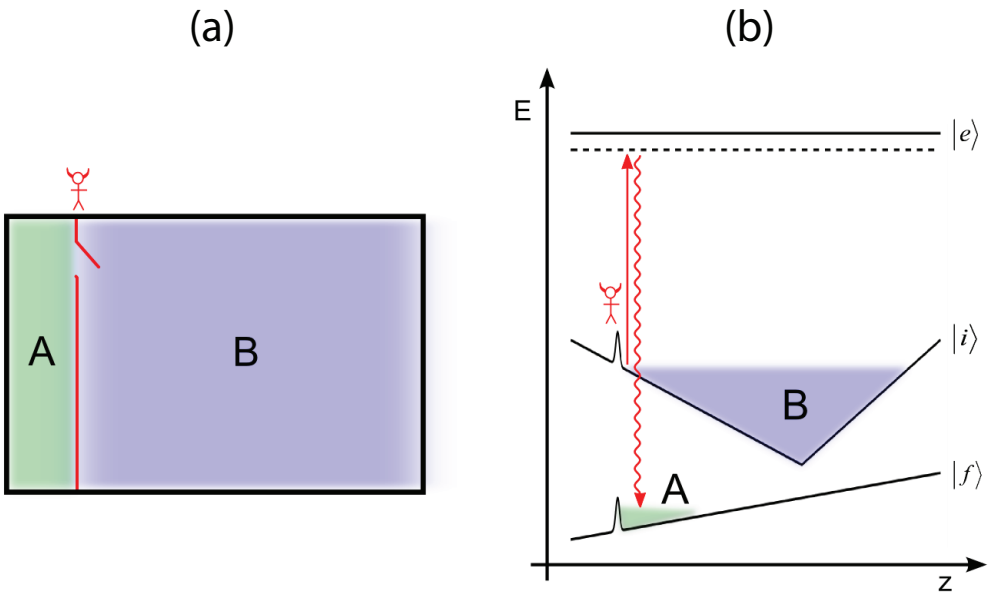

Figure 4.2: Single-photon cooling as Maxwell's demon. (a) Maxwell's demon operates a gate between two chambers, **A** and **B**. By functioning as a valve and allowing only one-way passage from **B** to **A**, the atoms are compressed without expenditure of work. (b) Schematic of single-photon cooling in a three-level system. Magnetically trapped atoms in state $|i\rangle$ occupy **B**. A spontaneous Raman transition is driven by the demon near each atom's classical turning point, transferring the atoms to state $|f\rangle$. These gravito-optically trapped atoms occupy **A**.

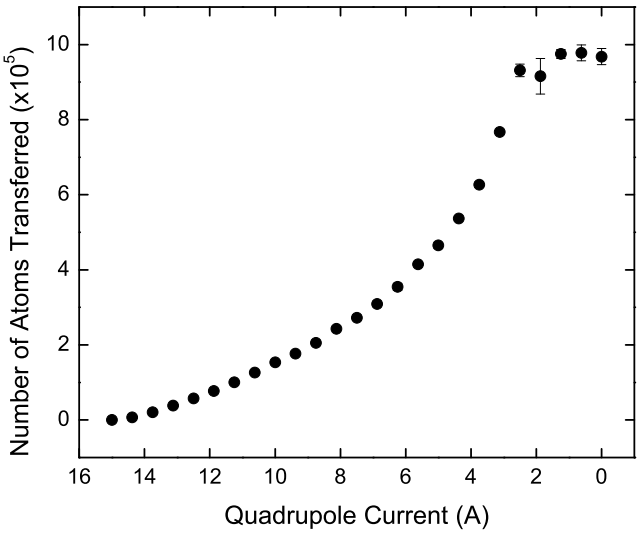

Figure 4.3: Incremental accumulation of atoms in the optical trough as a function of quadrupole current. Below 2.5 A, magnetically trapped atoms are no longer levitated by the quadrupole field gradient, and the cooling sequence is complete.

(see Figure 1.3). However, the latter method was found to be advantageous because the ensemble temperature is reduced as it expands. Thus collisions between optically trapped and magnetically trapped atoms occur at lower energies, resulting in less trap loss.

At this point, the cooling sequence is complete and the atoms are imaged, yielding information on atom number, spatial distribution, and temperature.

4.2 Analogs of the Demon

Though it is apparent from Figure 4.3 that, in general, a one-way valve is acting on the ensemble, there are several specific attributes of the demon which manifest themselves experimentally and merit closer examination. With the goal of the demon being to maximize entropy reduction, it is in fact crucial to account for these factors and tailor the experiment accordingly.

4.2.1 The Size of Chamber A

In a gradient confining potential, there is a one-to-one relationship between the spatial extent of an ideal gas and its temperature. For the magnetically trapped ensemble (chamber **B**), the temperature is controlled experimentally as described in Section 3.6. This, in turn, determines the size of **B**.

Following the same line of reasoning, one can see that the size of chamber A is determined predominantly by the distance h between the vertex of the optical trough and the demon beam (see Figure 4.4). After atoms have decayed to the $F = 1$ manifold by scattering a photon, they experience gravitational free fall or magnetic acceleration ($m_F = 1$ atoms) to the bottom of the trough. This acquired energy sets a limit on the minimum achievable temperature and hence the size of **A**.

Since the reduction of entropy scales inversely with the size of **A**, it is desirable to minimize the value of h. One might expect that the optimal strategy would be to largely overlap the demon beam and the trough beams

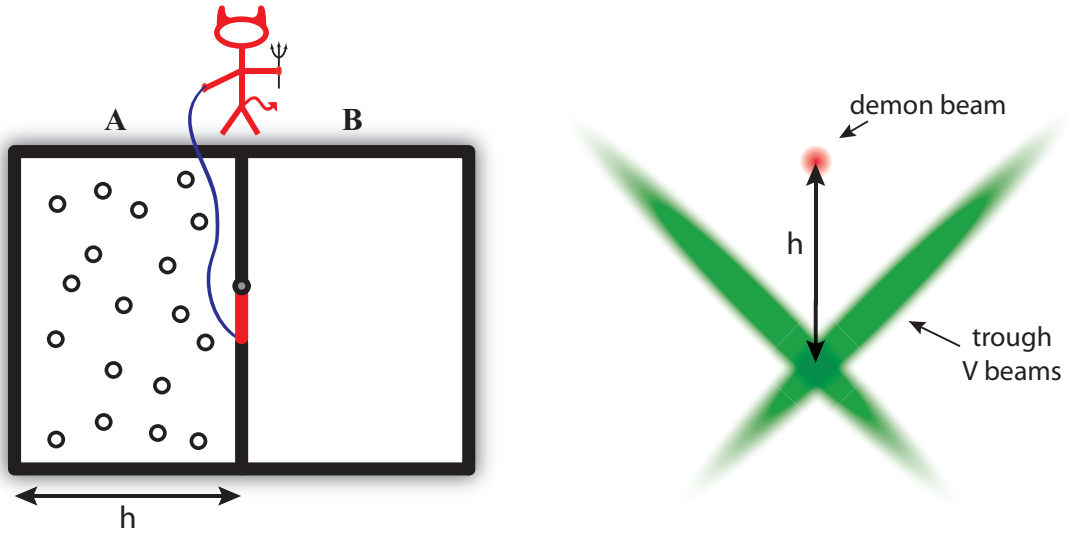

Figure 4.4: The size of Maxwell's chamber **A** corresponds to the height h of the demon beam above the optical trough vertex.

but allow the demon beam to leak out slightly above the vertex. Figure 4.5 shows that this is not the case. As the beams begin to overlap for small values of h, atoms climb the repulsive potential of the trough before the Raman transition occurs. The effect is the same as that of free fall: acquired energy and a larger chamber **A**.

4.2.2 The Size of the Gate

In Maxwell's thought experiment, the demon functions as a one-way valve by opening and closing a mechanical gate. This operation must be synchronized with the incidence of an atom, and it must be performed quickly to prevent reverse flow. In other words, if the gate size is large or it is operated

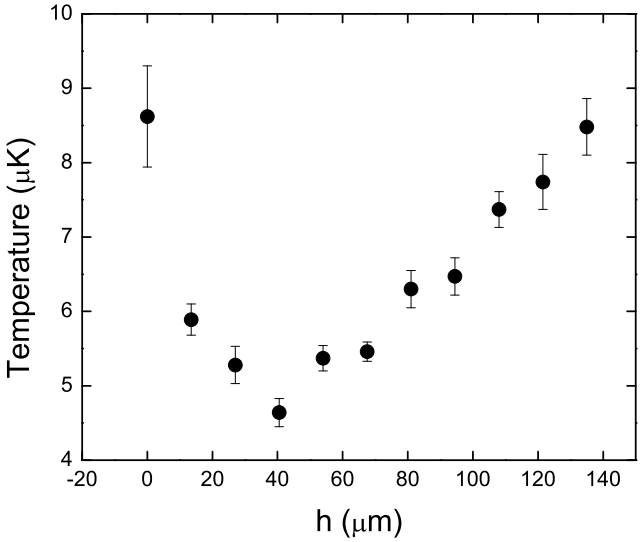

Figure 4.5: Relationship between demon beam height and temperature.

slowly, atoms will have a higher probability of retransiting the gate. There is a density threshold at which the valve can no longer act unidirectionally.

A direct analog to this density limit can be seen in the case of single-photon cooling, even though the gate is optical rather than mechanical. Irreversible transfer is ensured by the loss of the decay photon to the environment. Should this photon be reabsorbed before it is lost, as is increasingly likely with higher densities, atoms may escape from the optical trough through an additional decay cycle. One approach for mitigating this effect is to exploit the phenomenon of power broadening (see Figure 2.2). A high intensity optical field detuned from resonance can drive transitions at the same rate as a low intensity field on resonance. Due to energy conservation, the decay photons

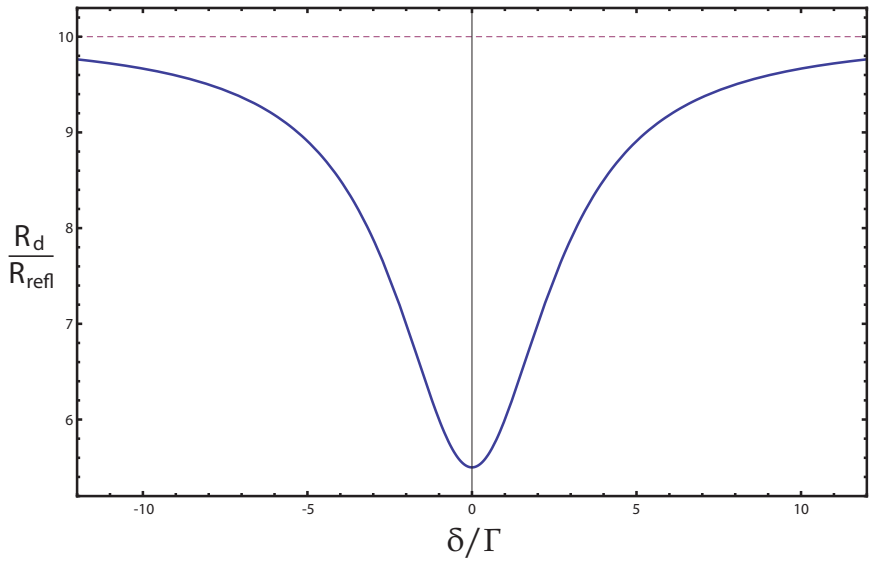

Figure 4.6: Plot of Equation 4.2 as a function of laser detuning in linewidths. The ratio of beneficial to detrimental scattering increases with greater detuning. In practice, a detuning of $\sim 6\Gamma$ is used.

are also detuned. These individual photons, however, produce a very small field and therefore, for large detunings, a negligible reabsorption rate. In the experiment, the demon beam is typically operated with a detuning of -35 MHz and a maximum intensity $I \sim 100 I_s$.

This effect is difficult to measure directly because it is partially masked by an artifact of the experimental apparatus, which, fortuitously, is mitigated in the same fashion. Because the experiment takes place in the science chamber, which is an uncoated glass cell, approximately 4% of the power from the demon beam is reflected at each surface. These reflections are divergent, and it is inevitable that some of the light is incident on the magnetic trap. This

leads to depopulation of the ensemble and a decrease in transfer to the optical trough. To see how detuning mitigates the problem, consider the scattering rate given by Equation 2.2. For a given saturation parameter of the demon beam $s_{\mathrm{d}} = I/I_{\mathrm{s}}$, the saturation parameter of the partially reflected beams in the magnetic trap will be proportional but smaller: $s_{\mathrm{refl}} = \alpha s_{\mathrm{d}}$ where $\alpha < 1$. Then the ratio

$$\frac{R_{\mathrm{d}}}{R_{\mathrm{refl}}} = \frac{1}{\alpha}\frac{1 + \alpha s_{\mathrm{d}} + (2\delta/\Gamma)^2}{1 + s_{\mathrm{d}} + (2\delta/\Gamma)^2} \tag{4.2}$$

compares beneficial scattering in the optical trough to detrimental scattering in the magnetic trap as a function of laser detuning. A plot of Equation 4.2 for a fixed saturation parameter is shown in Figure 4.6. As the detuning of the laser is increased, the effect of the partially reflected power is minimized. Of course, the intensity of the beam must also be increased with detuning to maintain a sufficient scattering rate in the trough.

Both of the above-described effects can be seen in Figure 4.7, which is a plot of the number of atoms transferred to the trough as a function of detuning, for several beam powers. The traces corresponding to 1.5 nW (green) and 15 nW (red) display a reabsorption-limited density near resonance. At 150 nW (black trace), partial reflections depopulate the magnetic trap and result in an even lower final density. Detuning is advantageous at all three powers, and the optimal amount is determined by balancing the excitation rate in the trough with the losses due to reabsorption and magnetic trap depopulation.

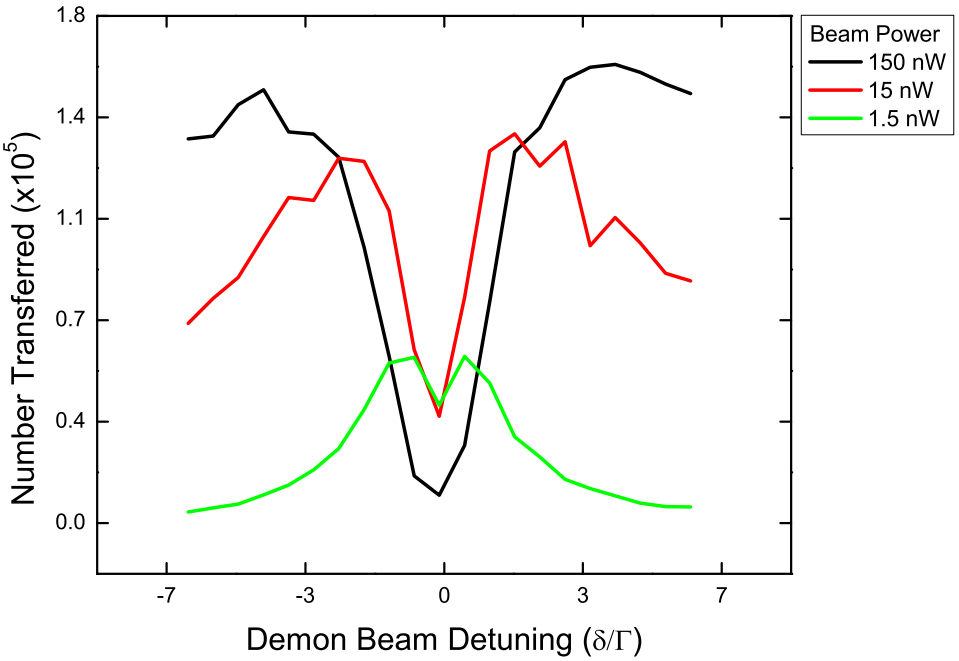

Figure 4.7: Final atom number as a function of demon beam detuning in linewidths. A resonant beam induces two loss mechanisms, both of which are mitigated by detuning the frequency and increasing the intensity.

4.2.3 Multiple Chambers

Because the irreversibility of the transfer mechanism in single-photon cooling relies on spontaneous decay, it is in general not possible to force all of the atoms into one final state–one must instead rely on favorable branching ratios to produce a desirable distribution of final states. The atoms transferred into the optical trough end up in a distribution of $F = 1$ sublevels, and, with respect to Maxwell's thought experiment, these sublevel populations should be considered as occupying separate chambers. The demon is, in this sense, inefficient; though it acts as a one-way valve, the valve has multiple output ports.

At the location of the optical trough–directly beneath the magnetic trap–the magnetic field lines are orthogonal to the propagation direction of the linearly polarized demon beam. Excitation of the magnetically trapped $|F = 2, m_F = 2\rangle$ atoms with linear polarization is impossible for the $F = 2 \rightarrow F' = 1$ transition, so they are excited by the σ^- component of this field to the $|F' = 1, m_{F'} = 1\rangle$ state. Atoms which begin in the $|F = 2, m_F = 1\rangle$ state are excited to the same state by absorption of a linearly polarized photon. From the excited state, 84% decay in equal proportion to the $m_F = 0$ and $m_F = 1$ sublevels in the $F = 1$ manifold, while approximately 15% are cycled back to the original states and a negligible remainder is lost to the $|F = 2, m_F = 0\rangle$ state.

The final distribution of states is measured by applying a strong magnetic field gradient after the cooling sequence has concluded. The gradient

ejects all magnetically coupled states from the trap, leaving only atoms in the $m_F = 0$ sublevel. As expected, the measurements show that these atoms constitute approximately 50% of the transferred population.

4.3 Analysis

Single-photon cooling, as implemented with the scheme discussed in this chapter and shown in Figure 4.2, is essentially a one-dimensional cooling technique. For an ideal gas in a magnetic quadrupole trap, energy distributions along orthogonal axes are uncorrelated. Therefore one would expect to achieve phase-space compression of the ensemble only along the vertical $\hat{\mathbf{z}}$ axis, with the transverse dimensions retaining their phase-space densities. This is apparent in Figure 4.5, where the lowest temperature measured (4.64 μK) is significantly higher than the fundamental limit of the technique, the recoil temperature $T_{\text{recoil}} = 362\,\text{nK}$.

Although there is an unmistakable increase in phase-space density in the optical trap as compared to the magnetic trap, the measured temperature is dominated not by the cooling technique but by the nature of the optical trap. Because it has a finite depth and size, both of which are smaller than that of the magnetic trap, the optical trough truncates the transverse phase-space distributions of the ensemble, resulting in a reduced temperature and size through the loss of atoms. This truncation can be controlled, as in Figure 4.8, by controlling the depth of the trap (through the power in the trough beams) or the size of the trap (through the spacing of the end caps).

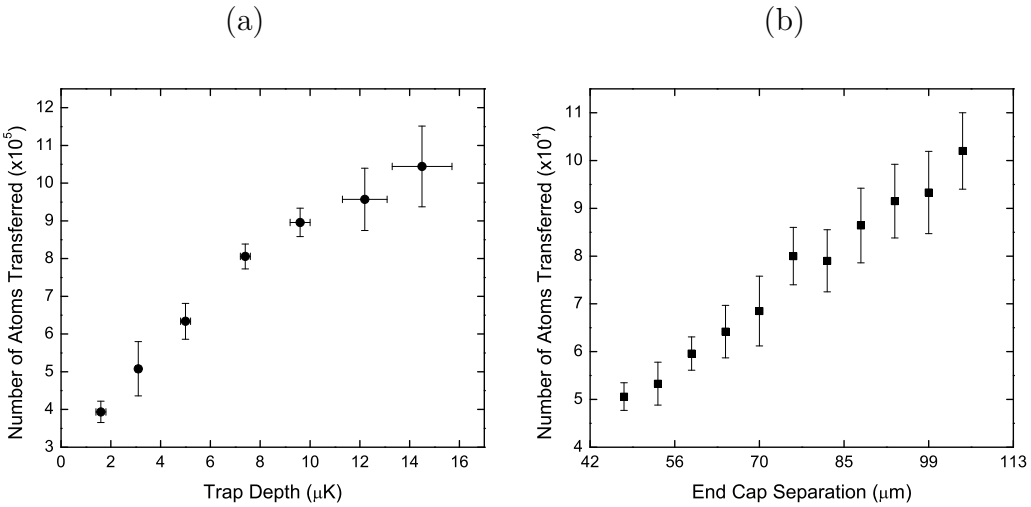

Figure 4.8: Effect of finite optical trap (a) depth and (b) size on the truncation of the ensemble. For deeper and larger traps, fewer atoms are lost.

As a consequence of this effect, measuring the temperature and size of the ensemble in the optical trough gives incomplete information on the cooling achieved by the technique. Rather, a more relevant metric for analyzing the vertical phase-space compression is the transfer efficiency–that is, the fraction of atoms transferred from the magnetic trap to the optical trap. To appreciate the value of this quantity, it is helpful to first develop an analytical model which describes the entire transfer process.

4.3.1 A Simple Model

To simplify the mathematics of the model tremendously, the spatial distribution of the ensemble is approximated as Gaussian, and it is assumed to have a Maxwell-Boltzmann velocity distribution. Strictly speaking, the

optical and magnetic traps are not harmonic potentials, and thus modeling the spatial distributions as Gaussian will introduce a small error. However, the utility of the model is not in its absolute precision but rather in its ability to expose the underlying physics of single-photon cooling.

In a single dimension denoted by the subscript i, the spatial distribution may be written as

$$n_{1D}(x_i) = \frac{N}{\sqrt{2\pi\sigma_i^2}} e^{-x_i^2/2\sigma_i^2}, \tag{4.3}$$

and the velocity distribution may be written as

$$f_{1D}(v_i) = \sqrt{\frac{m}{2\pi k_B T_i}} e^{-mv_i^2/2k_B T_i}. \tag{4.4}$$

For a given number of atoms N, these distributions are each characterized by single parameters: σ_i and T_i. The one-dimensional phase-space density $\rho_{1D} \propto N/\sigma_i\sqrt{T_i}$ (cf. Equation 2.1) is, at best, constant for a non-dissipative process, even if there are abrupt changes in the trap potential. This may be written explicitly as $\rho_{1D} = \rho'_{1D}$ or equivalently

$$\frac{N}{\sigma_i\sqrt{T_i}} = \frac{N'}{\sigma'_i\sqrt{T'_i}}, \tag{4.5}$$

where the primed variables refer to the transformed system. The transformation to be considered here is the result of the sudden switching of the trap potential from a large volume magnetic trap to a small, shallow optical trap with depth T'_i and width σ'_i. This necessarily induces a loss of atoms, and Equation 4.5 can be rearranged to define a maximum transfer efficiency:

$$\eta_i \equiv \frac{N'}{N} = \frac{\sigma'_i}{\sigma_i}\sqrt{\frac{T'_i}{T_i}}. \tag{4.6}$$

The assumptions of this equation are that $\sigma_i' \leq \sigma_i$ and $T_i' \leq T_i$. In the limit that these parameters are equal, the transfer efficiency is unity as should be expected. Equation 4.6 can be trivially extended to three dimensions in Cartesian coordinates as follows:

$$\eta = \prod_i \eta_i = \prod_i \frac{\sigma_i'}{\sigma_i} \sqrt{\frac{T_i'}{T_i}}, \tag{4.7}$$

where $i \in \{x, y, z\}$. This equation could be written more concisely for the case of thermalized ensembles ($T_i = T_j$) or isotropic traps ($\sigma_i = \sigma_j$), but it is left in long form for the sake of generality.

It is now straightforward to write an expression for the maximum expected transfer efficiency of single-photon cooling. Neglecting a photon recoil, the demon compresses the vertical dimension ($\hat{\mathbf{z}}$) of the ensemble completely in both position and momentum space. All that must be accounted for are the phase-space-conserving transfer efficiencies in the transverse dimensions. Noting that the ensemble is initially in thermal equilibrium ($T_x = T_y \equiv T$) and anisotropic ($\sigma_x = 2\sigma_y \equiv \sigma$), the upper bound for the transfer efficiency of single-photon cooling can be written as

$$\eta_{\text{spc}} = \prod_{i \in \{x,y,z\}} \frac{\sigma_i'}{\sigma_i} \sqrt{\frac{T_i'}{T_i}} = \frac{(\sigma_x' \sqrt{T_x'})(\sigma_y' \sqrt{T_y'})}{\frac{1}{2}\sigma^2 T}. \tag{4.8}$$

Any transfer efficiencies measured below this bound would indicate additional losses introduced by incomplete phase-space compression along $\hat{\mathbf{z}}$ or by heating.

All factors in the numerator of Equation 4.8 are constants which are set by the optical trough geometry and depth, so η_{spc} follows directly from

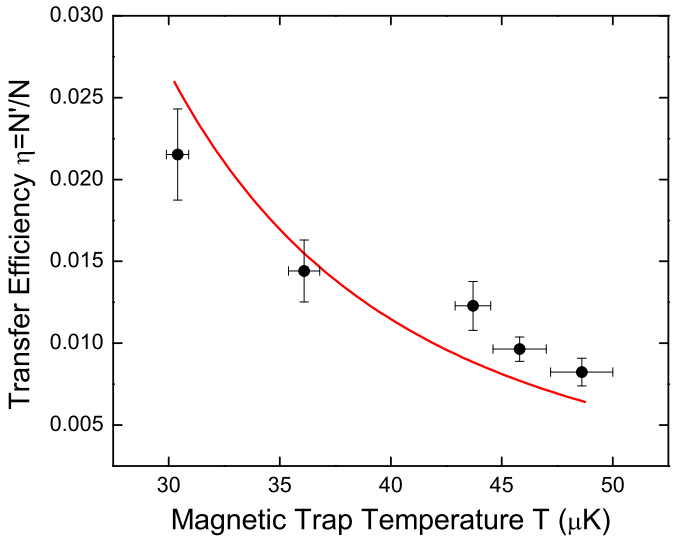

Figure 4.9: Measured transfer efficiency of single-photon cooling as a function of the initial magnetic trap temperature T. The red line is a plot of Equation 4.8.

the initial distributions of the magnetically trapped ensemble. Additionally, because $\sigma \propto T$ (see Equation 4.1), η_{spc} can be plotted as a function of the initial magnetic trap temperature T alone[1]. Figure 4.9 plots Equation 4.8 against measured data points.

The relevant optical trough parameters in this plot are $(T'_x,\ \sigma'_x) = (8.6\,\mu\mathrm{m},\ 39.9\,\mu\mathrm{K})$ and $(T'_y,\ \sigma'_y) = (2 \times 5.1\,\mu\mathrm{m},\ 40.4\,\mu\mathrm{K})$. There are two main points to make about these values. First, atoms do not have time to equi-

[1]One might point out that the adiabatic expansion of the magnetic trap during the experiment lowers the ensemble's temperature, and so it may seem a bit peculiar to insert only the initial value of the temperature into Equation 4.8. However, the term that appears in the denominator is $\sigma\sqrt{T}$, and this product is conserved during the adiabatic expansion.

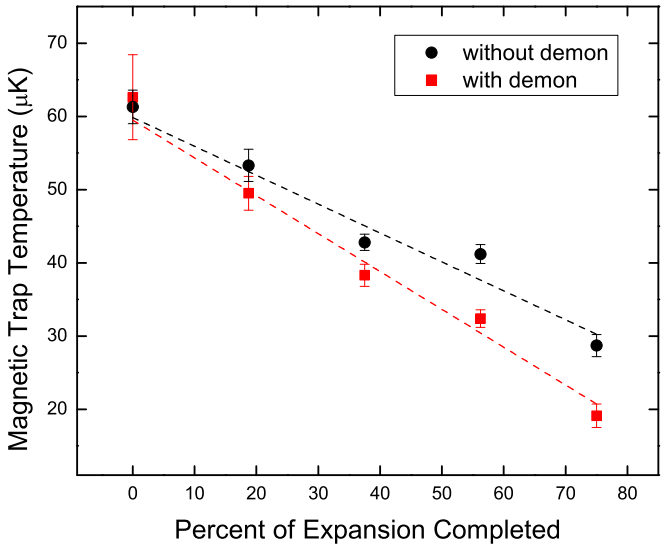

Figure 4.10: Magnetic trap temperatures at different stages of the cooling sequence. With the demon beam on (black squares), the ensemble's temperature is reduced by a greater amount than is caused by adiabatic expansion alone (red circles). The lower temperature is the result of evaporative cooling.

librate inside the trough. Thus the temperatures measured are unequal and correspond to the strength of the confining potential in either direction. The second point concerns the factor of 2 appearing in the value for T'_y, which is an artifact of the trough geometry. Because the trough beams propagating along $\hat{\mathbf{x}}$ are angled at 45°, half of the energy along $\hat{\mathbf{y}}$ is shifted to $\hat{\mathbf{z}}$ after atoms are transferred into the trough. Therefore the measured temperature, 5.1 μK, represents only half of the effective capture depth along $\hat{\mathbf{y}}$.

The data in Figure 4.9 show fairly close agreement with the model, but it seems that the cooling outperforms the model at higher magnetic trap

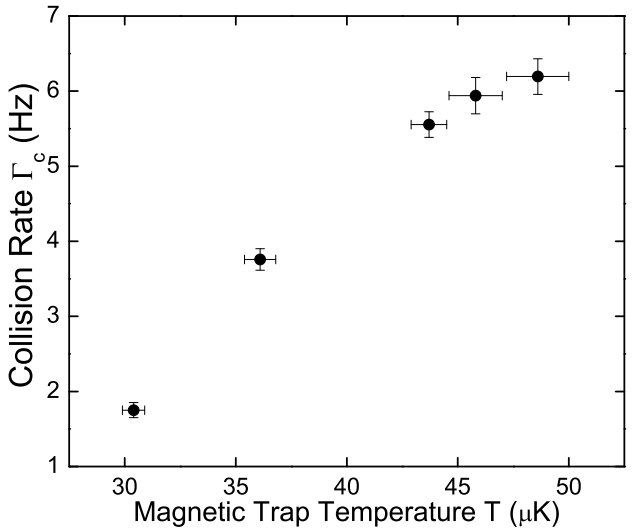

Figure 4.11: The collision rate in the magnetic trap increases monotonically as a function of temperature. This explains the increased transfer efficiency (with respect to the model) for higher initial temperatures.

temperatures. This is due to an effect predicted to occur in [28]. Single-photon cooling has, thus far, been presumed to be a nonequilibrium process, operating on an ideal gas which cannot rethermalize once its distribution is truncated by the demon. As an experimental technique, the fact that cooling can occur out of equilibrium can be quite advantageous, as discussed in Section 4.4. However, a physical gas can equilibrate through collisions after truncation. If the truncated atoms represent the high-energy tail of the distribution, the gas will rethermalize at a lower temperature. This is the basis of evaporative cooling. Figure 4.10 shows evidence that rethermalization occurs during the expansion of the magnetic trap.

Continuous thermal equilibration of the magnetically trapped ensemble, even if incomplete, provides an additional source of phase-space compression. This, in turn, can lead to better performance than predicted by Equation 4.8. To explain the correlation between performance and temperature in Figure 4.9, note that the rate of equilibration is governed by the single-particle collision rate, which is given by

$$\Gamma_{\mathrm{c}} = \frac{1}{N} \int n(\mathbf{r})^2 \sigma_s \langle v_r \rangle d\mathbf{r}, \tag{4.9}$$

where $n(\mathbf{r})$ is the atomic density, σ_s is the s-wave scattering cross section, and $\langle v_r \rangle = \sqrt{16 k_B T / \pi m}$ is the mean relative speed in a three-dimensional Boltzmann distribution. This rate is plotted in Figure 4.11 for the same ensembles as in Figure 4.9. The collision rate increases monotonically with temperature for these data points, implying that more equilibration occurs in these ensembles during the cooling experiment. Hence a greater transfer efficiency is expected, in agreement with the measured data.

4.3.2 Phase-Space Compression

It is clear from Equation 4.8 that the transfer efficiency may be increased by modifying the transverse phase-space overlap of the two traps (i.e., by decreasing the size and temperature of the magnetic trap or increasing the size and depth of the optical trap). However, phase-space compression is typically the important figure of merit for cooling experiments, as discussed in Section 2.2. One can use the analytical model to derive a simple expression

for the phase-space compression of a non-interacting ensemble:

$$\frac{\rho'}{\rho} = \frac{\sigma}{\sigma'_z}\sqrt{\frac{T}{T'_z}}, \tag{4.10}$$

For a fixed optical trough geometry and depth, the phase-space compression increases with the magnetic trap temperature in spite of a corresponding decrease in transfer efficiency.

This equation underestimates the phase-space compression if elastic collisions occur in the ensemble, which is the case for high initial temperatures. The greatest observed compression started with an ensemble of 1.2×10^8 atoms with $T = 53\,\mu$K and $\sigma = 515\,\mu$m. Noting that 73% were in the $|F = 2, m_F = 2\rangle$ state, this corresponds to a peak phase-space density $\rho = 1.4 \times 10^{-6}$. Out of this ensemble, 0.3% (3.3×10^5 atoms) were transferred to the optical trough at a final temperature of 4.3 μK, amounting to a peak phase-space density $\rho' = 4.9 \times 10^{-4}$. This value is for atoms in the $|F = 1, m_F = 0\rangle$ state, which account for 50% of the final population. The net compression of phase-space density is by a factor of 360.

4.4 Discussion

In addition to being interesting in the context of Maxwell's thought experiment, single-photon cooling is appealing because of its potential as a useful and effective cooling technique. This stems largely from its generality, especially in light of the restrictive nature of the commonly used techniques in the cold atom community. For single-photon cooling to work, only two re-

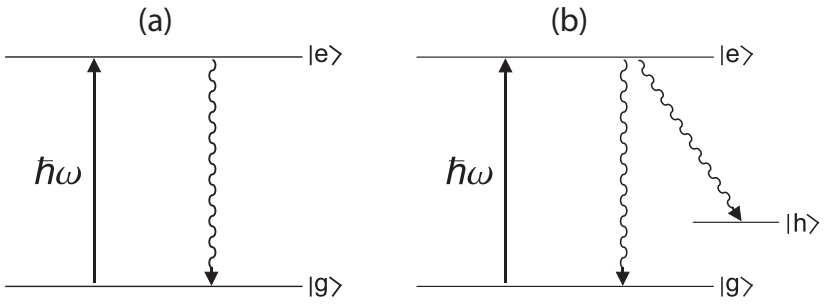

Figure 4.12: (a) Traditional laser cooling techniques require an atom to scatter thousands of photons, and so a closed cycling transition is crucial. (b) If the excited state can decay to a different ground state, the atom leaves the cooling cycle, and laser cooling fails.

quirements must be met: First, the atom to be cooled must possess a magnetic moment in the ground state (or a metastable excited state). Nearly the entire periodic table meets this condition. Second, there must be a laser-accessible transition to an excited state that can decay to a dark state.

Traditional laser cooling techniques, such as optical molasses (Section 2.3.1.1), work only on two-level atoms (Figure 4.12a). These techniques rely on momentum transfer between atoms and photons, and, because of the minuscule amount of momentum a photon carries, many thousands of photons must be scattered by each atom to obtain significant cooling. If an atom decays even once to a different ground state which is no longer resonant with the laser, it is effectively lost (Figure 4.12b). As is the case with the alkaline earth metals, additional lasers can sometimes be introduced to pump these lost atoms back into the cooling cycle. However, doing so exponentially increases the complexity of the experiment and is not feasible for most atoms, ergo only

a handful of atoms in the periodic table are amenable to laser cooling. In contrast, single-photon cooling is *prohibited* for two-level atoms. Because it doesn't rely on momentum transfer but instead reduces entropy directly, only one photon is required to achieve substantial cooling.

Another cooling technique commonly used to bring atoms to degeneracy is evaporative cooling. Though it might seem to be a universal technique, one could argue that it is just as restrictive as laser cooling. The technique relies on a large interatomic scattering cross section as well as a high initial density to provide an appreciable collision rate. Furthermore, collisions must be elastic; inelastic collisions will eject atoms from the magnetic trap. Because it is an inherently lossy technique, one must also start with a large number of atoms. Although single-photon cooling is aided by collisions, they are not required. Continuous equilibration is also not required, so single-photon cooling can proceed at a much faster rate than evaporation.

As an example of its generality, single-photon cooling can even be applied to molecules [35], which have seen extremely limited progress in regard to laser cooling. Consider, for example, the scheme presented in Figure 4.13. An ensemble of NH radicals is magnetically trapped in the $^3\Sigma^-$ $|\nu = 0, J = 1, N = 2, m_J = -1\rangle$ state, where ν, J, N, and m_J are the vibration, total rotation, nuclear rotation, and total angular momentum projection quantum numbers, respectively. A 336 nm photon from the demon laser excites each molecule at its classical turning point to the $^3\Pi_1$ manifold, irreversibly transferring $\sim 35\%$ of the population (defined by the Hönl-London and Franck-

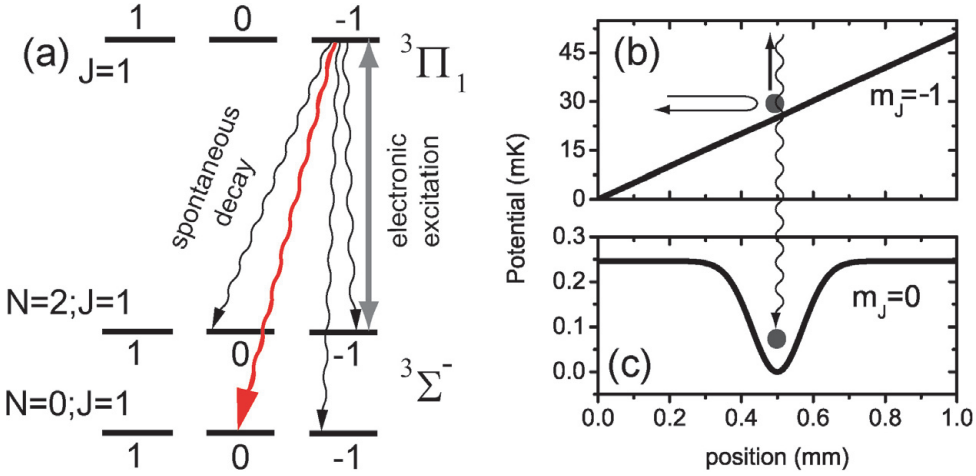

Figure 4.13: Single-photon cooling of an NH radical. (a) Level structure and relevant transitions. (b) Potential diagram for initial state. (c) Potential diagram for final, optically trapped state. [35]

Condon factors) to the nonmagnetic $^3\Sigma^-$ $|\nu = 0, J = 1, N = 0, m_J = -1\rangle$ ground state through the spontaneous decay of a photon.

As opposed to the repulsive optical trap in which rubidium atoms were accumulated, the NH radicals are transferred into an red-detuned, attractive optical trap. The relevant potentials are shown in Figures 4.13b and 4.13c. While the optical potential is eclipsed by the magnetic coupling for the initial state, the final nonmagnetic state encounters an unambiguous trapping potential. The cooling sequence then proceeds by adiabatically translating the magnetic trap toward the optical trap, which can be carried out as demonstrated in Figure 3.7.

Single-photon cooling is a particularly promising technique in light of recent progress with supersonic beams, much of which has been pioneered

in the Raizen Group. Experiments have demonstrated complete deceleration of pulsed supersonic beams of atoms [90, 91] and molecules [92–95]. These techniques are completely general, and they lead to trapped samples of any paramagnetic species at temperatures in the tens of millikelvins. Because of its unrestrictive nature, single-photon cooling is a prime candidate to further cool these ensembles.

Chapter 5

RF-Dressed Single-Photon Cooling

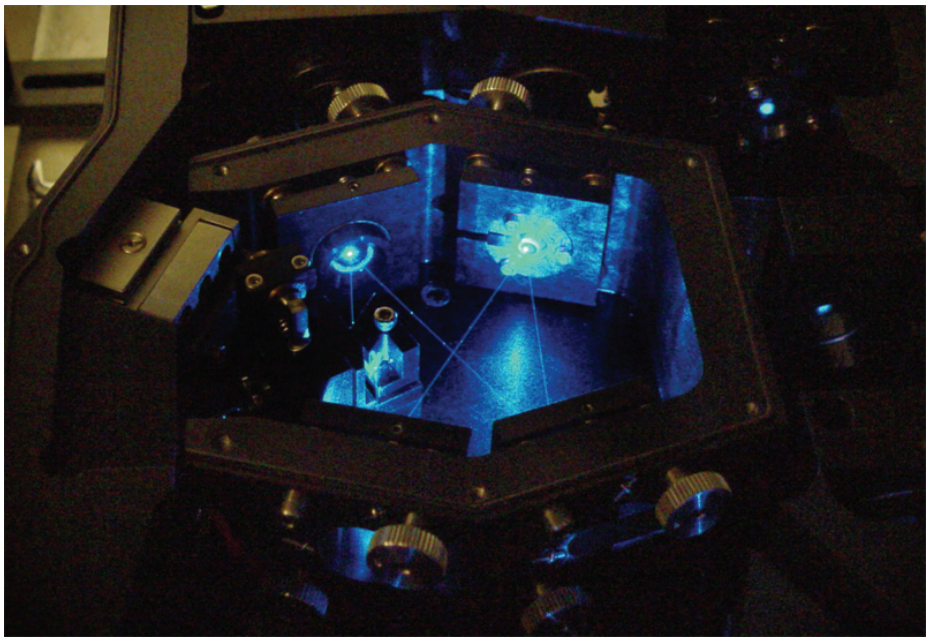

Single-photon cooling, as implemented in Chapter 4, is a versatile and effective technique, yet, in a practical sense, it suffers from one principal limitation: the ensemble is cooled in only one dimension due to the relative geometries of the initial (magnetic) and final (optical) traps. This not only limits the final temperature, but it also results in a loss of atoms for a final trap which is shallower than the initial ensemble temperature.

Cooling in three dimensions is possible with a final trap which forms

a surface surrounding the initial trap. Though it is not apparent how this could be implemented with an optical potential, it is relatively straightforward to create such a trap using a combination of static and radio-frequency (RF) magnetic fields. This chapter introduces so-called *RF-dressed states* and shows how single-photon cooling can be implemented using them. Atomic hydrogen is discussed as an example, and the apparatus being built toward the goal of cooling hydrogen and its isotopes is described.

5.1 RF-Dressed States

An atom in an external electromagnetic field can be described in the dressed state picture, where the atom is "dressed" with an external photon which couples two internal states and shifts their energies [96]. When the internal states are hyperfine levels of the electronic ground state, spontaneous relaxation of the states is negligible, and a resonant RF or microwave field in combination with a static magnetic field can create a conservative potential. RF-dressed potentials were first proposed for trapping neutral atoms in 2001 [97] and subsequently demonstrated in 2004 [98]. Since then, the versatility of RF-dressing has enabled numerous interesting applications, including the creation of novel trap geometries [99–101] and atomic beamsplitters [102].

5.1.1 Derivation

Consider the coupling of atoms in a magnetic trap to an RF magnetic field. This interaction has been analyzed in detail in [70, 103–105]. Only a

brief description will be given here. The Zeeman Hamiltonian for this system is given by

$$H = g_F \mu_B \mathbf{F} \cdot \mathbf{B}(\mathbf{r}, t) = g_F \mu_B \mathbf{F} \cdot [\mathbf{B}_{\mathrm{T}}(\mathbf{r}) + \mathbf{B}_{\mathrm{RF}}(\mathbf{r}, t)], \tag{5.1}$$

where $\mathbf{F}$ is the total atomic angular momentum operator and $\mathbf{B}_{\mathrm{T}}(\mathbf{r})$ is the static field of the trap. Let the RF field be written as

$$\mathbf{B}_{\mathrm{RF}}(\mathbf{r}, t) = \mathbf{B}^a_{\mathrm{RF}}(\mathbf{r}) \cos(\omega_{\mathrm{RF}} t) + \mathbf{B}^b_{\mathrm{RF}}(\mathbf{r}) \cos(\omega_{\mathrm{RF}} t + \delta). \tag{5.2}$$

The Hamiltonian may be diagonalized by making two transformations. The first transformation rotates the static field of the trap so that the trap interaction is diagonal: $[\mathcal{R}_{\mathrm{T}} \mathbf{B}_{\mathrm{T}}(\mathbf{r})]\mathbf{F} = |\mathbf{B}_{\mathrm{T}}(\mathbf{r})| F_z$. The second transformation rotates the frame about the direction of the local trap field at angular velocity ω_{RF}. Resulting terms oscillating at frequency $2\omega_{\mathrm{RF}}$ are discarded (the rotating wave approximation), and the final Hamiltonian can be expressed as

$$H = \left[g_F \mu_B |\mathbf{B}_{\mathrm{T}}(\mathbf{r})| - \frac{g_F}{|g_F|} \hbar \omega_{\mathrm{RF}} \right] F_z + \frac{g_F \mu_B}{2} \begin{pmatrix} \overline{B}_x \\ \overline{B}_y \end{pmatrix}^T \begin{pmatrix} F_x \\ F_y \end{pmatrix}, \tag{5.3}$$

where the transformed RF field $\overline{\mathbf{B}}$ is given by

$$\overline{\mathbf{B}} = \mathcal{R}_{\mathrm{T}} \mathbf{B}^a_{\mathrm{RF}}(\mathbf{r}) + \mathcal{R}_\gamma \mathcal{R}_{\mathrm{T}} \mathbf{B}^b_{\mathrm{RF}}(\mathbf{r}). \tag{5.4}$$

Here $\mathcal{R}_\gamma$ is a rotation matrix about the direction of the local magnetic field by angle $\gamma = -\frac{g_F}{|g_F|}\delta$.

For an $F = 1$ system, the eigenstates of this Hamiltonian can be expressed in terms of the un-dressed (or bare) states as a function of a single

parameter θ:

$$|\tilde{m}=1\rangle = \frac{1}{2}\Bigg[(1+\cos\theta)|m_F=1\rangle + \sqrt{2}\sin\theta|m_F=0\rangle + \frac{\sin^2\theta}{1+\cos\theta}|m_F=-1\rangle\Bigg] \tag{5.5a}$$

$$|\tilde{m}=0\rangle = \frac{1}{2}\Bigg[-\sqrt{2}\sin\theta|m_F=1\rangle + 2\cos\theta|m_F=0\rangle + \sqrt{2}\sin\theta|m_F=-1\rangle\Bigg] \tag{5.5b}$$

$$|\tilde{m}=-1\rangle = \frac{1}{2}\Bigg[(1-\cos\theta)|m_F=1\rangle - \sqrt{2}\sin\theta|m_F=0\rangle + \frac{\sin^2\theta}{1-\cos\theta}|m_F=-1\rangle\Bigg], \tag{5.5c}$$

where $\tilde{m}$ is the dressed state quantum number. The mixing angle θ is defined by the relation $\tan\theta = \sqrt{2}\Omega/\Delta$, where

$$\Omega = -\frac{1}{2}\langle m_F=\pm1|\boldsymbol{\mu}\cdot\boldsymbol{B}_{\mathrm{RF}}|m_F=0\rangle = \frac{g_F\mu_B}{2\hbar}\sqrt{\overline{B}_x^2+\overline{B}_y^2} \tag{5.6}$$

is the Rabi frequency and $\Delta = \omega_{\mathrm{RF}} - \omega_L$. Here $\omega_L = \mu B_{\mathrm{T}}/\hbar$ is the Larmor precession frequency. The eigenstate decompositions are plotted in Figure 5.1.

5.1.2 The Ioffe-Pritchard Magnetic Trap

Adiabatic rotation of the atomic angular momentum depends on a non-vanishing Rabi frequency. It can be seen from Equation 5.6 that this is only the case when there is a component of the RF field which is orthogonal to the trap field. When the two fields are parallel, $\Omega = 0$ and an atom will remain in its bare state. With a magnetic quadrupole trap, there are always points at which the fields are parallel for linear RF polarization. Circular polarization,

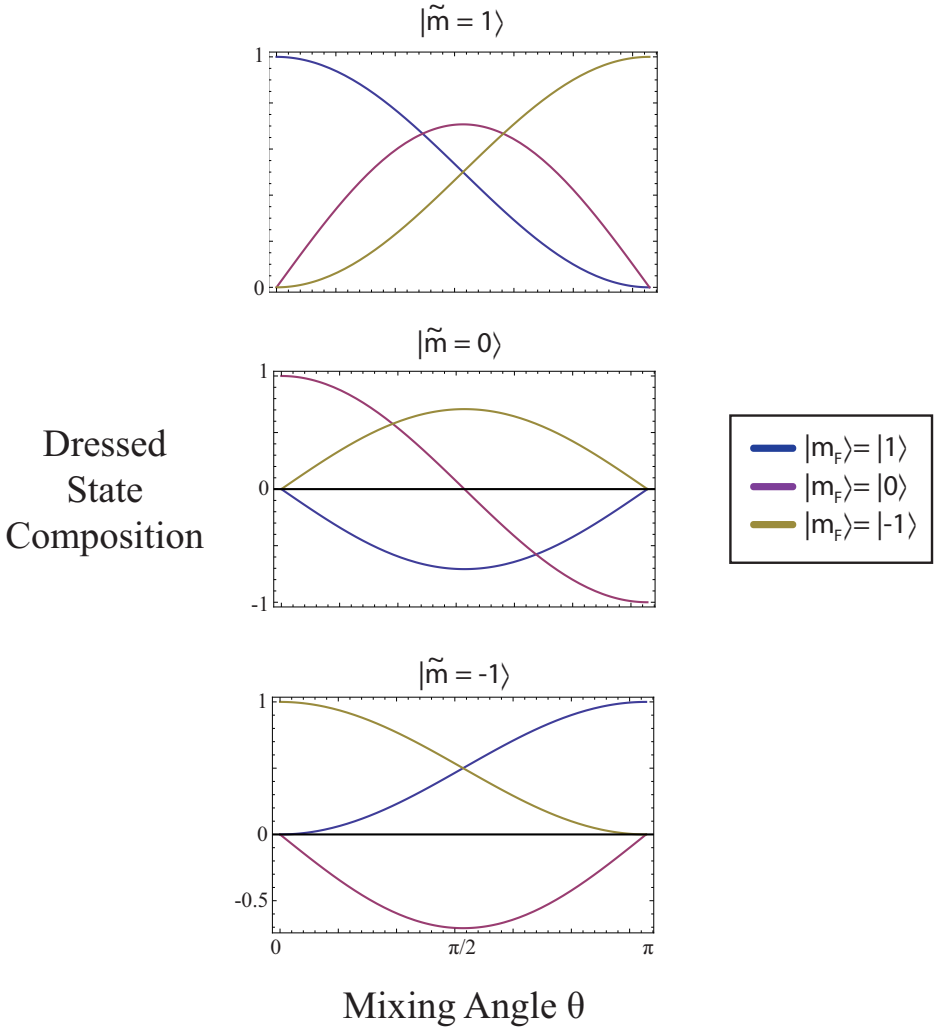

Figure 5.1: Decomposition of the RF-dressed states for a spin-1 atom. The atom's spin is adiabatically rotated as it passes through the region where $\omega_L \approx \omega_{\mathrm{RF}}$. The coordinate $\theta = \tan^{-1}\left[\sqrt{2}\Omega/(\omega_L - \omega_{\mathrm{RF}})\right]$, so the resonance condition occurs at $\theta = \pi/2$.

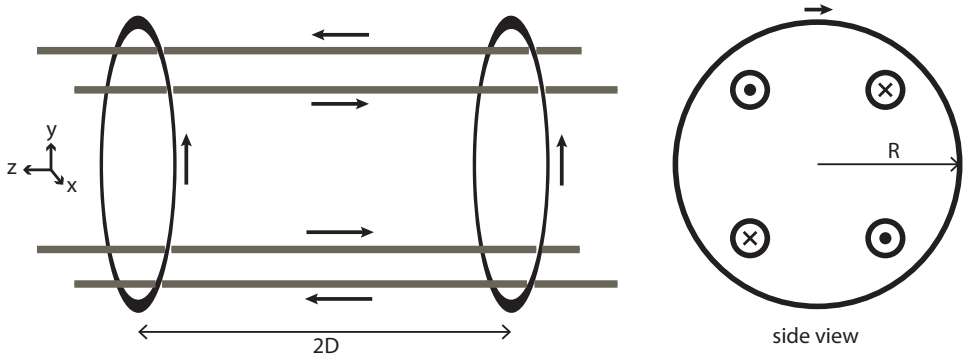

Figure 5.2: The Ioffe-Pritchard magnetic trap. Current through four straight bars creates a radial quadrupole field, while two pinch coils provide axial confinement. The arrows indicate the direction of the current.

on the other hand, would have opposite handedness on either side of the field minimum, leading to non-adiabatic rotation. These properties prevent the creation of perfectly adiabatic RF-dressed potentials [100]. To avoid this, traps with offset fields are typically used in RF-dressing experiments. The RF polarization is set to be orthogonal to the offset field, and the result is a non-vanishing Rabi frequency at all points.

A commonly used trap with an offset field is the Ioffe-Pritchard magnetic trap [58, 106], a schematic of which is depicted in Figure 5.2. Near the center of the trap, the field is given, in cylindrical coordinates $(\hat{\boldsymbol{\rho}}, \hat{\boldsymbol{\phi}}, \hat{\mathbf{z}})$, by

$$\mathbf{B}_{\mathrm{IP}} = B_0 \begin{pmatrix} 0 \\ 0 \\ 1 \end{pmatrix} + B'\rho \begin{pmatrix} \cos(2\phi) \\ -\sin(2\phi) \\ 0 \end{pmatrix} + \frac{B''}{2} \begin{pmatrix} -z\rho \\ 0 \\ z^2 - \rho^2/2 \end{pmatrix}. \tag{5.7}$$

Here the first term is the homogeneous offset field from the Helmholtz pair, the second term is a radial quadrupole field created by the bars, and the third term is a quadratic field generated by the Helmholtz pair. The magnitude

of the quadratic term, which provides axial confinement, is dependent on the geometry of Helmholtz coils as follows:

$$B'' = 6B_0 \frac{4D^2 - R^2}{(D^2 + R^2)^2}, \tag{5.8}$$

where $2D$ is the separation of the coils and R is the radius.

5.1.3 Adiabatic Potentials

The adiabatic dressed-state potentials corresponding to the Hamiltonian of Equation 5.3 are given by

$$U = \tilde{m}\sqrt{(|g_F \mu_B \mathbf{B}_\mathrm{T}| - \hbar\omega_\mathrm{RF})^2 + (\hbar\Omega(\mathbf{r}))^2}. \tag{5.9}$$

For a circularly polarized RF field in the $(\hat{\boldsymbol{\rho}}, \hat{\boldsymbol{\phi}})$ plane, the Rabi frequency $\Omega(\boldsymbol{r})$ may be approximated as independent of $\boldsymbol{r}$. The potentials for the bare states as well as the dressed states are shown in Figure 5.3 for $\omega_\mathrm{RF} > \omega_0$, where $\omega_0 = \mu B_0/\hbar$ is the Larmor frequency at the trap minimum.

At this point, the attraction of the RF-dressed potentials for single-photon cooling should be clear. With a suitable demon, atoms initially in state $|\tilde{m} = -1\rangle$ can be irreversibly transferred into state $|\tilde{m} = 1\rangle$ at their classical turning points, compressing and cooling the ensemble in all three dimensions.

5.2 The Dressed State Demon

To be effective, the demon in single-photon cooling must operate at a well-defined position. Spatial selectivity is crucial to maximizing entropy

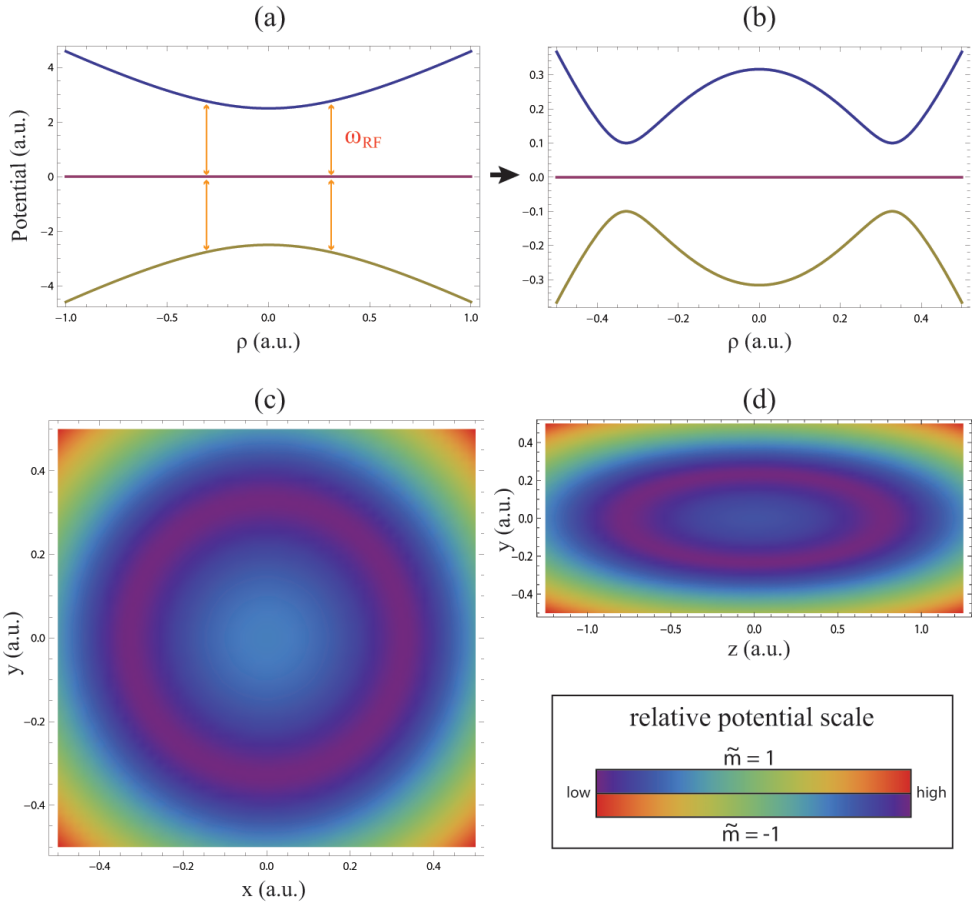

Figure 5.3: RF-dressed potentials in the Ioffe-Pritchard trap. (a) Bare state potentials as a function of radial coordinate. (b) RF-dressed potentials as a function of radial coordinate. (c) and (d) Two-dimensional plots of RF-dressed potentials show that a shell-like potential ($\tilde{m} = 1$) surrounds an inner trap potential ($\tilde{m} = -1$).

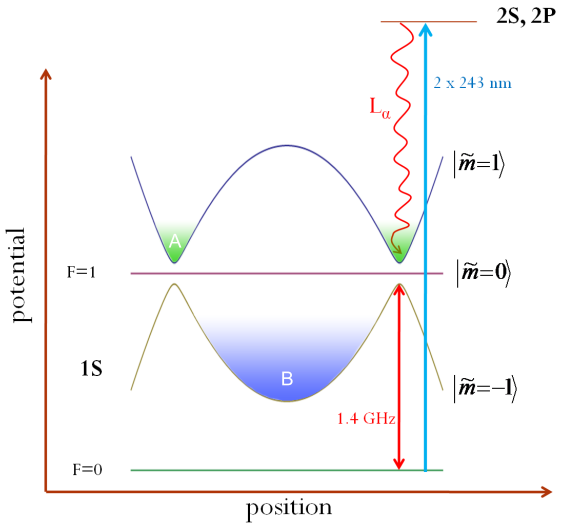

Figure 5.4: RF-dressed energy levels and the demon for atomic hydrogen. Atoms are transferred from the $|\tilde{m} = -1\rangle$ dressed state (chamber **B**) to the $|\tilde{m} = 1\rangle$ dressed state (chamber **A**) with the combination of a 1.4 GHz microwave transition and a two-photon optical transition, followed by a spontaneous decay.

reduction (see Section 4.2.1). When transferring atoms into an optical trap, spatial selectivity is easily achieved by tightly focusing the resonant beam inside the trap. However, it is, in general, not possible to do this over an extended surface such as the trap minimum of the $|\tilde{m} = 1\rangle$ state. The additional hyperfine structure of the ground state can be exploited to circumvent this problem.

Figure 5.4 depicts such a demon for the energy levels of atomic hydrogen initially in the $1^2S_{1/2}$ electronic configuration. Spatial selectivity is achieved by a microwave transition that couples the $|F = 1, \tilde{m}_F = -1\rangle$ state to the $F = 0$ manifold at the avoided crossings of the RF-dressed states. A 243

nm laser, which need not be focused at this location, drives a resonant two-photon transition to an excited state that decays to the $|\tilde{m}_F = 1\rangle$ state. This completes the irreversible transfer step. For hydrogen, the excited state configuration $2^2S_{1/2}$ is metastable ($\tau \approx 122\,\mathrm{ms}$) [107], but a modest electric field mixes it with the $2^2P_{1/2,\,3/2}$ states which quickly decay via emission of a Lyman-α photon.

A few words should be said on the irreversibility of this transfer step. In Chapter 4, irreversibility was ensured because the final state was in a different hyperfine manifold than the initial state. Thus the demon beam was detuned by the hyperfine splitting, leading to a negligible excitation rate. Conversely, with the scheme presented here, the final and initial states are in the same manifold. However, the degeneracy of the states is lifted by the vectorial coupling to the RF magnetic field. The Rabi splitting separates the dressed states and allows the microwave transition (which has a negligibly small linewidth) to occur only for the $|\tilde{m} = -1\rangle$ state.

Unlike the scheme described in Chapter 4, the cooling process cannot work by ramping off the magnetic potential. Doing so would not only ramp off the final trapping potential, but because the position of the avoided crossing is dependent on the magnetic field strength, the position of the demon would expand just as the ensemble would. Rather, cooling must proceed by translating the demon, as in Figure 1.3b. To do this, the RF frequency is swept downward, collapsing the outer dressed state radially (Figure 5.5). The picture is reminiscent of evaporative cooling, where atoms would be discarded

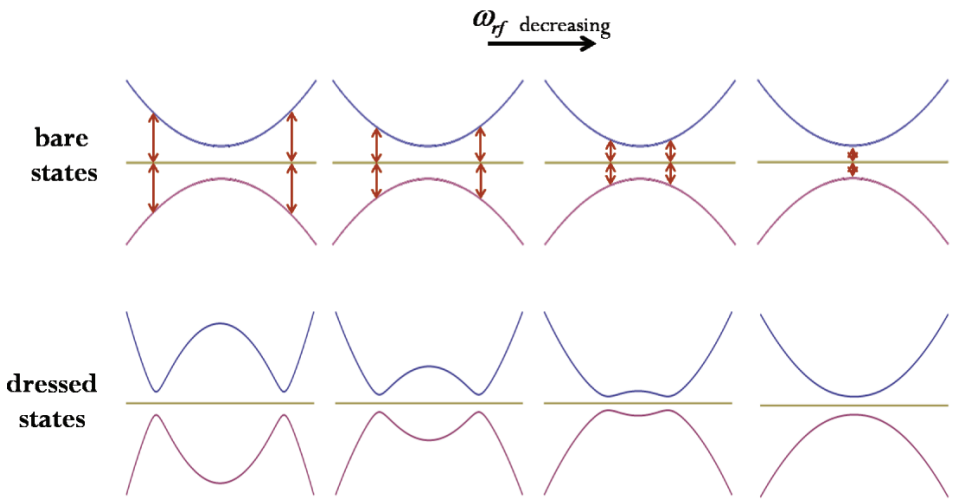

Figure 5.5: Sweep of the RF frequency. The outer shell potential collapses radially and finally resembles the initial low-field seeking state.

as they pass the avoided crossing of the $|\tilde{m} = -1\rangle$ state. With single-photon cooling, these atoms are instead saved by transferring them to $|\tilde{m} = 1\rangle$.

It should be noted that the outer dressed state potential forms an essentially lossless trap. Non-adiabatic Landau-Zener tunneling may occur through the avoided crossings with probability [100, 108]

$$p_{\mathrm{LZ}} = 1 - \left[1 - \exp\left(-\frac{\pi}{2}\frac{\Omega^2}{\alpha v}\right)\right]^{2F} \tag{5.10}$$

where $\alpha = g_F \mu_B b'/\hbar$, b' is the gradient of the magnetic field, and v is the atomic velocity. Increasing the Rabi frequency decreases the loss probability exponentially.

In this geometry, single-photon cooling is effectively a three-dimensional cooling technique. Thus the transfer efficiency (Equation 4.8) could, in principle, be unity. The only unavoidable loss mechanism is the branching ratio.

5.3 The Hydrogen Experiment

Although atomic hydrogen possesses a cycling transition and could, in principle, be laser cooled, lasers at the required wavelength (121 nm) do not exist with sufficient power to achieve appreciable cooling [109]. With great effort, hydrogen has been trapped and cooled [110] and even Bose-condensed [111] using a dilution refrigerator and evaporative cooling. The complexity of these experiments, however, was immense, and the lack of full optical access to the atoms greatly limited the scope of the investigations that could be performed.

In conjunction with the recently developed methods for decelerating supersonic pulses, single-photon cooling is a prime candidate for producing ultra-cold samples of atomic hydrogen and its isotopes in a simple apparatus with ample optical access [25]. Such a capability would be paramount for enabling a number of extraordinary investigations, including precision measurement of the $1S-2S$ transition frequency for all hydrogenic isotopes [112], tests of CPT by comparison with anti-hydrogen [113, 114], and even measurement of the neutrino mass [115]. With these goals in mind, this section describes progress toward building such an apparatus.

5.3.1 Slowing and Trapping

It has historically been a great challenge to produce trapped samples of gases which do not possess accessible cycling transitions. A general approach that has been picking up momentum in the scientific community is the

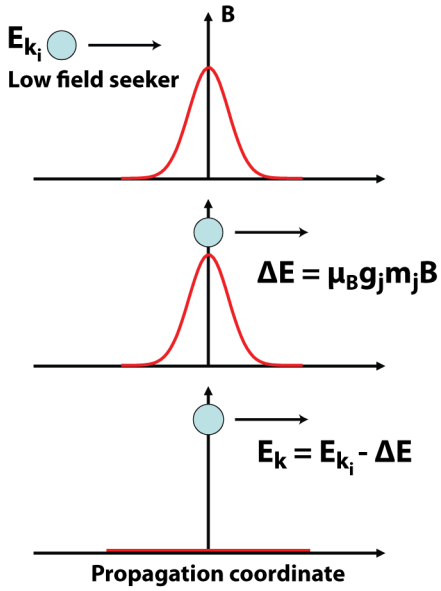

Figure 5.6: Fundamental principle of the atomic coilgun. Atoms lose kinetic energy as they climb the magnetic potential. The field is switched off when the atoms are near the peak, leading to a net reduction in kinetic energy.

deceleration of supersonic pulses. These pulses are created by nozzles which separate chambers of high pressure and vacuum. As the gas transits the nozzle, it adiabatically expands and cools to a temperature around 100 mK in the co-moving frame. However, the enthalpy is converted into kinetic energy, resulting in a pulse velocity typically greater than 500 m/s in the lab frame.

The collective kinetic energy of these pulses can be removed using a series of electromagnetic coils, the operation of which is analogous to a coilgun acting in reverse. Figure 5.6 shows the operating principle at the heart of the so-called 'atomic coilgun.' An atom (or molecule) in a low-field seeking state propagates with kinetic energy E_{k_i} along the axis of an electromagnetic coil.

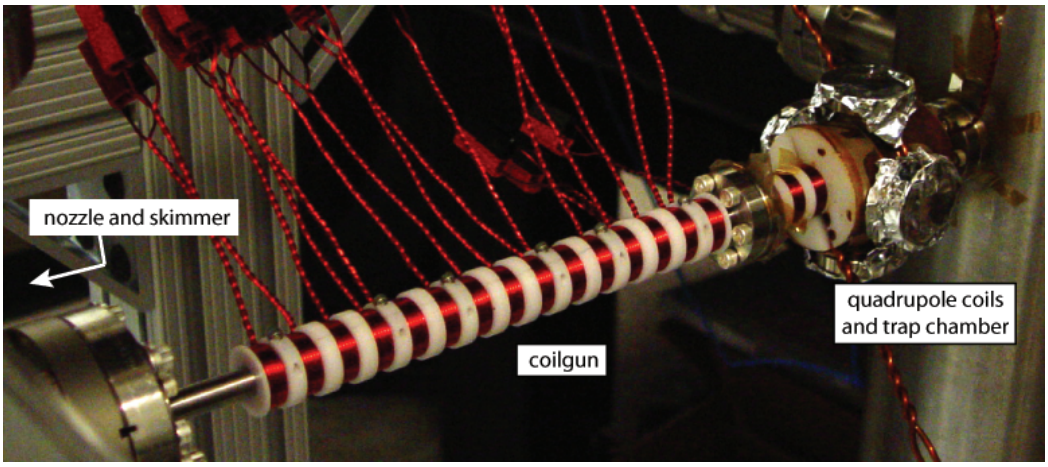

Figure 5.7: The hydrogen chamber.

Current through this coil generates an axial field as drawn. Once the atom has climbed the magnetic potential, the field is quickly extinguished, leaving the atom with a final kinetic energy $E_k < E_{k_i}$. This process is repeated as the pulse propagates through a series of coils until all the collective kinetic energy has been removed, at which point the pulse may be trapped in a static magnetic field.

A photograph of the vacuum chamber under construction for the hydrogen experiment is shown in Figure 5.7. Molecular hydrogen is seeded in a helium carrier gas on the high pressure side of a supersonic valve. As the gas transits the nozzle, a DC discharge dissociates the hydrogen molecules. The atoms that are produced pass through a skimmer and enter the coilgun.

The coilgun comprises 18 electromagnetic coils with inner diameter 1 cm. Around 825 A of current flows through 24 windings (4 layers $\times$ 6 windings)

of 17 gauge copper, producing a peak field of 1.9 T. The coils each are spaced by 1.2 cm, giving the coilgun a total length of about 30 cm. At the end of the coilgun are two large coils which create a quadrupole trap for the pulse once it has been stopped. With a static current of 500 A, the trap depth is approximately 100 mK and has an axial radius of roughly 4 mm. As discussed in Section 5.1.2, a quadrupole trap is unsuitable for RF-dressed single-photon cooling. In the future, this trap will be converted to a Ioffe-Pritchard trap. The immediate experimental goal, however, is just to trap and detect hydrogen, and so a quadrupole trap will suffice.

It is interesting to note the similarities and differences between the coilgun and single-photon cooling. Both techniques reduce the ensemble's kinetic energy by converting it into magnetic potential energy and then discarding it. However, the coilgun doesn't lower the entropy of the ensemble, and thus no dissipative step is required, as is the case with single-photon cooling. This can be understood through the informational interpretation of entropy. The dense pulse released from the supersonic valve is just one particular microstate of a system which, assuming ergodicity, is most likely to be found in a diffuse microstate occupying the entire vacuum chamber with entropy S_{diffuse}. The final state of the system after deceleration is a cold, trapped ensemble with entropy $S_{\text{trapped}} < S_{\text{diffuse}}$. This inequality is justified because the final state occupies a smaller volume in both configuration and velocity space. Naively, it may seem that entropy has been reduced, but it must be noted that information on the pulse's position and velocity is required to operate the coilgun.

This information is known *a priori*, and so the initial entropy of the pulse $S_{\text{initial}} = S_{\text{diffuse}} = S_{\text{trapped}} + S_{\text{info}}$, where S_{info} is the information entropy associated with the *a priori* knowledge. Thus the expression $S_{\text{trapped}} < S_{\text{initial}}$ does not imply a reduction of physical entropy.

5.3.2 Two-Photon Excitation

The $1S-2S$ transition of atomic hydrogen will be used for both detection and cooling. Because there is no change in orbital angular momentum, parity conservation prohibits this transition for a single photon. Nonetheless, the transition can be driven with two photons at 243 nm, the first of which excites a virtual P state which includes contributions from all nP states plus the continuum, and the second of which transfers the atom to the $2S$ state. This process has been analyzed in detail [116, 117]; the main results are given here.

Consider two counter-propagating laser beams with wavevectors $\mathbf{k}_1 = \mathbf{k}_2$. Doppler-sensitive excitation may occur by the absorption of two photons from one beam. For resonant excitation, the laser frequency must satisfy

$$2\hbar\omega_{\text{laser}} = E_{2S,\mathbf{p}_f} - E_{1S,\mathbf{p}_i} = \hbar\omega_{1S-2S} - \frac{2\hbar\mathbf{k}\cdot\mathbf{p}_i}{m} + \frac{2\hbar^2k^2}{m}, \tag{5.11}$$

where $\mathbf{p}_i$ ($\mathbf{p}_f$) is the initial (final) atomic momentum. The $\mathbf{k}\cdot\mathbf{p}_i$ term is referred to as the Doppler shift, and the term quadratic in k is the recoil shift. The Doppler shift leads to a broad excitation spectrum and thus a relatively small excitation rate.

Conversely, an atom may absorb one photon from both laser beams. In this case, $\mathbf{k}_1 \cdot \mathbf{p}_i = -\mathbf{k}_2 \cdot \mathbf{p}_i$ and so the Doppler shifts cancel each other. Additionally, there is no net recoil because the absorbed photons were counter-propagating. This is referred to as Doppler-insensitive excitation, and the laser frequency required for resonant excitation satisfies

$$2\hbar\omega_{\text{laser}} = E_{2S,\mathbf{p}_f} - E_{1S,\mathbf{p}_i} = \hbar\omega_{1S-2S}. \tag{5.12}$$

For linearly polarized laser beams with equal intensities $I_1 = I_1 = I$ and frequencies $\omega_{\text{laser}} = \omega_{1S-2S}/2$, the Rabi frequency for Doppler-insensitive excitation is given by

$$\Omega_0(\mathbf{r}) = 2M^{12}_{2S,1S}\left(\frac{\alpha}{2R_\infty}\right)^3 \frac{1}{3\pi^2\hbar c}\sqrt{I_1(\mathbf{r})I_2(\mathbf{r})} = 9.264\, I(\mathbf{r})\,\text{s}^{-1}\,\text{cm}^2\,\text{W}^{-1}, \tag{5.13}$$

where $M^{12}_{2S,1S} = 11.78$ is the sum over two-photon dipole matrix elements [118], α is the fine structure constant, and R_∞ is the Rydberg constant. For weak resonant excitation, the transition rate is

$$R = \frac{\Omega_0(\mathbf{r})^2}{\Gamma} = \frac{85.8}{\Gamma} I(\mathbf{r})^2\,\text{s}^{-1}\,\text{cm}^2\,\text{W}^{-1}, \tag{5.14}$$

where Γ is the homogeneous linewidth. With no external sources of broadening present, the linewidth is determined by the lifetime of the $2S$ state: $\Gamma = \Gamma_{2S} = 8.2\,\text{s}^{-1}$. Setting $R = \Gamma$ then gives an effective resonant saturation intensity of $0.89\,\text{W/cm}^2$ [61].

The first thing to notice in Equation 5.14 is that the rate scales with the square of the intensity, as opposed to the single-photon excitation rate

(Equation 2.2) which scales linearly with intensity. The two-photon rate is thus much more sensitive to intensity, and much higher powers are typically required to drive two-photon transitions efficiently.

Furthermore, the transition rate is inversely proportional to the effective linewidth. In the present experiment, this linewidth is not given by the natural linewidth of hydrogen, but by two other sources: the excitation laser linewidth and transit time broadening. The former is a function of laser design and stability, and it is discussed in Section 5.3.3. The latter is simply a manifestation of the energy-time uncertainty relation $\Delta E \Delta t \approx \hbar$. As an atom's trajectory passes though the laser beams, the atom sees a time-dependent intensity and hence a time-dependent excitation rate. The resulting spectral width is related to the inverse of the time the atom spends in the laser beams. Assuming that the excitation amplitudes from multiple passes through the beams add incoherently, there are no Ramsey fringes and the $1/e$ half-width due to transit time broadening is given by

$$\Gamma_{\mathrm{tt}} = \frac{1}{w_0}\sqrt{\frac{2k_B T}{m}}, \tag{5.15}$$

where w_0 is the laser beam waist corresponding to the Gaussian intensity profile

$$I(x,y) = \frac{2P}{\pi w_0^2}\exp\left[-\frac{2(x^2+y^2)}{w_0^2}\right], \tag{5.16}$$

where P is the total power in the beam.

Ideally, for both detection and RF-dressed single-photon cooling, one would like to illuminate the entire volume of the magnetic trap with counter-

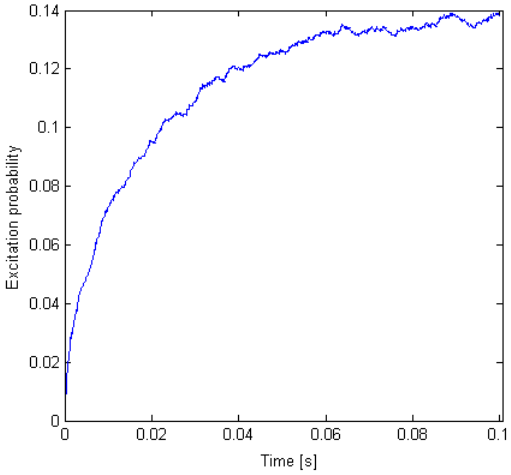

Figure 5.8: Monte Carlo simulation of two-photon excitation in the magnetic trap. The fraction of excited atoms in the magnetic trap is plotted as a function of interrogation time. For 300 mW of counter-propagating power focused to a waist of 50 μm with a laser linewidth of 40 kHz, about 14% of the atoms in the magnetic trap are excited after 100 ms interrogation time. Plot courtesy of Robert Clark.

propagating beams. For a given intensity, this would minimize transit time broadening and maximize the transition rate. However, due to the limited power currently achievable in a 243 nm laser, one must balance a decrease in transit time broadening with a concomitant decrease in intensity. From Equations 5.15 and 5.16, it can be seen that the transition rate $R \sim w_0^{-3}$.

Experimentally, one strategy is to match the transit time broadening with the laser linewidth by setting the beam waist. The transition rate can then be increased with the use of a Fabry-Perot cavity [119, 120], which creates a counter-propagating standing wave with high intensity. Robert Clark has performed Monte Carlo simulations which integrate the optical Bloch equa-

tions [57] for atomic trajectories in the quadrupole trap. A plot of the excitation fraction as a function of interrogation time is shown in Figure 5.8.

After excitation, hydrogen atoms can be detected either by launching them into a micro-channel plate (MCP), or by quenching them and detecting the emitted Lyman-α photons with a photo-multiplier tube (PMT).

5.3.3 Laser System

Ultraviolet (UV) radiation at 243 nm is generated by an amplified and frequency-quadrupled semiconductor laser. This section describes each component used to produce a stable and tunable source for driving the hydrogen $1S - 2S$ transition. A schematic of the beam distribution and components is shown in Figure 5.9.

Master Laser

The master laser is an infrared ECDL which lases at 972 nm. The diode (Eagleyard Photonics RWE-0980-08020-1500-SOT02) is a single-mode ridge waveguide GaAs laser which is AR coated to extend its bandwidth. The nominal lasing wavelength is 980 nm, but the gain profile extends from 900-1000 nm. The diode is mounted in a temperature-controlled bronze block, which in turn is mounted on an Invar breadboard for additional thermal stability.

Because phase noise is multiplied during each wavelength conversion process and the hydrogen resonance is at the eighth harmonic of the funda-

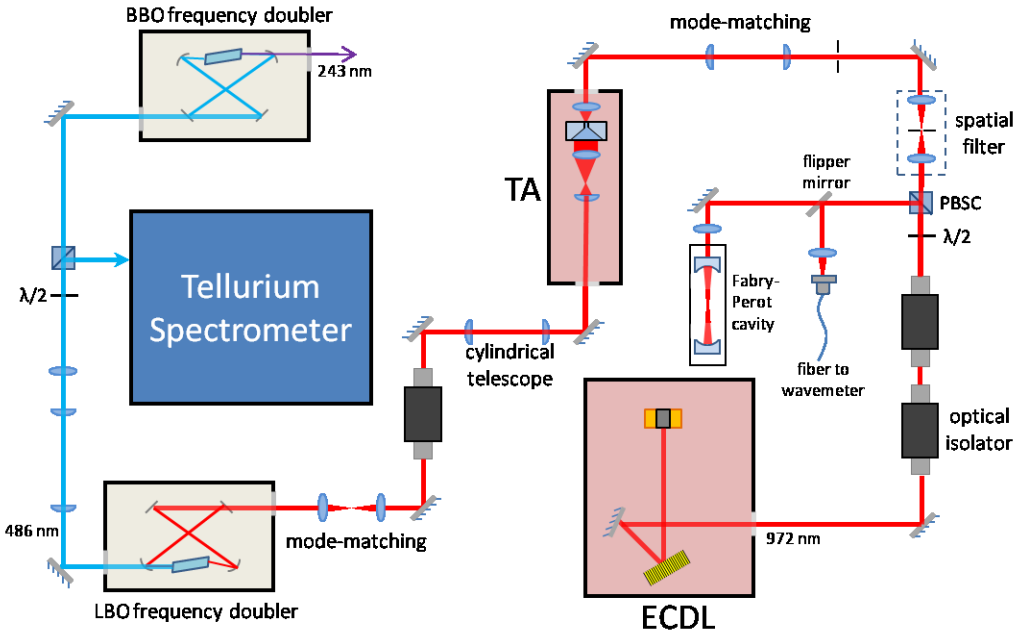

Figure 5.9: Beam distribution for the 243 nm laser.

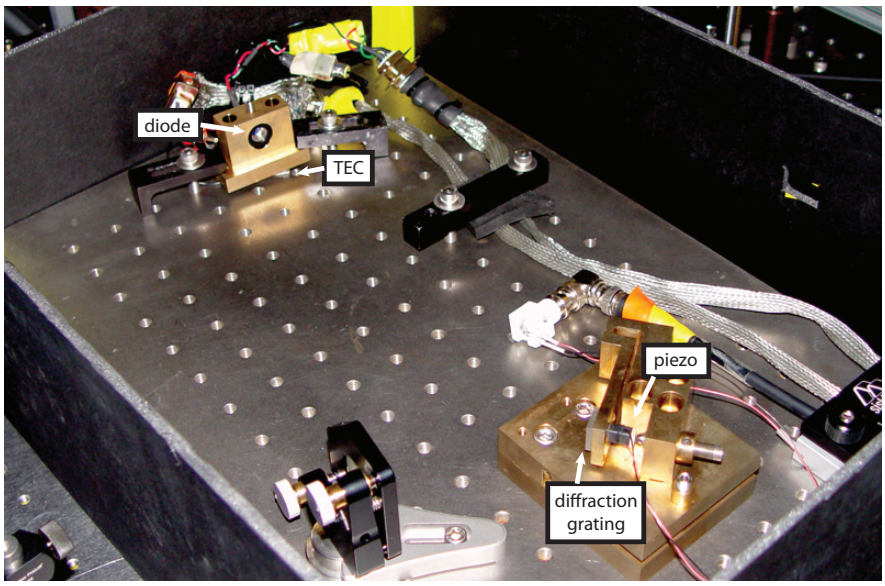

Figure 5.10: The 972 nm master laser.

mental infrared frequency, it is critical that phase noise be suppressed as much as possible. To address this issue, the diffraction grating is mounted on the Invar breadboard approximately 27 cm from the diode. A long cavity such as this one acts as a flywheel for the laser radiation, which averages out the high-frequency phase noise of the diode. The holographic diffraction grating has 1200 lines/mm and retroreflects about 30% of the incident power back to the diode.

A photograph of the master laser is shown in Figure 5.10. It typically produces around 70 mW output power at an injection current of 120 mA. The wavelength can be tuned with a piezo stack, which controls the angle of the diffraction grating. A 700 kHz upper bound for the linewidth has been measured using a reference Fabry-Perot cavity. Most likely, the linewidth is closer to 20 kHz, as this value was measured for a similarly constructed laser [121].

Master Oscillator Power Amplifier

Single-mode semiconductor diode lasers are limited in output power due to nonradiative surface recombination and thermal damage resulting from high optical power. One solution to this problem is the use of a semiconductor amplifier with a tapered gain region [122]. A tapered amplifier (TA) can produce high output power with good mode quality while retaining the spectral characteristics of the master laser which is injected into its rear facet. Such a configuration is referred to as a master oscillator power amplifier (MOPA)

system.

After exiting the ECDL, the laser beam passes through two optical isolators (Conoptics 713B, 714) which provide about 80 dB isolation while transmitting around 85% of the power. One isolator alone was insufficient in preventing light emitted from the rear facet of the TA from destabilizing the frequency of the master laser. After the isolators, about 5 mW is picked off with a PBSC and sent to a wavemeter and a Fabry-Perot cavity for frequency diagnostics. The remainder ($\sim 50\,\mathrm{mW}$) is spatially filtered with a telescope-pinhole combination and mode-matched to the TA with a cylindrical telescope.

The TA was originally a home-built system using a 2 W amplifier chip (m2k-laser GmbH TAL-0976-2000). Over a period of about six months, the output mode quality and stability of the chip worsened drastically, and so it was replaced by a commercial system (Toptica Photonics BoosTA-L-980). This TA produces 1 W output power in a clean mode and has been extremely stable since installation. The output of the tapered amplifier is highly astigmatic, so it is collimated with a combination of an aspheric lens and a cylindrical lens, and then it is circularized with a cylindrical telescope. After this, it passes through an optical isolator (Conoptics 713B) which prevents potentially damaging back-reflections from re-entering the TA. About 900 mW is transmitted through the isolator.

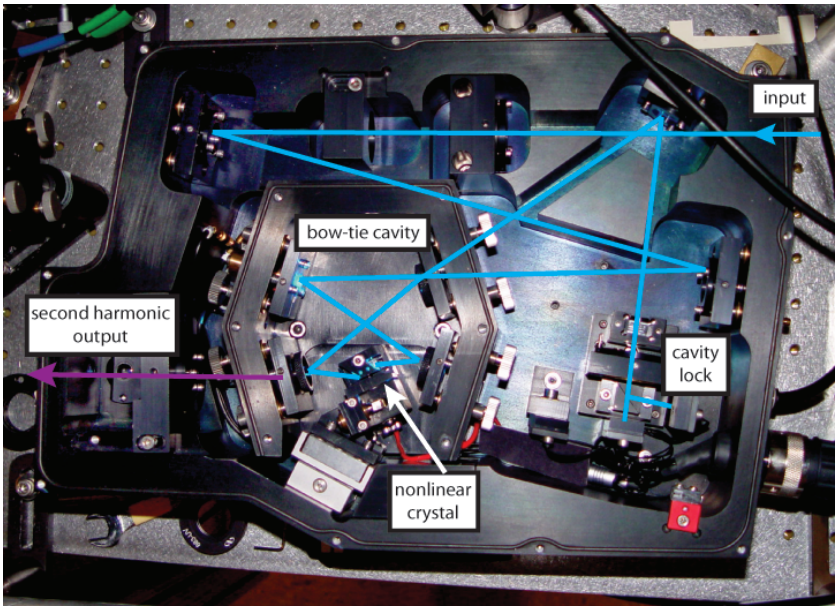

Figure 5.11: The second frequency doubler.

Frequency Doublers

Subsequent to the isolator, the beam is mode-matched for a commercial frequency doubler (Coherent MBD-200). The doubler comprises a bow-tie enhancement cavity with a lithium triborate (LBO) nonlinear crystal at the focus. The cavity is locked to the master laser frequency using a Hänsch-Couillaud lock [123]. About 110 mW of blue 486 nm light is produced in this doubler.

The blue light exits the first doubler through a dichroic mirror which is highly reflective at 972 nm. It is then mode-matched with three lenses to a second frequency doubler. This unit is nearly identical to the first, but uses an intracavity beta barium borate (BBO) crystal rather than LBO to create

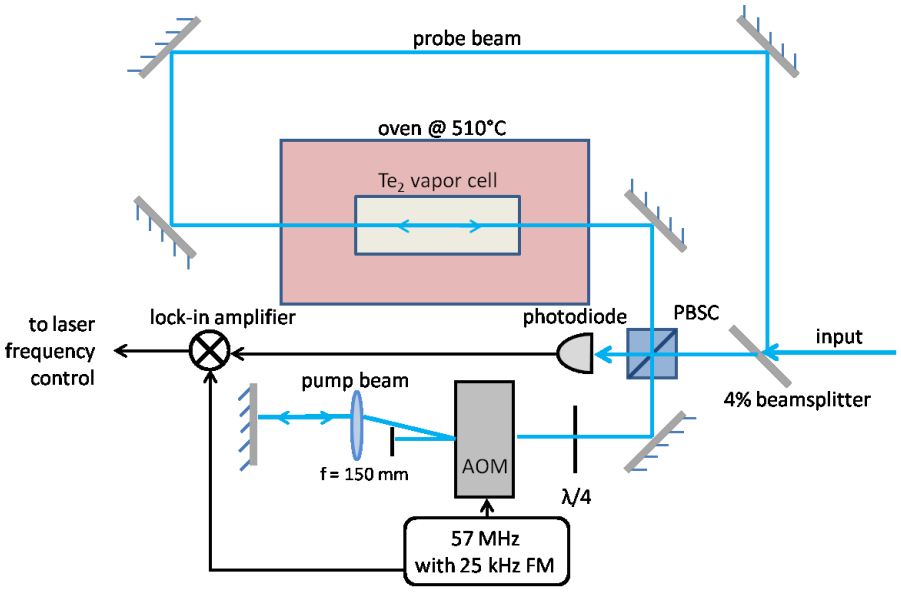

Figure 5.12: The molecular tellurium spectrometer. A glass plate beamsplitter picks off 4% of the beam for the probe. The remainder (the pump beam) is reflected by a PBSC and double-passes a 57 MHz AOM which is dithered at 25 kHz. The polarization is rotated twice by a quarter waveplate, so it passes straight through the PBSC on its second encounter, and it counter-propagates with the probe beam through the tellurium cell. The probe beam is reflected by the PBSC after passing through the cell, and it is picked up by a fast photodiode. The resulting signal is mixed with the dither frequency and sent to a PID controller which feeds back to the master laser piezo stack.

a few milliwatts of 243 nm light. A photograph of this doubler with labeled components is shown in Figure 5.11.

Tellurium Spectrometer

In between the two frequency doublers, about 10 mW of blue light is picked off by a PBSC and sent to a saturated absorption setup, as depicted in Figure 5.12. Molecular tellurium serves as a frequency reference, as its

excitation lines near 486 nm are known to better than 1 MHz [124–126]. For a Te_2 cell at a temperature around 510°C, the i_2 line (near line 1284 in [127]) has been found to be approximately 57 MHz above the 1/4 harmonic of the hydrogen $1S - 2S$ transition frequency. This displacement is compensated by the 57 MHz double-pass AOM in the path of the pump beam. The error signal from the spectrometer is fed back to the piezo stack of the master laser, closing the feedback loop and locking the laser on the harmonic of the hydrogen resonance.

5.3.4 Future Directions

The next step for the experiment is to actually slow, trap, and detect hydrogen. There are also several improvements to the laser system which can be made in order to increase the excitation fraction in the magnetic trap. First, more UV power will increase the excitation rate. In principle, the frequency doublers can operate more efficiently, and an increase by a factor of 10 in UV power is not unforeseeable. The UV intensity can also be increased by using higher reflectivity mirrors in Fabry-Perot cavity. Additionally, narrowing the linewidth of the laser could help to increase the excitation rate. A common practice is to stabilize the laser frequency with the aid of an ultra-stable reference cavity [128].

After this, the experiment will be upgraded for single-photon cooling. The quadrupole trap must be replaced with a Ioffe-Pritchard trap, and antennas will be installed to provide the necessary RF and microwave fields.

Appendix

Contributions

The work presented in this dissertation was almost entirely the result of collaborative efforts by myself, fellow graduate students, postdoctoral scholars, and my advisor. Unless otherwise cited, I have discussed only work in which I played a central role in producing. It is a difficult, if not impossible, task to completely isolate the contributions of individual researchers to the final results of the cooling experiments. Nonetheless, I will attempt in this appendix to provide a rough sketch of each group member's involvement.

Rubidium

The original idea for the rubidium experiment was conceived by my advisor, Mark Raizen, and the particular implementation for the first generation of the experiment was developed jointly by Mark and Gabriel Price. Though the first demonstration was not discussed in this dissertation, I worked on it closely alongside Gabriel, and Kirsten Viering joined the team after a semester. Our postdoc Ed Narevicius was available for many discussions and made helpful suggestions along the way.

We had the good fortune of starting with an experimental infrastructure left over from a previous rubidium BEC experiment. Gabriel, Kirsten, and I worked together to adapt the apparatus (vacuum chamber, magnetic system,

MOT lasers, and computer control system) for single-photon cooling. We rerouted lasers, installed optical components, designed and built a new optical trap, and set up new imaging systems. I wrote the bulk of the new computer code that was necessary to run the cooling sequence in *Control* and interface a new CCD camera with *Vision*. I also wrote code for a Monte Carlo simulation which was later taken up and improved by Kirsten.

There was a great amount of maintenance which the three of us contributed to on a daily basis to keep the apparatus working. A short list of the main tasks included debugging general malfunctions, tweaking PID circuits, repairing electronics, realigning lasers, and replacing failed laser diodes.

The cooling experiment with rubidium discussed in this dissertation followed our first demonstration. I played a central role in the development and implementation of the major modifications to the previous technique. These included designing a new optical trap and repositioning it beneath the magnetic trap, adiabatically expanding the ensemble during the cooling sequence rather than translating it, and detuning the demon beam from resonance. Though the acquisition and analysis of data overall was a collaborative effort, I led the development and interpretation of the analytical model that clarified our results and defined the limits of the cooling technique.

For a few months, I worked, with the assistance of Gabriel, on implementing RF-dressed single-photon cooling with rubidium. We did not observe phase-space compression, likely due to constraints imposed by the apparatus, and so the results were not published. However, we did observe irreversible

transfer between dressed state potentials.

Hydrogen

Progress toward building the hydrogen experiment has been achieved on two fronts: trapping and cooling. The former has involved construction of the vacuum chamber, coilgun, and magnetic trap. Adam Libson, Tom Mazur, Isaac Chavez, and Rob Clark have all worked on this aspect of the experiment.

My efforts have been focused on cooling. Along with Mark and Ed, I devised the technique for cooling in three dimensions using RF-dressed states. With the assistance of Rob, I led the design, construction, and characterization of the 243 nm laser system for excitation of hydrogen, including the ECDL, first generation TA, and tellurium spectrometer. We have also installed and characterized the commercial TA and frequency doubling units.

Bibliography

[1] J.C. Maxwell. Diffusion. In Thomas Spencer Baynes, editor, *The Encyclopædia Brittanica*, volume VII. Henry G. Allen and Co., New York, 9th edition, 1878.

[2] R. Clausius. *The Mechanical Theory of Heat*. John Van Voorst, London, 1865.

[3] A.S. Eddington. *The Nature of the Physical World*. The Macmillan Company, 1928.

[4] E. Fermi. *Thermodynamics*. Dover, New York, 1956.

[5] K. Huang. *Statistical Mechanics*. John Wiley & Sons, 2nd edition, 1987.

[6] H. Poincaré. The principles of mathematical physics. In *Physics for a New Century: Papers Presented at that 1904 St. Louis Congress*, page 281. Tomash, Los Angeles, 1986.

[7] G. D'Abramo. The peculiar status of the second law of thermodynamics and the quest for its violation. *arXiv:1101.5056v2 [physics.class-ph]*, 2011.

[8] C.G. Knott. *Life and Scientific Work of Peter Gutherie Tait.* Cambridge University Press, Cambridge, 1911.

[9] W. Thomson. The kinetic theory of the dissipation of energy. *Nature*, 9:441, 1874.

[10] L. Szilard. On the decrease of entropy in a thermodynamic system by the intervention of intelligent beings. In H.S. Leff and A.F. Rex, editors, *Maxwell's Demon 2: Entropy, Classical and Quantum Information, Computing.* Institute of Physics, Philadelphia, 2003.

[11] L. Brillouin. Maxwell's demon cannot operate: information and entropy I. *Journal of Applied Physics*, 22:332, 1951.

[12] L. Brillouin. Maxwell's demon cannot operate: information and entropy II. *Journal of Applied Physics*, 22:338, 1951.

[13] D. Gabor. *Progress in Optics*, volume 13, page 111. North-Holland, Amsterdam, 1961.

[14] C.H. Bennett. The thermodynamics of computation–a review. *International Journal of Theoretical Physics*, 21:905, 1982.

[15] R. Landauer. Irreversibility and heat generation in the computing process. *IBM Journal of Research and Development*, 5:183, 1961.

[16] C. Shannon. The mathematical theory of communication. *Bell Systems Technical Journal*, 27:379, 1948.

[17] E.T. Jaynes. Information theory and statistical mechanics. II. *Physical Review*, 106:620, 1957.

[18] G.N. Lewis. The symmetry of time in physics. *Science*, 71:569, 1930.

[19] J. Earman and J.D. Norton. Exorcist XIV: The wrath of Maxwell's demon. Part I. From Maxwell to Szilard. *Studies in History and Philosophy of Modern Physics*, 29:435, 1998.

[20] J. Earman and J.D. Norton. Exorcist XIV: The wrath of Maxwell's demon. Part II. From Szilard to Landauer and beyond. *Studies in History and Philosophy of Modern Physics*, 30:1, 1999.

[21] J.D. Norton. Eaters of the lotus: Landauer's principle and the return of Maxwell's demon. *Studies in History and Philosophy of Modern Physics*, 36:375, 2005.

[22] D. Möhl, G. Petrucci, L. Thorndahl, and S. van der Meer. Physics and technique of stochastic cooling. *Physics Reports*, 58:74, 1980.

[23] S. van der Meer. Stochastic cooling and the accumulation of antiprotons. *Review of Modern Physics*, 57:689, 1985.

[24] S. Toyabe, T. Sagawa, M. Ueda, E. Muneyuki, and M. Sano. Experimental demonstration of information-to-energy conversion and validation of the generalized Jarzynski equality. *Nature Physics*, 6:988, 2010.

[25] M.G. Raizen. Comprehensive control of atomic motion. *Science*, 324:1403, 2009.

[26] M.G. Raizen, A.M. Dudarev, Q. Niu, and N.J. Fisch. Compression of atomic phase space using an asymmetric one-way barrier. *Physical Review Letters*, 94:053003, 2005.

[27] A. Ruschhaupt and J.G. Muga. Atom diode: a laser device for unidirectional transmission of ground-state atoms. *Physical Review A*, 70:061604(R), 2004.

[28] A.M. Dudarev, M. Marder, Q. Niu, N.J. Fisch, and M.G. Raizen. Statistical mechanics of an optical phase space compressor. *Europhysics Letters*, 70:761, 2005.

[29] A. Ruschhaupt, J.G. Muga, and M.G. Raizen. Improvement by laser quenching of an 'atom diode': a one-way barrier for ultra-cold atoms. *Journal of Physics B: Atomic, Molecular and Optical Physics*, 39:L133, 2006.

[30] A. Ruschhaupt, J.G. Muga, and M.G. Raizen. One-photon atomic cooling with an optical Maxwell demon valve. *Journal of Physics B: Atomic, Molecular and Optical Physics*, 39:3833, 2006.

[31] G.N. Price, S.T. Bannerman, E. Narevicius, and M.G. Raizen. Single-photon atomic cooling. *Laser Physics*, 17:1, 2007.

[32] G.N. Price, S.T. Bannerman, K. Viering, E. Narevicius, and M.G. Raizen. Single-photon atomic cooling. *Physical Review Letters*, 100:093004, 2008.

[33] J.J. Thorn, E.A. Schoene, T. Li, and D.A. Steck. Experimental realization of an optical one-way barrier for neutral atoms. *Physical Review Letters*, 100:240407, 2008.

[34] S.T. Bannerman, G.N. Price, K. Viering, and M.G. Raizen. Single-photon cooling at the limit of trap dynamics: Maxwell's demon near maximum efficiency. *New Journal of Physics*, 11:063044, 2009.

[35] E. Narevicius, S.T. Bannerman, and M.G. Raizen. Single-photon molecular cooling. *New Journal of Physics*, 11:055046, 2009.

[36] K.G. Denbigh and J.S. Denbigh. *Entropy in Relation to Incomplete Knowledge*. Cambridge University Press, Cambridge, 1985.

[37] K. Maruyama, F. Nori, and V. Vedral. Colloquium: The physics of Maxwell's demon and information. *Reviews of Modern Physics*, 81:1, 2009.

[38] A.G. van Melsen. *From Atomos to Atom: The History of the Concept Atom*. Dover, New York, 2004.

[39] A.L. Schowlow and C.H. Townes. Infrared and optical masers. *Physical Review*, 112:1940, 1958.

[40] T.H. Maiman. Stimulated optical radiation in ruby. *Nature*, 187:493, 1960.

[41] V.G. Minogin and V.S. Letokhov. *Laser Light Pressure on Atoms*. Gordon and Breach, New York, 1987.

[42] T.W. Hansch and A.L. Schawlow. Cooling of gases by laser radiation. *Optics Communications*, 13:68, 1975.

[43] D. Wineland and H. Dehmelt. Proposed $10^{14}\ \Delta\nu < \nu$ laser fluorescence spectroscopy on $T1^{+}$ mono-ion oscillator III. *Bulletin of the American Physical Society*, 20:637, 1975.

[44] D. Wineland, R. Drullinger, and F. Walls. Radiation-pressure cooling of bound resonant absorbers. *Physical Review Letters*, 40:1639, 1978.

[45] W. Neuhauser, M. Hohenstatt, P. Toschek, and H. Dehmelt. Optical-sideband cooling of visible atom cloud confined in a parabolic well. *Physical Review Letters*, 41:233, 1978.

[46] J. Prodan, A. Migdall, W.D. Phillips, I. So, H. Metcalf, and J. Dalibard. Stopping atoms with laser light. *Physical Review Letters*, 54:992, 1985.

[47] W. Ertmer, R. Blatt, J.L. Hall, and M. Zhu. Laser manipulation of atomic beam velocities: Demonstrations of stopped atoms and velocity reversal. *Physical Review Letters*, 54:996, 1985.

[48] K.B. Davis, M.O. Mewes, M.R. Andrews, N.J. van Druten, D.S. Durfee, D.M. Kurn, and W. Ketterle. Bose-Einstein condensation in a gas of sodium atoms. *Physical Review Letters*, 75:3969, 1995.

[49] M.H. Anderson, J.R. Ensher, M.R. Matthews, C.E. Weiman, and E.A. Cornell. Observation of Bose-Einstein condensation in a dilute atomic vapor. *Science*, 269:198, 1995.

[50] B. DeMarco and D.S. Jin. Onset of Fermi degeneracy in a trapped atomic gas. *Science*, 285:1703, 1999.

[51] T.L. Gustavson, P. Bouyer, and M.A. Kasevich. Precision rotation measurements with an atom interferometer gyroscope. *Physical Review Letters*, 78:2046, 1997.

[52] A.D. Ludlow, T. Zelevinsky, G.K. Campbell, S. Blatt, M.M. Boyd, M.H.G. de Miranda, M.J. Martin, J.W. Thomsen, S.M. Foreman, J. Ye, T.M. Fortier, J.E. Stalnaker, S.A. Diddams, Y. Le Coq, Z.W. Barber, N. Poli, N.D. Lemke, K.M. Beck, and C.W. Oates. Sr lattice clock at 1×10^{-16} fractional uncertainty by remote optical evaluation with a ca clock. *Science*, 319:1805, 2008.

[53] Quantum Computation and Quantum Information. *M.A. Nielsen and I.L. Chuang*. Cambridge University Press, Cambridge, 2000.

[54] J.V. José and E.J. Saletan. *Classical Dynamics: A Contemporary Approach*. Cambridge University Press, Cambridge, 1998.

[55] W. Ketterle and D.E. Pritchard. Atom cooling by time-dependent potentials. *Physical Review A*, 46(7):4051, 1992.

[56] P.W.H. Pinske, A. Mosk, M. Weidemüller, M.W. Reynolds, T.W. Hijmans, and J.T.M. Walraven. Adiabatically changing the phase-space density of a trapped Bose gas. *Physical Review Letters*, 78:990, 1997.

[57] H.J. Metcalf and P. van der Straten. *Laser Cooling and Trapping*. Springer, New York, corrected edition, 1999.

[58] P. Meystre. *Atom Optics*. Springer, 2001.

[59] L. Allen and J.H. Eberly. *Optical Resonance and Two-Level Atoms*. Dover, 1987.

[60] D.A. Steck. Rubidium 87 D line data. http://steck.us/alkalidata, September 2008.

[61] J.C. Sandberg. *Research Toward Laser Spectroscopy of Trapped Atomic Hydrogen*. PhD thesis, Massachusetts Institute of Technology, 1993.

[62] C.J. Foot. *Atomic Physics*. Oxford University Press, New York, 2005.

[63] E.L. Raab, M. Prentiss, A. Cable, S. Chu, and D.E. Pritchard. Traping of neutral sodium atoms with radiation pressure. *Physical Review Letters*, 54:2596, 1985.

[64] I. Sobelman. *Atomic Spectra and Radiative Transitions*. Springer-Verlag, Berlin, 1992.

[65] D.A. Varshalovich, A.N. Moskalev, and V.K. Khersonskii. *Quantum Theory of Angular Momentum*. World Scientific, Singapore, 1988.

[66] G.A. Askar'yan. Effects of the gradient of a strong electromagnetic beam on electrons and atoms. *Soviet Physics JETP*, 15:1088, 1962.

[67] S. Chu, J.E. Bjorkholm, A. Ashkin, and A. Cable. Experimental observation of optically trapped atoms. *Physical Review Letters*, 57:314, 1986.

[68] R. Grimm, M. Weidemüller, and Y. Ovchinnikov. Optical dipole traps for neutral atoms. *Advances in Atomic, Molecular, and Optical Physics*, 42:95, 2000.

[69] J.D. Jackson. *Classical Electrodynamics*. Wiley, New York, 3rd edition, 1999.

[70] C. Cohen-Tannoudji, B. Diu, and F. Laloë. *Quantum Mechanics*. Hermann, Paris, 1977.

[71] A.L. Migdall, J.V. Prodan, and W.D. Phillips. First observation of magnetically trapped neutral atoms. *Physical Review Letters*, 54:2596, 1985.

[72] W. Wing. On neutral particle trapping in quasistatic electromagnetic fields. *Progress in Quantum Electronics*, 8:181, 1984.

[73] J.L. Hanssen. *Controlling Atomic Motion: From Single Particle Classical Mechanics to Many Body Quantum Dynamics*. PhD thesis, The University of Texas at Austin, 2004.

[74] T.P. Meyrath. *Experiments with Bose-Einstein Condensation in an Optical Box*. PhD thesis, The University of Texas at Austin, 2005.

[75] C.-S. Chuu. *Direct Study of Quantum Statistics in a Degenerate Bose Gas*. PhD thesis, The University of Texas at Austin, 2006.

[76] G.N. Price. *Single-Photon Atomic Cooling*. PhD thesis, The University of Texas at Austin, 2008.

[77] W. Wohlleben, F. Chevy, K. Madison, and J. Dalibard. An atom faucet. *European Physical Journal D*, 15:237, 2001.

[78] C.B. Alcock, V.P. Itkin, and M.K. Horrigan. Vapor pressure equations of the metallic elements: 298-2500 K. *Canadian Metallurgical Quarterly*, 23:309, 1984.

[79] T. Bergeman, G. Erez, and H. Metcalf. Magnetostatic trapping fields for neutral atoms. *Physical Review A*, 35:1535, 1987.

[80] C.E. Weiman and L. Hollberg. Using diode lasers for atomic physics. *Review of Scientific Instruments*, 62:1, 1991.

[81] D.A. Steck. *Quantum Chaos, Transport, and Decoherence in Atom Optics*. PhD thesis, The University of Texas at Austin, 2001.

[82] W. Demtröder. *Laser Spectroscopy.* Springer, New York, 2nd edition, 1996.

[83] A.E. Siegman. *Lasers.* University Science Books, Sausalito, 1986.

[84] D.S. Weiss, E. Riis, Y. Shevy, P.J. Ungar, and S. Chu. Optical molasses and multilevel atoms: experiment. *Journal of the Optical Society of America B*, 6:2072, 1989.

[85] W. Ketterle, D.S. Durfee, and D.M. Stamper-Kurn. Making, probing and understanding Bose-Einstein condensates. *arXiv:cond-mat/9904034v2*, 1999.

[86] C.-S. Chuu, F. Schreck, T.P. Meyrath, J.L. Hanssen, G.N. Price, and M.G. Raizen. Direct observation of sub-Poissonian number statistics in a degenerate bose gas. *Physical Review Letters*, 95:260403, 2005.

[87] W. Alt. An objective lens for efficient fluorescence detection of single atoms. *Optik*, 113:142, 2002.

[88] F. Schreck and T.P. Meyrath. A laboratory control system for cold atom experiments: Hardware and software. http://george.ph.utexas.edu/ control, March 2004.

[89] J. Dalibard and C. Cohen-Tannoudji. Laser cooling below the doppler limit by polarization gradients - simple theoretical models. *Journal of the Optical Society of America B*, 6:2023, 1989.

[90] E. Narevicius, A. Libson, C.G. Parthey, I. Chavez, J. Narevicius, U. Even, and M.G. Raizen. Stopping supersonic beams with a series of pulsed electromagnetic coils: an atomic coilgun. *Physical Review Letters*, 100:093003, 2008.

[91] S.D. Hogan, A.W. Wiederkehr, H. Schmutz, and F. Merkt. Magnetic trapping of hydrogen after multistage Zeeman deceleration. *Physical Review Letters*, 101:143001, 2008.

[92] E. Narevicius, A. Libson, C.G. Parthey, I. Chavez, J. Narevicius, U. Even, and M.G. Raizen. Stopping supersonic oxygen wtih a series of pulsed electromagnetic coils: a molecular coilgun. *Physical Review A*, 77:051401, 2008.

[93] H.L. Bethlem, G. Berden, and G. Meijer. Decelerating neutral dipolar molecules. *Physical Review Letters*, 83:1558, 1999.

[94] S.Y.T. van de Meerakker, P.H.M Smeets, N. Vanhaecke, R.T. Jongma, and G. Meijer. Deceleration and electrostatic trapping of OH radicals. *Physical Review Letters*, 94:023004, 2005.

[95] B.C. Sawyer, B.L. Lev, E.R. Hudson, B.K. Stuhl, M. Lara, J.L Bohn, and J. Ye. Magnetoelectrostatic trapping of ground state OH molecules. *Physical Review Letters*, 98:253002, 2007.

[96] C. Cohen-Tannoudji, J. Dupont-Roc, and G. Grynberg. *Atom-photon interactions: basic processes and applications*. Wiley, New York, 1998.

[97] O. Zobay and B.M. Garraway. Two-dimensional atom trapping in field-induced adiabatic potentials. *Physical Review Letters*, 86:1195, 2001.

[98] Y. Colombe, E. Knyazchyan, O. Morizot, B. Mercier, V. Lorent, and H. Perrin. Ultracold atoms confined in rf-induced two-dimensional trapping potentials. *Europhysics Letters*, 67:593, 2004.

[99] S. Hofferberth, I. Lesanovsky, B. Fischer, J. Verdu, and J. Schmiedmayer. Radiofrequency-dressed-state potentials for neutral atoms. *Nature*, 2:710, 2006.

[100] O. Morizot, C.L. Garrido Alzar, P.-E. Pottie, V. Lorent, and H. Perrin. Trapping and cooling of rf-dressed atoms in a quadrupole magnetic field. *Journal of Physics B: Atomic, Molecular, and Optical Physics*, 40:4013, 2007.

[101] T. Fernholz, R. Gerritsma, P. Krüger, and R.J.C. Spreeuw. Dynamically controlled toroidal and ring-shaped magnetic traps. *Physical Review A*, 75:063406, 2007.

[102] T. Schumm, S. Hofferberth, L.M. Andersson, S. Wildermuth, S. Groth, I. Bar-Joseph, J. Schmiedmayer, and P. Krüger. Matter-wave interferometry in a double well on an atom chip. *Nature Physics*, 1:57, 2005.

[103] I. Lesanovsky, T. Schumm, S. Hofferberth, L.M. Andersson, P. Krüger, and J. Schmiedmayer. Adiabatic radio-frequency potentials for the co-

herent manipulation of matter waves. *Physical Review A*, 73:033619, 2006.

[104] I. Lesanovsky, S. Hofferberth, J. Schmiedmayer, and P. Schmelcher. Manipulation of ultracold atoms in dressed adiabatic radio-frequency potentials. *Physical Review A*, 74:133619, 2006.

[105] S. Hofferberth, B. Fischer, T. Schumm, J. Schmiedmayer, and I. Lesanovsky. Ultracold atoms in radio-frequency dressed potentials beyond the rotating-wave approximation. *Physical Review A*, 76:013401, 2007.

[106] D.E. Pritchard. Cooling neutral atoms in a magnetic trap for precision spectroscopy. *Physical Review Letters*, 51:1336, 1983.

[107] J.H. Tung, X.M. Ye, G.J. Salamo, and F.T. Chan. Two-photon decay of hydrogenic atoms. *Physical Review A*, 30:1175, 1984.

[108] N.V. Vitanov and K.-A. Suominen. Time-dependent control of ultracold atoms in magnetic traps. *Physical Review A*, 56:R4377, 1997.

[109] D. Kolbe, A. Beczkowiak, T. Diehl, A. Koglbauer, A. Müllers, M. Scheid, M. Stappel, R. Steinborn, and J. Walz. Continuous Lyman-alpha generation by four-wave mixing in mercury for laser cooling of antihydrogen. *Canadian Journal of Physics*, 89:25, 2011.

[110] H. Hess, G.P. Kochanski, J.M. Doyle, N. Masuhara, D. Kleppner, and T.J. Greytak. Magnetic trapping of spin-polarized atomic hydrogen. *Physical Review Letters*, 59:672, 1987.

[111] D.G. Fried, T.C. Killian, L. Willmann, D. Landhuis, S.C. Moss, D. Kleppner, and T.J. Greytak. Bose-Einstein condensation of atomic hydrogen. *Physical Review Letters*, 81:3811, 1998.

[112] C.G. Parthey, A. Matveev, J. Alnis, R. Pohl, T. Udem, U.D. Jenschura, N. Kolachevsky, and T.W. Hänsch. Precision measurement of the hydrogen-deuterium 1S-2S isotope shift. *Physical Review Letters*, 104:233001, 2010.

[113] M. Amoretti *et al.* Production and detection of cold antihydrogen atoms. *Nature*, 419:456, 2002.

[114] G. Gabrielse *et al.* Background-free observation of cold antihydrogen with field-ionization analysis of its states. *Physical Review Letters*, 89:213401, 2002.

[115] M. Jerkins, J.R. Klein, J.H. Majors, F. Robicheaux, and M.G. Raizen. Using cold atoms to measure neutrino mass. *New Journal of Physics*, 12:043022, 2010.

[116] R.G. Beausoleil and T.W. Hänsch. Ultrahigh-resolution two-photon optical Ramsey spectroscopy of an atomic fountain. *Physical Review A*, 33:1661, 1986.

[117] T.C. Killian. *1S-2S Spectroscopy of Trapped Hydrogen: The Cold Collision Frequency Shift and Studies of BEC.* PhD thesis, Massachusetts Institute of Technology, 1999.

[118] F. Bassani, J.J. Forney, and A. Quattropani. Choice of gauge in two-photon transitions: 1s-2s transition in atomic hydrogen. *Physical Review Letters*, 39:1070, 1977.

[119] E. Hecht. *Optics*. Addison-Wesley, Boston, 2002.

[120] P.W. Milonni and J.H. Eberly. *Lasers*. Wiley, New York, 1988.

[121] J. Alnis, A. Mateev, N. Kolachevsky, T. Wilken, and T.W. Hänsch. Stable diode lasers for hydrogen precision spectroscopy. *European Physical Journal Special Topics*, 163:89, 2008.

[122] J.N. Walpole. Semiconductor amplifiers and lasers with tapered gain regions. *Optical and Quantum Electronics*, 28:623, 1996.

[123] T.W. Hänsch and B. Couillaud. Laser frequency stabilization by polarization spectroscopy of a reflecting reference cavity. *Optics Communications*, 35:441, 1980.

[124] R.M. Barr, J.M. Girkin, A.I. Ferguson, G.P. Barwood, P. Gill, W.R.C. Rowley, and R.C. Thompson. Interferometric frequency measurements of $^{130}Te_2$ transitions at 486 nm. *Optics Communications*, 54:217, 1985.

[125] D.H. McIntyre, W.M. Fairbank, Jr., S.A. Lee, T.W. Hänsch, and E. Riis. Interferometric frequency measurement of $^{130}Te_2$ reference transitions at 486 nm. *Physical Review A*, 41:4632, 1990.

[126] J.D. Gillaspy and C.J. Sansonetti. Absolute wavelength determinations in molecular tellurium: new reference lines for precision laser spectroscopy. *Optical Society of America B*, 8:2414, 1991.

[127] J. Cariou and P. Luc. Atlas du spectre d'absorption de la molecule de tellure, 1980.

[128] A.D. Ludlow, X. Huang, M. Notcutt, T. Zanon-Willette, S.M. Foreman, M.M Boyd, S. Blatt, and J. Ye. Compact, thermal-noise-limited optical cavity for diode laser stabilization at 1×10^{-15}. *Optics Letters*, 32:641, 2007.